

AFRL-IF-RS-TR-2002-247
Final Technical Report
September 2002



MEMS FOR WIRELESS COMMUNICATIONS

University of Michigan

Sponsored by
Defense Advanced Research Projects Agency
DARPA Order No. E117

APPROVED FOR PUBLIC RELEASE; DISTRIBUTION UNLIMITED.

The views and conclusions contained in this document are those of the authors and should not be interpreted as necessarily representing the official policies, either expressed or implied, of the Defense Advanced Research Projects Agency or the U.S. Government.

AIR FORCE RESEARCH LABORATORY
INFORMATION DIRECTORATE
ROME RESEARCH SITE
ROME, NEW YORK

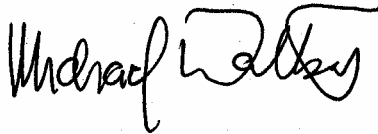
This report has been reviewed by the Air Force Research Laboratory, Information Directorate, Public Affairs Office (IFOIPA) and is releasable to the National Technical Information Service (NTIS). At NTIS it will be releasable to the general public, including foreign nations.

AFRL-IF-RS-TR-2002-247 has been reviewed and is approved for publication.

APPROVED:

A handwritten signature in black ink, appearing to read "David C. Williamson". The signature is fluid and cursive, with a large loop at the end.

DAVID C. WILLIAMSON
Project Engineer

A handwritten signature in black ink, appearing to read "Michael L. Talbert". The signature is fluid and cursive, with a large loop at the end.

FOR THE DIRECTOR:

MICHAEL L. TALBERT, Technical Advisor
Information Technology Division
Information Directorate

REPORT DOCUMENTATION PAGE			<i>Form Approved</i> OMB No. 074-0188	
Public reporting burden for this collection of information is estimated to average 1 hour per response, including the time for reviewing instructions, searching existing data sources, gathering and maintaining the data needed, and completing and reviewing this collection of information. Send comments regarding this burden estimate or any other aspect of this collection of information, including suggestions for reducing this burden to Washington Headquarters Services, Directorate for Information Operations and Reports, 1215 Jefferson Davis Highway, Suite 1204, Arlington, VA 22202-4302, and to the Office of Management and Budget, Paperwork Reduction Project (0704-0188), Washington, DC 20503				
1. AGENCY USE ONLY (Leave blank)		2. REPORT DATE Sep 02	3. REPORT TYPE AND DATES COVERED Final Apr 97 – Sep 01	
4. TITLE AND SUBTITLE MEMS FOR WIRELESS COMMUNICATIONS			5. FUNDING NUMBERS C - F30602-97-2-0101 PE - 63739E PR - E117 TA - 00 WU -17	
6. AUTHOR(S) Clark T.-C. Nguyen				
7. PERFORMING ORGANIZATION NAME(S) AND ADDRESS(ES) University of Michigan 2406 EECS Building 1301 Beal Ave. Ann Arbor, MI 48109-2122			8. PERFORMING ORGANIZATION REPORT NUMBER	
9. SPONSORING / MONITORING AGENCY NAME(S) AND ADDRESS(ES) Defense Advanced Research Projects Agency AFRL/IFTC 3701 North Fairfax Drive 26 Electronic Pky Arlington, VA 22203-1714 Rome, NY 13441-4514			10. SPONSORING / MONITORING AGENCY REPORT NUMBER AFRL-IF-RS-TR-2002-247	
11. SUPPLEMENTARY NOTES AFRL Project Engineer: David C. Williamson, IFTC, 315-330-7324, williamsond@rl.af.mil				
12a. DISTRIBUTION / AVAILABILITY STATEMENT Approved for public release; distribution unlimited.				12b. DISTRIBUTION CODE
13. ABSTRACT (Maximum 200 Words) The primary objectives of this project are 1) identification and study of the physical performance limitations incurred when extending the frequency range of miniaturized, micro-scale mechanical resonators to the VHF, UHF, and S-Band ranges; 2) implementation of prototype high-Q micromechanical filters and oscillators in these frequency ranges; and 3) subsequent incorporation of these components into the RF and IF stages of compact, inexpensive wireless transceivers. The proposed devices are not only orders of magnitude smaller than existing discrete resonator equivalents, but are also expected to outperform their macroscopic counterparts in insertion loss and percent bandwidth.				
14. SUBJECT TERMS Wireless Communications, Oscillators, MEMS, RF Filters, Resonators, System-on-a-Chip				15. NUMBER OF PAGES 81
				16. PRICE CODE
17. SECURITY CLASSIFICATION OF REPORT UNCLASSIFIED	18. SECURITY CLASSIFICATION OF THIS PAGE UNCLASSIFIED	19. SECURITY CLASSIFICATION OF ABSTRACT UNCLASSIFIED	20. LIMITATION OF ABSTRACT UL	

Table of Contents

1.0	PROJECT GOALS	1
1.1.	Miniaturization of Transceivers.....	1
1.2.	The Need for High Q in Oscillators.....	2
1.3.	The Need for High Q in Filters.....	4
2.0	APPROACH/PROBLEMS TO BE ADDRESSED	4
2.1.	Micromechanical Filters.....	5
2.2.	High-Q Micromechanical Resonator Oscillators.....	6
2.3.	Material Issues.....	6
3.0	SUMMARY OF KEY ACCOMPLISHMENTS	6
4.0	DETAILS FOR SELECT KEY ACCOMPLISHMENTS	8
4.1.	Micromechanical Resonator Frequency Extension	8
4.1.1.	Ratioed Folded-Beam Micromechanical Resonators.....	9
4.1.2.	Clamped-Clamped Beam Micromechanical Resonators	10
4.1.3.	Free-Free Beam Micromechanical Resonators.....	12
4.1.4.	Radial Contour-Mode Micromechanical Disk Resonators	13
4.1.5.	CVD Polydiamond Micromechanical Resonators	16
4.1.6.	Technology Transfer.....	20
4.2.	Micromechanical Resonator Oscillator Design and Demonstration.....	20
4.2.1.	A 10 MHz Micromechanical Resonator Pierce Oscillator	20
4.2.2.	Temperature Compensation.....	23
4.2.3.	Localized Annealing for Frequency Trimming	27
4.2.4.	Nickel Micromechanical Resonators, Q-Enhancement, and Aging Studies....	30
4.3.	Micromechanical Signal Processor Circuit Design and Demonstration.....	33
4.3.1.	Micromechanical Filters	33
4.3.2.	A Two-Resonator, Tunable, Switchable, VHF Micromechanical Filter	34
4.3.3.	High-Order Micromechanical Filters.....	38
4.3.4.	Parallel Microresonator Filters	40
4.3.5.	Micromechanical Mixer-Filters (“Mixlers”).....	42
4.4.	Other RF MEMS Devices.....	45
4.5.	Integrated MEMS/Transistor Merging Technologies.....	48
4.5.1.	High Aspect-Ratio Gaps and a Merged Single-Crystal Si/CMOS Process	48
4.5.2.	Nickel Micromechanical Resonators and Aging Studies.....	50
4.5.3.	Bonded-Microplatform MEMS/Transistor Merging Process	51
4.5.4.	Localized Heated Bonded Vacuum Encapsulation.....	56
5.0	SUMMARY	58
6.0	LIST OF PUBLICATIONS (over the period of this grant)	66
7.0	LIST OF INVITED PRESENTATIONS (over the period of this grant).....	70

List of Figures

Fig. 1: System-level schematic detailing the front-end design for a typical wireless transceiver. The off-chip, high- Q , passive components targeted for replacement via micromechanical versions (suggestions in lighter ink) are indicated in the figure.	2
Fig. 2: (a) A simple series resonant oscillator schematic (b) Bode plot for a low Q tank, indicating the Δf for a given $\Delta\theta$. (c) Similar to (b), but for a high Q tank.	3
Fig. 3: Simulated frequency characteristics for a 0.3% bandwidth, 70 MHz bandpass filter under varying tank Q 's.	4
Fig. 4: (a) Desired transfer function for an unterminated, ideal mechanical filter. (b) Mass-spring-damper model and equivalent electrical circuit (c) for a three-resonator mechanical filter explicitly depicting the electrical-to-mechanical analogy.	5
Fig. 5: Overhead-view schematics of (a) a conventional folded-beam micromechanical resonator; and (b) a ratioed folded-beam version, allowing control of truss velocity.	9
Fig. 6: (a) SEM of a ratioed folded-beam, comb-transduced micromechanical resonator (without inner electrodes). (b) Frequency characteristic for the device of (a) measured under 50 μ Torr vacuum using a drive voltage of $v_i=1\text{mV}$ and transresistance detection electronics with a gain of $100\text{k}\Omega$	9
Fig. 7: (a) SEM and (b) measured frequency characteristic (under 50 μ Torr vacuum) for a 9.66 MHz clamped-clamped beam evaluation resonator.	10
Fig. 8: (a) SEM of a 70 MHz clamped-clamped beam μ mechanical resonator. (b) Measured frequency characteristic for the resonator of (a).	11
Fig. 9: SEM of a 71MHz free-free beam micromechanical resonator.	12
Fig. 10: Measured spectra for (a) a 31.51MHz free-free beam μ resonator; and (b) a 92.25 MHz free-free beam μ resonator.	12
Fig. 11: Schematic of a contour-mode disk resonator with the preferred bias and excitation scheme.	13
Fig. 12: Predicted resonant frequency versus the radius of a radial contour mode disk fabricated in polysilicon.	13
Fig. 13: (a) SEM of a fabricated 156 MHz contour-mode disk μ mechanical resonator.	14
Fig. 14: Measured frequency characteristic for the contour-mode disk μ mechanical resonator of Fig. 13.	14
Fig. 15: SEM of a 10.47 MHz lateral free-free beam polysilicon μ mechanical resonator with metal electrodes and 1000\AA lateral electrode-to-resonator gaps.	14
Fig. 16: Process flow for the multiple-metal-electrode, sub-micron gap, polysilicon lateral μ resonator technology.	15
Fig. 17: (a) Wide-view and (b) zoom-in SEM's of a 3MHz CVD polydiamond CC-beam μ mechanical resonator with metal electrodes, all fabricated via the process of Fig. 18.	16
Fig. 18: Fabrication process flow for the polycrystalline diamond CC-beam resonator with metal electrodes.	17
Fig. 19: Frequency characteristic for a 2.94MHz CVD polydiamond CC-beam resonator.	18
Fig. 20: Frequency characteristic for a 4.21MHz CVD polydiamond CC-beam resonator.	18

Fig. 21: Plot of frequency versus beam length for the CVD diamond resonators of this work. (The points are measured data; the curve is the theoretical prediction of Eq. (5).)	19
Fig. 22: SEM of a 38.8 kHz CVD polydiamond folded-beam, comb-driven μ mechanical resonator.	19
Fig. 23: Frequency characteristic for a 38.8 kHz CVD polydiamond folded-beam μ mechanical resonator.	19
Fig. 24: Circuit schematics for the μ mechanical resonator oscillator of this work, using modified a Pierce configuration.	21
Fig. 25: Measured Fourier spectrum for the oscillator of Fig. 24, with an oscilloscope waveform in the inset.	22
Fig. 26: Measured Fourier spectrum showing second harmonic oscillator output.	22
Fig. 27: Phase noise versus frequency offset from the carrier for a 9.75 MHz CC-Beam Pierce oscillator and a 10 MHz crystal version. Theoretical phase noise plots for the CC-beam oscillator are also included.	22
Fig. 29: SEM of a 13.5 MHz mechanically temperature-compensated resonator: (a) Perspective view. (b) Close-up view around the electrodes.	23
Fig. 28: Perspective-view schematic of a mechanically temperature-compensated micromechanical resonator and test set-up.	24
Fig. 30: Plots of fractional frequency change versus temperature for temperature compensated micromechanical resonators with various $L1/L2$ compensation ratios.	24
Fig. 31: (a) Perspective schematic of a stiffness-compensated μ mechanical resonator, with effective cross-sections under different temperatures in (b) and (c).	25
Fig. 32: Process flow cross-sections for top metal electrode formation. (a) After standard surface micromachining, deposit top sacrificial oxide and seed layer. (b) After molded electroplating of sacrificial Ni spacer. (c) After molded electroplating of Au top electrode. (d) After HF release.	26
Fig. 33: SEM of a fabricated 10MHz stiffness-compensated temperature-insensitive micromechanical resonator, with an inset zoom in on the gap.	27
Fig. 34: Measured frequency characteristic for the 10MHz stiffness compensated resonator of Fig. 33. (The inset shows the measurement set-up.)	27
Fig. 35: Plot of fractional frequency change versus temperature for the 10MHz stiffness-compensated resonator of Fig. 33. Plotted as a function of the TC_f control voltage, (V_P-V_C)	27
Fig. 36: Perspective-view schematic depicting details of the filament annealing procedure, showing circuit details and indicating key components.	28
Fig. 37: Plot of frequency change versus anneal trial with the number of pulses as a third variable, indicating some consistency from trial to trial for a given resonator.	28
Fig. 38: Nickel surface micromachining process flow.	29
Fig. 39: SEM for a folded-beam, comb-driven Ni μ mechanical resonator using the new rigid-anchor process flow.	30
Fig. 40: SEM of a geometric-stress compensated nickel micromechanical resonator.	30
Fig. 41: FEM simulation of the temperature distribution on a localized annealed nickel micromechanical resonator.	30

Fig. 42: Frequency versus time plot summarizing the procedure used to enhance the Q and frequency stability of a nickel micromechanical resonator.	31
Fig. 43: Measured spectra for a nickel micromechanical resonator operated at a pressure of 30mTorr and a temperature of 47°C before and after localized annealing.	32
Fig. 44: (a) Equivalent lumped parameter mechanical circuit for a mechanical filter. (b) Corresponding equivalent LCR network.	33
Fig. 45: Mode shapes of a three-resonator micromechanical filter and their corresponding frequency peaks.	33
Fig. 46: (a) Perspective-view schematic of a two-resonator VHF μ mechanical filter with typical bias, excitation, and signal conditioning electronics. (b) Electrical equivalent circuit for the filter in (a). Here, m_r , k_r , and c_r denote the mass, stiffness, and damping of the (identical) resonators at the drive electrode locations, and $\eta_e = V_P(\partial C/\partial x)$ and $\eta_c = (k_{rc}/k_r)^{0.5}$ are turns ratios modeling electromechanical coupling at the inputs and mechanical impedance transformations at low velocity coupling locations.	35
Fig. 47: Filter schematics showing (a) maximum velocity coupling to yield a large percent bandwidth and (b) low velocity coupling to yield a smaller percent bandwidth.	37
Fig. 48: SEM of a 34.5 MHz switchable, tunable, μ mechanical filter with important dimensions.	38
Fig. 49: Measured transmission spectrum for a VHF two-resonator micromechanical filter, such as shown in Fig. 48.	38
Fig. 50: Perspective view schematic of the designed three-resonator micromechanical filter, showing the equivalence to a lumped mass-spring-damper mechanical circuit.	39
Fig. 51: Wide-view and close-in SEM's of a fabricated three-resonator micromechanical filter.	40
Fig. 52: Measured frequency spectrum for the filter of Fig. 51.	40
Fig. 53: Schematic of a parallel-resonator filter, indicating the required bias and excitation scheme, and identifying key components.	41
Fig. 54: Bode plot depiction of the mechanism behind parallel microresonator bandpass filters.	42
Fig. 55: Measured frequency spectrum for a 15 MHz parallel-resonator filter.	42
Fig. 56: Simplified block diagram of a wireless receiver, indicating (with shading) the components replaceable by the subject mixer+filter devices.	43
Fig. 57: (a) Schematic diagram of the described μ mechanical mixer+filter, depicting the bias and excitation scheme needed for down-conversion. (b) Equivalent block diagram of the mixer+filter scheme.	43
Fig. 58: SEM's of the 34.5MHz micromechanical mixer+filter: (a) Top perspective view. (b) Low angle view. Dimensions for the indicated geometries are given in Table II.	44
Fig. 59: Experimental set-up for mixer+filter evaluation.	44
Fig. 60: Spectrum obtained when sweeping the RF input ν_{RF} over a 47MHz to 55MHz frequency range while detecting and holding outputs (using the MAX HOLD function on an HP 8561E Spectrum Analyzer) over a 15MHz to 55MHz range. Note that some peaking is seen in the filter spectrum, because the micromechanical filter is not terminated exactly. A flatter spectrum is achievable with proper termination.	44
Fig. 61: Micromachined tunable capacitor. (a) Conceptual schematic. (b) Actual structure designed with a lateral spring.	45

Fig. 62: Simplified fabrication process for the tunable-dielectric micromechanical capacitor.	46
Fig. 63: SEM of a fabricated lateral spring movable-dielectric micromechanical capacitor.....	46
Fig. 64: Measured capacitance versus actuation voltage of the fabricated device with a lateral spring.....	47
Fig. 65: Measured and circuit-modeled RF characteristics of the fabricated device with a lateral spring (a) 0V bias (b) 10V bias.....	46
Fig. 66: Smith chart showing measured and predicted S11 parameters of the fabricated device with a lateral spring (0V bias).....	47
Fig. 67: A tunable capacitor with a vertical spring. (a) Device structure. (b) SEM photomicrograph of the fabricated device. (c) RF characteristic for both 0V and 10V bias voltage. (d) Measured tuning characteristic.	47
Fig. 68: 30 kHz micromechanical resonator integrated with BiCMOS detection circuitry.....	49
Fig. 69: Cross-sectional process flow for the merged CMOS+ μ Structures technology.....	49
Fig. 70: SEM showing 0.1 μ m-wide gaps between 2 μ m-wide cantilever beams, etched in 3.1 μ m-thick single-crystal silicon using a high-density ICP Cl2-etch.	50
Fig. 71: SEM of a μ platform housing a 40 MHz, two-resonator CC-beam μ mechanical filter	51
Fig. 72: Illustration of the procedure for achieving a combined MEMS/transistor chip via the described flip-bond-and-tear process. (a) Bonding. (b) Final cross-section.....	52
Fig. 73: Schematic showing cross-sections of the μ platform fabrication process flow.	52
Fig. 74: SEM showing the cross-sectional view of the μ platform.....	53
Fig. 75: SEM showing the solder bumps deposited on the BiCMOS wafer.....	53
Fig. 76: A μ mechanical filter circuit showing both the transistor level electronics and the bonded platform: (a) Top view; (b) Perspective view.	53
Fig. 76: Frequency response of a 6MHz μ resonator (a) before bonding and (b) after bonding.	54
Fig. 77: Frequency response of a 40MHz μ resonator (a) before bonding and (b) after bonding.	54
Fig. 78: Frequency response of a 9MHz μ resonator with (a) 350Å gap (b) 1000Å gap.	54
Fig. 80: Frequency response of a 40MHz filter (a) before bonding and (b) after bonding.	55
Fig. 81: Layout and cross-section for a μ mechanical resonator with overhead for encapsulation via solder-based localized heating.	55
Fig. 82: Process flow for wafer-level vacuum encapsulation of micromechanical resonators via localized heated bonding.....	56
Fig. 83: Measured frequency characteristic for a polysilicon folded-beam μ mechanical resonator vacuum encapsulated using the localized heated bonding technique of Fig. 81.	57
Fig. 82: SEM of a previously encapsulated micromechanical resonator with glass cap forcibly removed (i.e., broken).....	58
Fig. 84: Plot of pressure versus time for a vacuum encapsulated resonator such as shown in Fig. 83.	58
Fig. 85: System block diagram for an RF channel-select receiver architecture utilizing large numbers of micromechanical resonators in banks to trade Q for power consumption. (On-chip μ mechanics are shaded.)	60

Fig 86: System block diagram for an all-MEMS receiver front-end, employing an RF image-reject filter, a fixed μ mechanical resonator local oscillator, and a switchable array of IF mechanical mixer-filters.....	61
---	----

List of Tables

Table I: Environmental Q-Degradation and Anneal-Activated Restoration	33
Table II: Dimensions.....	44

1.0 PROJECT GOALS

The majority of the high- Q bandpass filters commonly used in the RF and IF stages of heterodyning transceivers are realized using off-chip, mechanically-resonant components, such as crystal filters and SAW devices. Due to higher quality factor Q , such technologies greatly outperform comparable filters implemented using transistor technologies, in insertion loss, percent bandwidth, and achievable rejection [1,2]. High Q is further required to implement local oscillators or synchronizing clocks in transceivers, both of which must satisfy strict phase noise specifications. Again, off-chip elements (e.g., quartz crystals) are utilized for this purpose. Being off-chip components, the above mechanical devices must interface with integrated electronics at the board level, and this constitutes an important bottleneck to miniaturization and performance of heterodyning transceivers. For this reason, recent attempts to achieve single-chip transceivers for paging and cellular communications have utilized direct conversion architectures, rather than heterodyning, that attempt to eliminate some of the off-chip high- Q components, but that have suffered in overall performance as a result [3]. In this respect, single-chip solutions to heterodyning transceivers are desirable.

The rapid growth of micromachining technologies, which yield high- Q on-chip vibrating mechanical resonators [4], may now make miniaturized, single-chip heterodyning transceivers possible. With Q 's of over 80,000 [5] under vacuum and center frequency temperature coefficients in the range of -10 ppm/ $^{\circ}\text{C}$ (several times less with nulling techniques) [6], polycrystalline silicon micromechanical resonators (abbreviated “ μ resonators”) can serve well as miniaturized substitutes for crystals in a variety of high- Q oscillator and filtering applications. The primary objectives of this project are (1) identification and study of the physical performance limitations incurred when extending the frequency range of miniaturized, micro-scale mechanical resonators to the VHF, UHF, and S-Band ranges; (2) implementation of prototype high- Q micromechanical filters and oscillators in these frequency ranges; and (3) subsequent incorporation of these components into the RF and IF stages of compact, inexpensive wireless transceivers. The proposed devices are not only orders of magnitude smaller than existing discrete resonator equivalents, but are also expected to outperform their macroscopic counterparts in insertion loss and percent bandwidth.

1.1. *Miniaturization of Transceivers*

To illustrate more concretely the specific transceiver functions that benefit from micromechanical implementation, Fig. 1 presents the system-level schematic for a typical super-heterodyne wireless transceiver. As implied in the figure, several of the constituent components can already be miniaturized using integrated circuit transistor technologies. These include the low noise amplifiers (LNA's) in the receive path, the solid-state power amplifier (SSPA) in the transmit path, synthesizer phase-locked loop (PLL) electronics, mixers, and lower frequency digital circuits for baseband signal demodulation. Due to noise, power, and frequency considerations, the SSPA (and sometimes the LNA's) are often implemented using compound semiconductor technologies (i.e., GaAs). Thus, they often occupy their own chips, separate from the other mentioned transistor-based components, which are normally realized using silicon-based bipolar and CMOS technologies. However, given the rate of improvement of silicon technologies (silicon-germanium included [7]), it is not implausible that all of the above functions could be integrated onto a single-chip in the foreseeable future.

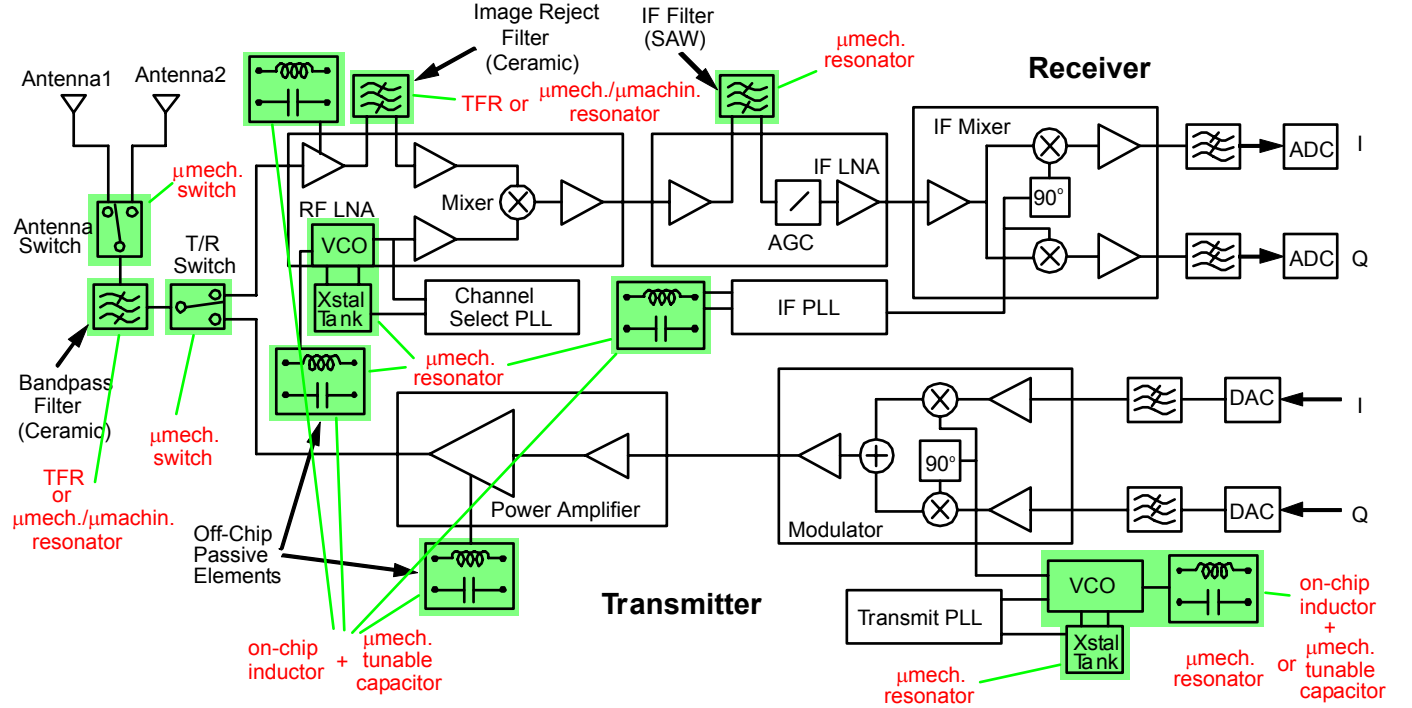


Fig. 1: System-level schematic detailing the front-end design for a typical wireless transceiver. The off-chip, high- Q , passive components targeted for replacement via micromechanical versions (suggestions in lighter ink) are indicated in the figure.

Unfortunately, placing all of the above functions onto a single chip does very little towards decreasing the overall super-heterodyne transceiver size, which is dominated not by transistor-based components, but by the numerous passive components indicated in Fig. 1. The presence of so many frequency-selective passive components is easily justified when considering that communication systems designed to service large numbers of users require numerous communication channels, which in many implementations (e.g., Time Division Multiple Access (TDMA)) must have small bandwidths and must be separable by transceiver devices used by the system. The requirement for small channel bandwidths results in a requirement for extremely selective filtering devices for channel selection and extremely stable (noise free) local oscillators for frequency translation. For the vast majority of military communication standards, as well as for commercial cellular and cordless standards, the required selectivity and stability can only be achieved using high- Q components, such as discrete inductors, discrete tunable capacitors (i.e., varactors), and SAW and quartz crystal resonators, all of which interface with IC components at the board level. The needed performance cannot be achieved using conventional IC technologies, because such technologies lack the required Q . It is for this reason that virtually all military transceivers and commercially available cellular and cordless phones contain numerous passive SAW and crystal components.

1.2. The Need for High Q in Oscillators.

For any communications application, the stability of the oscillator signals used for frequency translation, synchronization, or sampling, is of utmost importance. Oscillator frequencies must be stable against variations in temperature, against aging, and against any phenomena, such as noise or microphonics, that cause instantaneous fluctuations in phase and frequency. The single most important parameter that dictates oscillator stability is the Q of the frequency-setting tank (or of the effective tank for the case of ring oscillators). For a given application, and assuming a

finite power budget, adequate long- and short-term stability of the oscillation frequency is insured only when the tank Q exceeds a certain threshold value.

The correlation between tank Q and oscillator stability can be illustrated heuristically by considering the simple oscillator circuit depicted in Fig. 2(a). Here, a series resonant oscillator is shown, comprised of a sustaining amplifier and an LC tank connected in a positive feedback loop. For proper start-up and steady-state operation, the total phase shift around the loop must sum to zero. Thus, if at the oscillation frequency the amplifier operates nominally with a 0° phase shift from its input to its output, then the tank must also have a 0° phase shift across its terminals. Given this, and referring to any one of the tank response spectra shown in Figs. 2(b) or (c), this oscillator is seen to operate nominally at the tank resonance frequency.

If, however, an external stimulus (e.g., a noise spike, or a temperature fluctuation) generates a phase shift $-\Delta\theta$ across the terminals of the sustaining amplifier, the tank must respond with an equal and opposite phase shift $\Delta\theta$ for sustained oscillation. As dictated by the tank transfer functions of Fig. 2, any tank phase shift must be accompanied by a corresponding operating frequency shift Δf . The magnitude of Δf for a given $\Delta\theta$ is largely dependent on the Q of the resonator tank. Comparison of Fig. 2(b) with (c) clearly shows that a given phase shift incurs a much smaller frequency deviation on the tank with the higher Q . Thus, the higher the tank Q , the more stable the oscillator against phase-shifting phenomena.

To help quantify the above heuristic concepts, one important figure of merit for oscillators is the phase noise power present at frequencies close to the carrier frequency. Typical phase noise requirements range from -121 dBc/Hz at 600 kHz deviation from a 1.8 GHz carrier in DCS1800 European Global System for Mobile Telecommunications (GSM) cellular phones [8], to -150 dBc/Hz at 67 kHz carrier deviations in X-Band, Doppler-based radar systems [9]. Through a more rigorous analysis of Fig. 1 (assuming linear operation), the phase noise of a given oscillator can be described by the expression [10], [11]:

$$\left(\frac{N_{op}}{C} \right)_{f_m} = \frac{FkT}{C} \frac{1}{8Q^2} \left(\frac{f_o}{f_m} \right)^2 [dBc/Hz], \quad (1)$$

where $(N_{op}/C)_{f_m}$ is the phase noise power density-to-carrier power ratio at a frequency f_m offset from the carrier frequency, F is the noise figure of the active device evaluated using the total oscillator power P , C is the carrier power delivered to the load, and f_o is the carrier frequency. From (1), phase noise is seen to be inversely proportional to the square of Q , and directly proportional to the amplifier noise figure F . Given that F can often be reduced by increasing the operat-

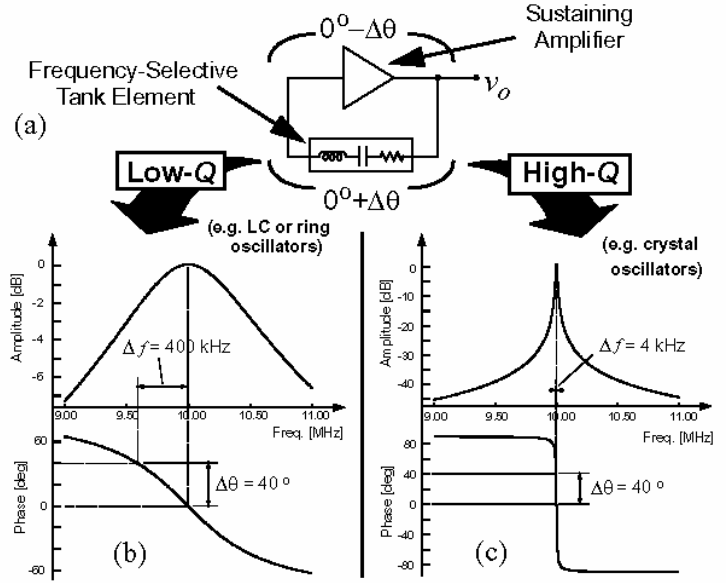


Fig. 2: (a) A simple series resonant oscillator schematic (b) Bode plot for a low Q tank, indicating the Δf for a given $\Delta\theta$. (c) Similar to (b), but for a high Q tank.

ing power P of the sustaining amplifier, (1) then can be interpreted as implying that power and Q can be traded to achieve a given phase noise specification. Given the need for low power in portable units, and given that the synthesizer (containing the reference and VCO oscillators) is often a dominant contributor to total transceiver power consumption, modern transceivers could benefit greatly from technologies that yield high- Q tank components.

1.3. The Need for High Q in Filters.

Tank Q also greatly influences the ability to implement extremely selective IF and RF filters with small percent bandwidth, small shape factor, and low insertion loss. To illustrate, Fig. 3 presents simulated frequency characteristics under varying resonator tank Q 's for a 0.3% bandwidth bandpass filter centered at 70 MHz, realized using the typical LC resonator ladder configuration shown in the insert. As shown, for a resonator tank Q of 10,000, very little insertion loss is observed. However, as tank Q decreases, insertion loss increases very quickly, to the point where a tank Q of 1,000 leads to 20 dB of insertion loss—too much even for IF filters, and quite unacceptable for RF filters. As with oscillators, high- Q tanks are required for RF and IF filters alike, although more so for the latter, since channel selection is done predominantly at the IF in super-heterodyne receivers. In general, the more selective the filter, the higher the resonator Q required to achieve a given level of insertion loss. In particular, the above 0.3% bandwidth filter example applies for IF filters, which, because of their high selectivity, are best implemented with resonator Q 's exceeding 5,000; RF pre-select or image-reject filters, on the other hand, typically require only 3% bandwidths and can thus be implemented using resonators with Q 's on the order of 500-1,000.

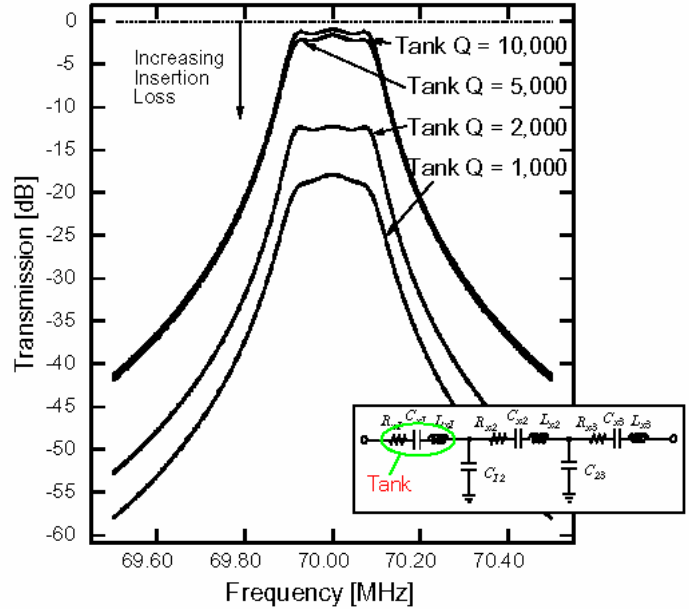


Fig. 3: Simulated frequency characteristics for a 0.3% bandwidth, 70 MHz bandpass filter under varying tank Q 's.

2.0 APPROACH/PROBLEMS TO BE ADDRESSED

As detailed in the original proposal, this project features several tasks aimed at realizing the frequency-selective off-chip components required in wireless communication transceivers. Among the specific components of interest are IF and RF filters, low phase noise reference oscillators, high- Q voltage-controlled oscillators (VCO's), codes that automate the design of these components, and special packaging procedures for vacuum encapsulation and electrical isolation.

2.1. Micromechanical Filters.

The high- Q filters of interest are comprised of micromachined mechanical resonators coupled by soft mechanical springs, as depicted in Fig. 4(b) using a mass-spring-damper representation. This coupled three-resonator system has three modes of vibration that form the passband of the resultant filter, as shown in the input force-to-output displacement transfer function of Fig. 4(a). The separation between the modes (i.e., the bandwidth of the resultant filter) is determined primarily by the stiffnesses of the coupling springs. The absolute center frequency of the filter is determined primarily by the resonance frequencies of the constituent resonators.

In actual design of these filters, electromechanical analogies are used, where the electrical domain inductance and capacitance of a properly synthesized LC ladder filter are implemented via analogous values of compliance and mass in the mechanical domain. Figure 1(c) explicitly shows the electrical to mechanical equivalence. Here, vibrating resonators in the mechanical domain equate to LCR tanks in the electrical domain, while coupling springs are analogous to coupling capacitors.

To date low frequency prototypes of such filters have been demonstrated using micromachining technologies [12]. Extensions to the higher VHF or UHF ranges and incorporation into single-chip transceivers are the subject of the present research proposal, and will require investigations on all aspects, from material and mechanical design, to circuit modeling and transducer design, to fabrication technology design. In particular, tenth-micron-scale technology will play a key role in making communications-grade micromechanical filters possible. To see this, consider that a general equation for mechanical resonance frequency ω_o may be expressed as

$$\omega_o = \sqrt{\frac{k_r}{m_r}}, \quad (2)$$

where m_r is the effective (distributed) mass of the resonator, and k_r is the system spring constant. Equation (2) suggests that resonator designs with frequencies in the VHF to UHF range will require both high spring stiffness and very small mass. The latter requirement (small mass) stipulates that micro-scale resonators be realized. Furthermore, the requirement for high spring stiff-

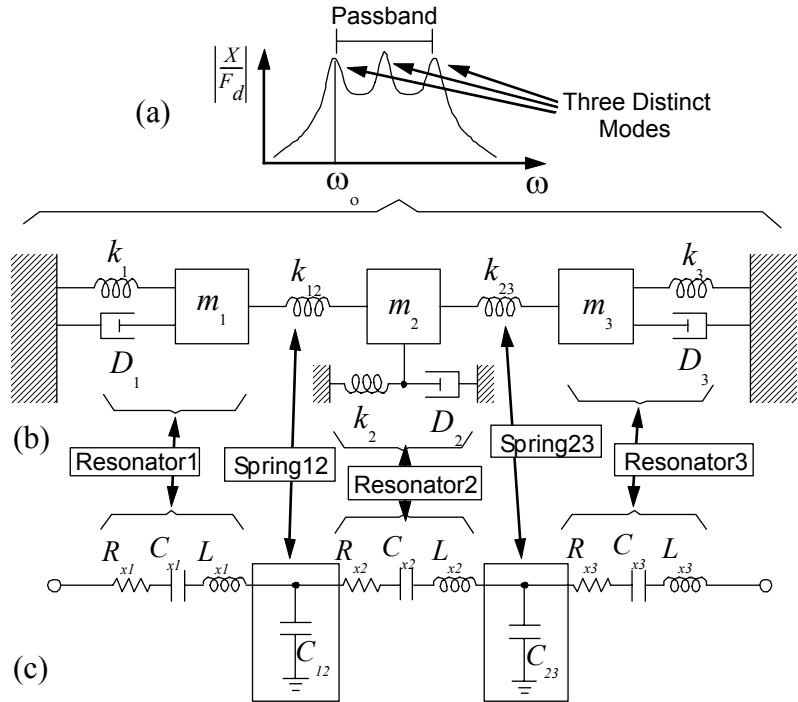


Fig. 4: (a) Desired transfer function for an unterminated, ideal mechanical filter. (b) Mass-spring-damper model and equivalent electrical circuit (c) for a three-resonator mechanical filter explicitly depicting the electrical-to-mechanical analogy.

ness results in a simultaneous requirement for large electromechanical transducer coupling [13]. Large coupling both suppresses noise due to Brownian motion of the mechanical resonator and enhances the utility of such resonators from a design standpoint. For the case of the capacitively transduced resonators under study, this requirement for large electromechanical coupling may necessitate tenth-micron-scale gaps between the resonator and transducing electrodes.

2.2. *High- Q Micromechanical Resonator Oscillators.*

The above frequency extension issues translate directly to high frequency, high- Q oscillator implementation, as well. However, for the case of oscillators used in communications, there is the additional requirement for enhanced temperature and aging stability, which may require more advanced resonator topologies, on-chip ovens, and/or on-chip temperature compensation circuitry. Furthermore, because Q greatly influences the overall short- and long-term stability of oscillators (phase noise decreases quadratically with increasing Q), the requirement of high Q is more pressing for oscillators than for filters. Balanced anchor designs (i.e., tuning fork designs) that minimize losses to the substrate are expected to greatly influence the performance of oscillators referenced to micromechanical resonators. For the case of voltage-controlled oscillators (VCO's), resonator designs that allow substantial tuning of the resonance frequency are required. Alternative transducer and anchor designs may play significant roles in achieving adequate voltage-controlled tuning range.

2.3. *Material Issues.*

In addition to the above scaling and design issues, the *intrinsic* Q and its dependence on frequency is of interest, since the proposed communications applications are heavily dependent upon the high- Q of micromechanical resonators. In particular, for the case of oscillators, phase noise decreases quadratically with increasing Q . For the case of micromechanical filters, the Q of the constituent mechanical resonators largely determines the minimum insertion loss achievable. Since different materials will exhibit different dissipation mechanisms, temperature dependencies, and aging rates, it is instructive to investigate the performance of filters constructed in a variety of materials and with several resonator geometries, such as tuning fork types.

3.0 SUMMARY OF KEY ACCOMPLISHMENTS

To provide a broad perspective for the reader's convenience, the following comprises a bulleted summary of key accomplishments achieved over the period of this grant:

- Invented and demonstrated electrical stiffness compensation, in which a metal electrode is strategically added around a resonator structure to introduce a temperature-dependent *electrical* stiffness that counteracts frequency shifts due to Young's modulus temperature dependence. Using this technique, micromechanical resonators have now been achieved with temperature independencies that rival those of the best AT-cut quartz crystals.
- Demonstrated the first HF range micromechanical resonators constructed of chemical vapor deposited (CVD) polycrystalline diamond material that exhibit resonance frequencies 80% higher than attainable via equivalent polysilicon devices, while posting Q 's on par with them. With its higher acoustic velocity, polydiamond has great potential for more easily achieving the coveted UHF frequencies (0.3-3 GHz) required for use in wireless communication transceivers.

- Invented and demonstrated a bonded-microplatform process for integration of micromechanics and transistor circuits, where suspended-platform-mounted micromechanics are bonded to a transistor circuit wafer, then torn away from a carrier wafer to remain on the transistor wafer.
- Invented and demonstrated geometric-stress compensation, in which geometric design is used to introduce a temperature-dependent *mechanical* stiffness that nulls out frequency shifts due to Young's modulus temperature dependence.
- Derived an analytical explanation for the $1/f^3$ phase noise component seen in the output of a μ mechanical resonator oscillator using an off-chip sustaining amplifier.
- Developed and demonstrated mixer-based measurement techniques to facilitate the characterization of micromechanical disk resonators operating at UHF frequencies.
- Invented and demonstrated a 156 MHz radial contour-mode vibrating mechanical disk resonator with a Q of 9,400.
- Invented and demonstrated a process technology that combines surface-micromachining, metal electroplating, and a sacrificial sidewall spacer technique to achieve polysilicon microstructures and metal electrodes with sub-micron lateral electrode-to-resonator gaps.
- Invented and demonstrated a micromechanical tunable dielectric capacitor that has achieved a Q of 291 at 1 GHz.
- Invented and demonstrated vacuum-encapsulated micromechanical resonators using a locally-heated solder-bonding technique, in which a glass cap is bonded over a wafer containing micromechanical resonators to them within an enclosure defined by the cap and wafer substrate. This wafer-level vacuum package has now held a vacuum pressure of 25 mTorr for more than 1.5 years.
- Demonstrated a 10 MHz micromechanical resonator oscillator using an off-chip sustaining circuit, and in measuring the phase noise performance of this oscillator, identified a $1/f^3$ phase noise component not normally seen in comparable quartz crystal oscillators. The $1/f^3$ phase noise component has been modeled and steps are being taken to remove it via DARPA-funded research.
- Demonstrated a lateral FF-beam micromechanical resonator for which the Q can be optimized via proper selection of a dc-bias voltage.
- Demonstrated two-resonator micromechanical filters with passbands centered around 68 MHz, passband rejections in excess of 25 dB, and insertion losses less than 5 dB. These filters used clamped-clamped beam micromechanical resonators.
- Wrote codes to automatically generate micromechanical filters and mixer-filters ("mixlers") to satisfy specific sets of specifications.
- Demonstrated micromechanical mixer-filter devices that allow both mixing and filtering in a single passive device. (This work won the Roger A. Haken Best Student Paper Award at the 1998 IEEE Int. Electron Devices Meeting.)
- Developed complete models for two-resonator filters using clamped-clamped beam resonators capable of predicting correctly the required termination resistance and dimensions for a given specification, capable of explaining the peaking effect seen in higher frequency filters, and capable of predicting the IIP_3 of capacitively-transduced micromechanical resonators.
- Developed processing techniques realizing micromechanical resonators with 300 Å electrode-to-resonator gaps with high yield.
- Demonstrated virtually-levitated, free-free beam micromechanical resonators with Q 's of up to 14,000 operating at VHF frequencies of up to 93 MHz.

- Demonstrated geometric stress-compensated micromechanical resonator designs for folded-beam nickel resonators that greatly reduce temperature dependencies (down to 2ppm/°C).
- Demonstrated a three-resonator, spring-coupled micromechanical filter at 340 kHz with a percent bandwidth of 0.09%, less than 0.6 dB of insertion loss, and more than 64 dB of passband rejection. This was achieved using a new ratioed-folded beam resonator design.
- Fabricated nickel resonators with Q 's up to 14,000.
- Investigated the use of in situ localized annealing techniques to not only improve the long-term stability and quality factor of nickel micromechanical resonators, but also to recover the Q 's of resonators exposed to various environmental contaminants.
- Completed layout for fully-integrated reference oscillators and for frequency- and bandwidth-tunable micromechanical filters with automatic passband correction circuitry. A platform-bonding process to combine Analog Devices BiCMOS circuits with micromechanics has been successfully completed, and integrated microsystems have been evaluated.
- Finished several fabrication runs for resonator samples to be sent to various government and military agencies and services for stability evaluation. Completed samples have now been sent to AFRL, CECOM, the MAYO Foundation, and Raytheon TI-Systems.
- Achieved 0.1 μm vertical gaps in 3.1 μm -thick single-crystal silicon using ICP etching.
- Demonstrated a process technology combining CMOS and high-aspect-ratio single-crystal silicon micromechanical resonators with 1000 Å lateral gaps achieved using e-beam lithography.

4.0 DETAILS FOR SELECT KEY ACCOMPLISHMENTS

The efforts over the past four years under this grant have yielded enormous progress towards the development of micromechanical signal processing circuits for communication applications, much more than can possibly be detailed completely in just one final report. As such, only a highlighted subset of accomplishments are presented in this section, and these are presented within the context of four major thrusts identified for this research: (1) micromechanical resonator frequency extension; (2) micromechanical resonator oscillator design and demonstration; (3) micromechanical signal processor circuit design and demonstration; and (4) merging technologies for micromechanics and transistor integrated circuits.

4.1. *Micromechanical Resonator Frequency Extension*

At the time this grant started, micromechanical resonators were used mainly in resonant sensor applications, where frequency changes in relatively low frequency resonators (with resonance frequencies lower than 100 kHz) were used to sense physical phenomena capable of perturbing resonance frequencies (e.g., temperature, pressure, stress, mass). Signal processing applications for micromechanical resonators were only very recently invented at the time, and the technology for this application was in its infancy.

Due to their analytical simplicity and familiarity at the start of this grant, folded-beam, comb-driven micromechanical resonators were the design of choice at the time, so this work began with such resonators, with the intent of starting conservatively. Although the frequency range of such resonators was greatly limited, these devices proved instrumental in provided much-needed insight into the needs of future resonators for oscillator and filter design. In particular, the first instances of localized annealing for frequency trimming and Q -enhancement (to be detailed later in Section 4.2.3) were demonstrated using folded-beam resonators, as were the first micromechanical filters and nickel devices.

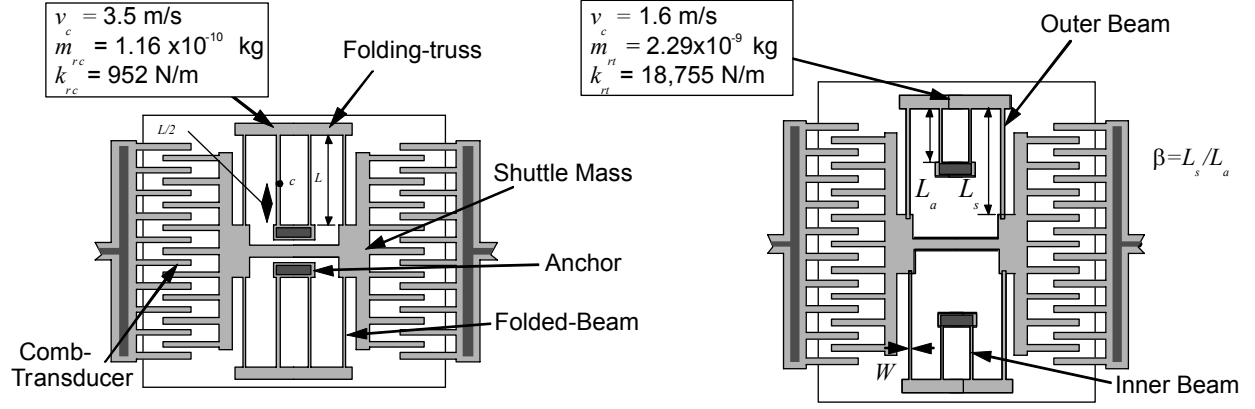


Fig. 5: Overhead-view schematics of (a) a conventional folded-beam micromechanical resonator; and (b) a ratioed folded-beam version, allowing control of truss velocity

4.1.1. Ratioed Folded-Beam Micromechanical Resonators

One novel rendition of a folded-beam, comb-driven resonator introduced near the beginning of this grant is the ratioed-folded-beam resonator [14], shown in Fig. 5(b) in comparison with a conventional folded-beam resonator shown in Fig. 5(a). As indicated in the figure, the ratioed folded-beam resonator allows the designer to control the velocity of the folding truss, where resonator-to-resonator coupling occurs in the particular filter design of Fig. 50 (to be discussed). Since the equivalent dynamic mass and stiffness of a given resonator is a strong function of the velocity at the location in question, control of velocity corresponds to control of the resonator stiffness at the coupling location. From the expression for filter bandwidth,

$$BW = \left(\frac{f_o}{k_{ij}} \right) \left(\frac{k_{sij}}{k_r} \right), \quad (3)$$

where f_o is the center frequency, k_{sij} is the stiffness of the coupling beam, k_r is the stiffness of the resonator at the coupling location, and k_{ij} is a normalized coupling coefficient found in filter cookbooks [16],

the bandwidth of a micromechanical filter is clearly controllable via adjustment of the resonator stiffness at the coupling location k_r . Note from (3) that filter bandwidth is not dependent on the absolute values of resonator and coupling beam stiffness; rather, their ratio k_{sij}/k_r dictates bandwidth. This implies that filter bandwidth is controllable by simply varying the ratio $\beta = (L_s/L_a)$,

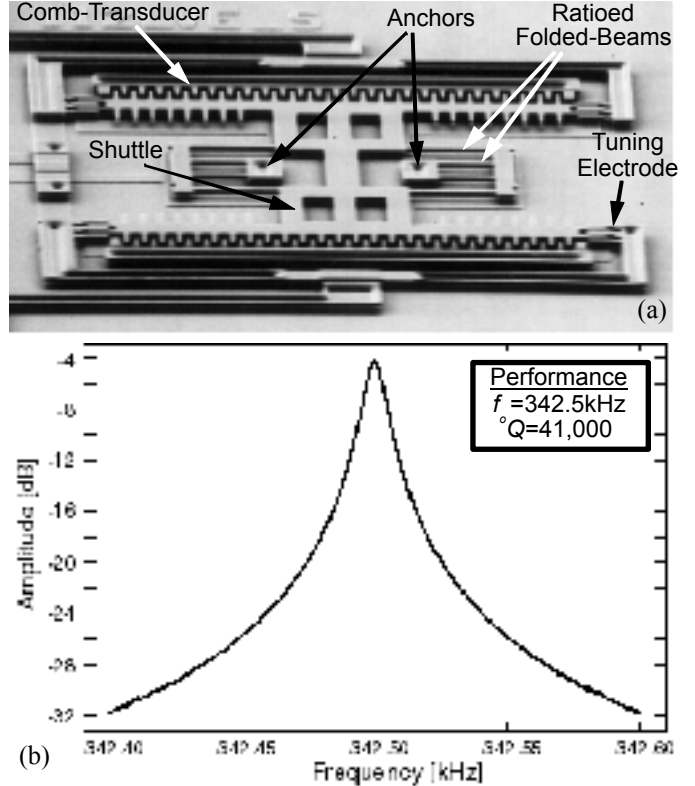


Fig. 6: (a) SEM of a ratioed folded-beam, comb-transduced micromechanical resonator (without inner electrodes). (b) Frequency characteristic for the device of (a) measured under 50 μ Torr vacuum using a drive voltage of $v = 1$ mV and transresistance detection electronics with a gain of 100k Ω .

where L_s and L_a are outer and inner folded-beam lengths, respectively (see Fig. 5(b)). This low-velocity coupling technique becomes particularly important when realizing filters with extremely small bandwidths (such as in Fig. 50), which without low-velocity coupling, would require sub-micron coupling beam dimensions.

Figure 6 presents the SEM and measured spectrum for a 342.5 kHz ratioed folded-beam micromechanical resonator with a measured Q of 41,000 under vacuum. The use of the resonator of Fig. 6 in a three-resonator medium frequency (MF) micromechanical filter will be discussed later in Section 4.3.3 of this document.

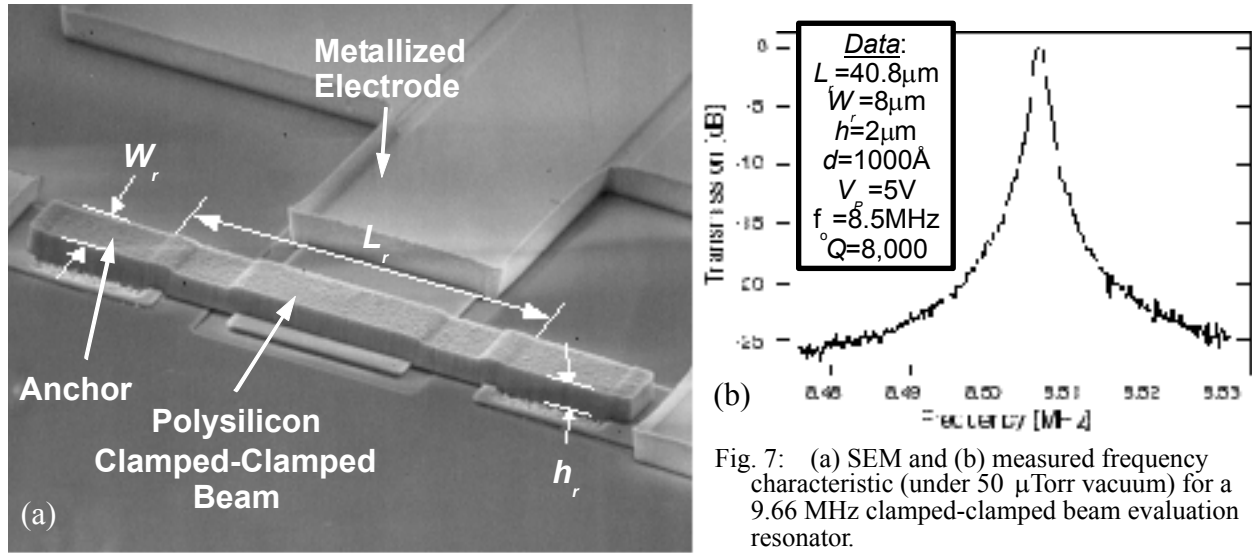


Fig. 7: (a) SEM and (b) measured frequency characteristic (under 50 μTorr vacuum) for a 9.66 MHz clamped-clamped beam evaluation resonator.

4.1.2. Clamped-Clamped Beam Micromechanical Resonators

Again, although they did help to accelerate the understanding and development of filter design methodologies using micromechanical resonators, folded-beam resonators were too massive to be practically applied to filters with center frequencies higher than medium frequency (MF). Recognizing this, less massive resonator designs were then pursued for higher operation frequencies, and it was actually the simplest of these, the clamped-clamped beam (“CC-beam”, c.f., Fig. 7 [15]), that proved most useful for exploring high frequency (HF; 3-30 MHz) to very high frequency (VHF; 30-300 MHz) micromechanical circuit designs (to be detailed in Section 4.3). These clamped-clamped beams were essentially guitar strings shrunk down from the macro-scale (e.g., 25 inches for a typical guitar string) to the micro-scale (e.g., 10 μm , representing orders of magnitude size reduction) and made in a polysilicon material (rather than metal) to achieve vibrational resonance frequencies many orders of magnitude higher than that achievable by guitar strings, and with much better frequency selective properties. The particular beam depicted in Fig. 7 is 40.8 μm -long, 2 μm -thick, and 8 μm -wide, and can be driven electrostatically via the underlying electrode to vibrate at an 8.5 MHz resonance frequency with a Q of up to 8,000 under vacuum. Given a suitable technology to provide an appropriate vacuum environment (see Section 4.5.4), the on-chip Q of 8,000 shown in Fig. 7(b) is quite useful both filtering and oscillator applications in communication transceivers.

Unfortunately, although simple and convenient to use for such applications, the CC-beam resonator of Fig. 7 has one major flaw that restricts its practical use to frequencies below 100 MHz. Specifically, as its dimensions are scaled for frequencies past 30 MHz, it begins to lose an exces-

sive fraction of its total energy to the substrate through its anchors. To illustrate this Q -degradation phenomenon, Fig. 8 presents the SEM and measured frequency characteristic for a 14 μm -long, 2 μm -thick, and 8 μm -wide CC-beam resonator, exhibiting a resonance frequency of 71.8 MHz, but showing a much Q of only 300, which is much degraded from the $Q \sim 8,000$ for the 8.5 MHz version of Fig. 7). The observed decrease in Q comes about mainly because the stiffness of the resonator increases rapidly as its length is shortened to allow higher frequency. With this increased stiffness, as the resonator beam vibrates, a larger amount of force is exerted on the substrate at its anchors, resulting in more energy radiated (and lost) into the substrate, and in turn leading to a much lower Q . This mechanical (or acoustic) substrate loss mechanism might be perceived as somewhat analogous to substrate loss mechanisms seen in the electrical domain for LC tank resonators using spiral inductors achievable by conventional IC technology. For such spiral inductors, problems with substrate loss have so far proven insurmountable if a micro-scale, small form factor solution is desired. Fortunately, however, where design inflexibility in the electrical domain precludes a micro-scale solution to electrical substrate losses, design in the mechanical domain is quite flexible, and several solutions have now been pursued via this grant to combat anchor dissipation.

Perhaps the simplest approach to combating anchor dissipation is to prevent huge increases in stiffness as higher frequencies are attained. This can be done by scaling not only the length dimension of a CC-beam resonator, but also its width and thickness dimensions. With this strategy, very high frequency resonators can be attained. For example, a 100 MHz resonator can be achieved with a length of 2.6 μm , a width of 1000 \AA , and a thickness of 1000 \AA , while exhibiting a stiffness of only 9.3 N/m. This is many times smaller than the 66,000 N/m of an 11.4 μm -long, 8 μm -wide, 2 μm -thick version at the same frequency, and thus, the smaller resonator should exhibit smaller anchor losses, and thus, a better Q . Unfortunately, however, due to its sheer lack of size, such a tiny resonator does not have the power handling ability to even satisfy present-day commercial communications requirements, let alone military requirements, which are many times more demanding. Thus, especially for wireless applications in hostile military environments, it would be much preferred if the width and thickness dimensions of a flexural beam resonator could remain sizable (on the order of μm 's) as frequency increases, and that the resonator stiffness remain large to allow the device to handle larger input powers and suppress nonlinear phenomena, as measured by IIP_3 [17]. Although it won't be described in detail here, the first measurements of IIP_3 for micromechanical

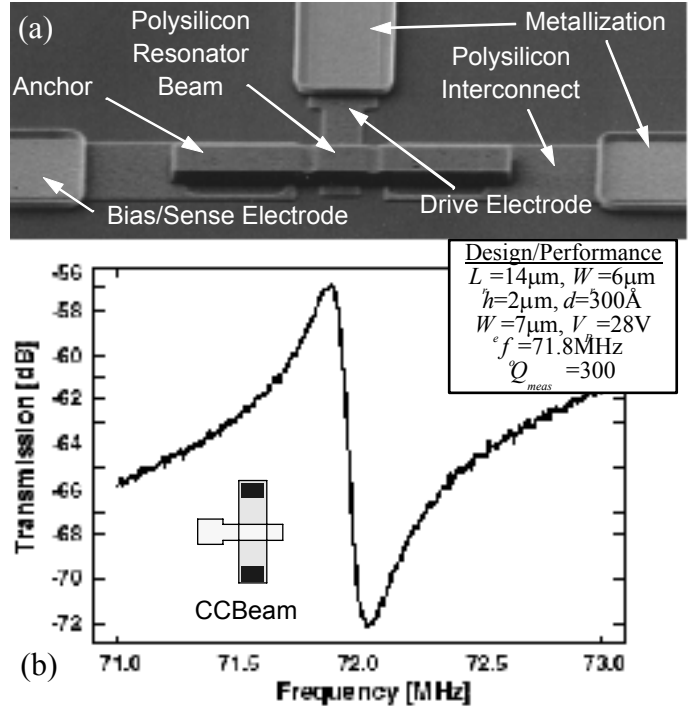


Fig. 8: (a) SEM of a 70 MHz clamped-clamped beam μm mechanical resonator. (b) Measured frequency characteristic for the resonator of (a).

requirements, let alone military requirements, which are many times more demanding. Thus, especially for wireless applications in hostile military environments, it would be much preferred if the width and thickness dimensions of a flexural beam resonator could remain sizable (on the order of μm 's) as frequency increases, and that the resonator stiffness remain large to allow the device to handle larger input powers and suppress nonlinear phenomena, as measured by IIP_3 [17]. Although it won't be described in detail here, the first measurements of IIP_3 for micromechanical

resonators were made under this grant, and these measurements, along with analytical formulations predicting IIP_3 , concluded that micromechanical resonator stiffness should remain large if adequate IIP_3 and power handling performance are to be maintained for both military and commercial communications applications [17].

4.1.3. Free-Free Beam Micromechanical Resonators

Pursuant to allowing high resonator stiffness, high frequency, and high Q simultaneously in micromechanical resonators, a free-free beam resonator design that effectively eliminates anchor dissipation in micromechanical resonators was next investigated under this grant. The SEM for a 71MHz version of this free-free beam resonator is presented in Fig. 9, which also identifies important features and dimensions [18]. As shown, this device is comprised of a free-free μ mechanical beam supported at its flexural node points by four torsional beams, each of which is anchored to the substrate by rigid contact anchors. An electrode is provided underneath the free-free beam to allow electrostatic excitation via an applied ac voltage v_i , and output currents are detected directly off the dc-biased (via V_p) resonator structure.

The torsional support beams for this device are strategically designed with quarter-wavelength dimensions, so as to affect an impedance transformation that isolates the free-free beam from the rigid anchors. Ideally, the free-free beam sees zero-impedance into its supports, and thus, effectively operates as if levitated without any supports. As a result, anchor dissipation mechanisms normally found in previous clamped-clamped beam resonators are greatly suppressed, allowing much higher device Q , even when the stiffness of resonant beam is extremely large.

Figure 10 compares the measured frequency characteristics for free-free beam resonators at 31.51 MHz and 92.25 MHz, respectively, showing Q 's right around 8,000 for both resonators—much higher than their clamped-clamped beam counterparts. Note that the fact that Q remains constant with increasing frequency for these an-

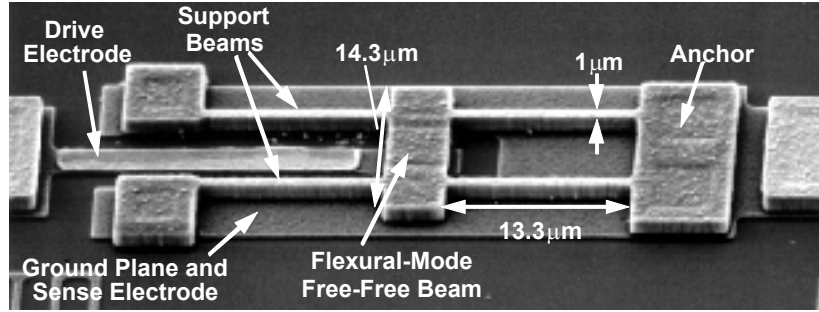


Fig. 9: SEM of a 71MHz free-free beam micromechanical resonator.

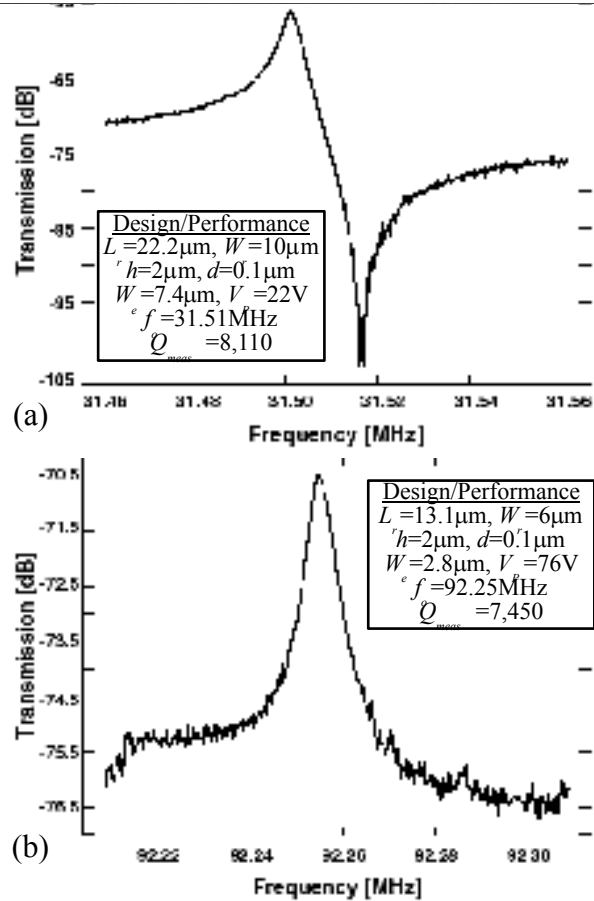


Fig. 10: Measured spectra for (a) a 31.51MHz free-free beam μ resonator; and (b) a 92.25 MHz free-free beam μ resonator.

chor-isolated free-free beam resonators verifies that anchor losses are a dominant mechanism for Q -degradation in the clamped-clamped beams of Fig. 8. Needless to say, these results are very exciting, as it represents one of the keys to achieving operation frequencies in the UHF range. In addition, the 92 MHz frequencies demonstrated now satisfy the frequency range needed for IF filters in the majority of commercial wireless phone handsets, and satisfy the RF range for SINCGARS (30-88MHz) wireless systems used in the military (e.g., on UAV's).

To attain further increases in frequency, one need only continue to reduce the length of the flexural mode beam. For example, a $4.38\text{ }\mu\text{m}$ -long, $2\text{ }\mu\text{m}$ -thick, $4\text{ }\mu\text{m}$ -wide polysilicon beam would achieve a frequency of 780 MHz when operating in its second flexural mode. Using fine-line lithography, such as used for today's transistors, appropriately-sized supports and more accurate support beam attachment locations should be feasible to allow the implementation of such small devices at UHF frequencies. However, again due to power handling limitations and also due to "scaling-induced" performance limitations (e.g, mass loading noise, temperature fluctuation noise, both of which degrade oscillator phase noise [19]), if it can be avoided, it is best not to use tiny dimensions when extending frequencies.

4.1.4. Radial Contour-Mode Micromechanical Disk Resonators

With the intent of attaining UHF frequencies without the need for too much scaling, resonator research under this grant turned its focus away from flexural-mode resonators to seek out alternative vibration modes that would allow high frequency, while retaining relatively large geometric dimensions. The result: A micromechanical, laterally vibrating disk resonator, shown in Fig. 11, fabricated via a technology that combines polysilicon surface-micromachining and metal electroplating to attain sub-micron lateral capacitive gaps, and demonstrated at frequencies approaching 160 MHz with Q 's as high as 9,400—the highest demonstrated Q to date for an on-chip resonator in this frequency range [20]. This frequency also represents the highest to date for an *electrostatically transduced* micromechanical resonator and is an important step towards reaching the frequencies required by the RF front-ends in wireless transceivers. Unlike previous micromechanical resonators that employ flexural mode beams to achieve mid-VHF frequencies [18], this resonator utilizes the radial contour mode, or areal dilation of a disk, in which the disk expands and contracts along its radius. The geometric dimensions necessary to reach a given frequency are larger for this contour-mode than for the

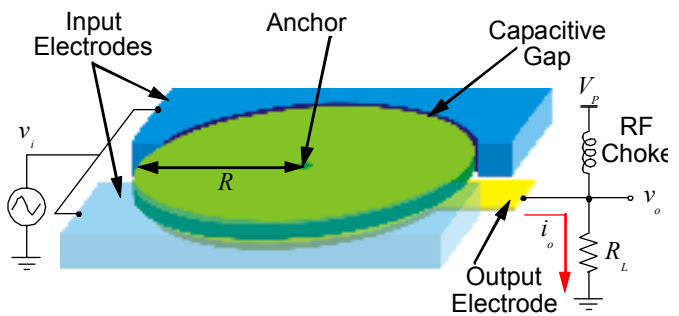


Fig. 11: Schematic of a contour -mode disk resonator with the preferred bias and excitation scheme.

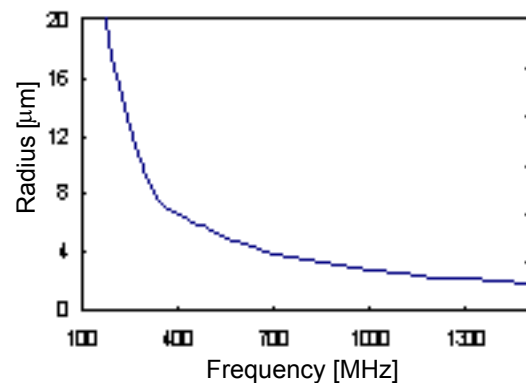


Fig. 12: Predicted resonant frequency versus the radius of a radial contour mode disk fabricated in polysilicon.

flexural-modes used by previous resonators [18], making disk resonators not only geometrically more suitable for UHF frequencies, but also less susceptible to the “scaling-induced” performance limitations described above. This, coupled with the observation that larger size leads to higher power handling ability and higher dynamic range [13], and coupled with its unprecedented Q value, makes this disk resonator a choice candidate for use in the IF and RF stages of future miniaturized transceivers.

The resonant frequency of this contour-mode disk resonator is determined by its structural material properties and is inversely proportional to its radius. A simplified expression for resonance frequency can be written as

$$f_o = \frac{\alpha}{R} \sqrt{\frac{E}{\rho}} \quad (4)$$

where α is a constant dependent on the Poisson's Ratio of the material (0.342 for polysilicon), E is the Young's Modulus of the material, ρ is its density, and R is the radius of the disk. The plot in Fig. 12 shows the predicted resonant frequency as a function of radius, assuming polysilicon as a structural material. As shown, disk resonators are quite capable of extending into the GHz range while maintaining very reasonable dimensions. (Note that the dimensions in polydiamond [21] will be even larger.)

Figure 13 presents the SEM of a fabricated 156 MHz disk with 1000Å electrode-to-resonator gaps. Figure 14 presents the measured frequency spectrum for this resonator, showing a Q of 9,400—again, the highest demonstrated to date for an on-chip resonator in this frequency range.

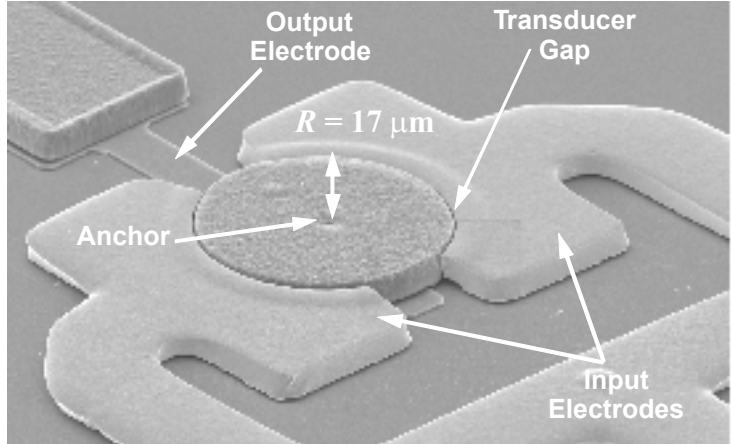


Fig. 13: (a) SEM of a fabricated 156 MHz contour-mode disk μ mechanical resonator.

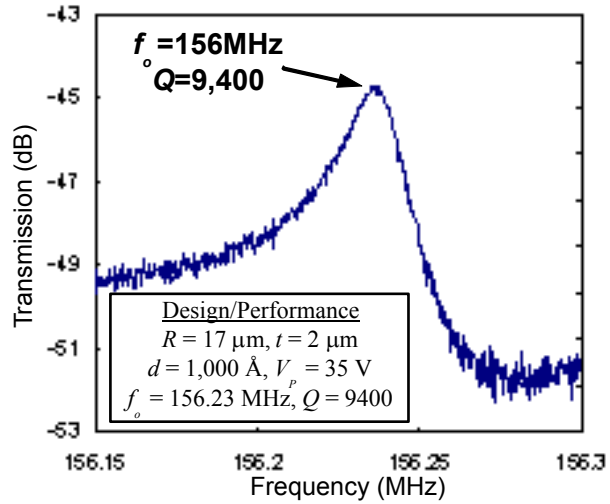


Fig. 14: Measured frequency characteristic for the contour-mode disk μ mechanical resonator of Fig. 13.

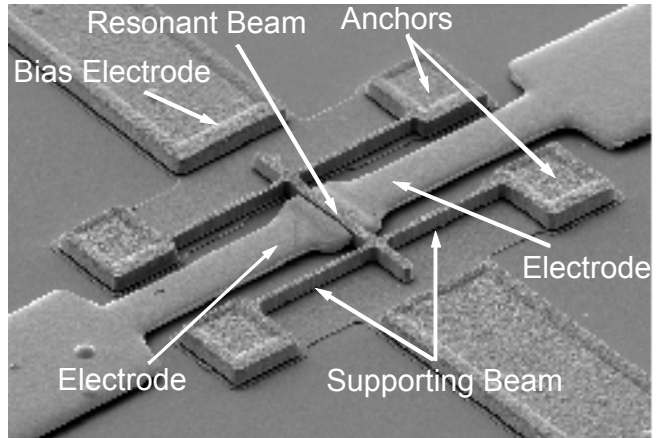


Fig. 15: SEM of a 10.47 MHz lateral free-free beam polysilicon μ mechanical resonator with metal electrodes and 1000Å lateral electrode-to-resonator gaps.

In order to minimize the input impedance of this device, high aspect-ratio, sub-micron lateral gap spacings are required between the electrode and disk perimeter. These are achieved using a process that combines surface micromachining, metal-electroplating, and a sidewall sacrificial-spacer technique, to attain lateral polysilicon resonators with metal electrodes and submicron lateral electrode-to-resonator gaps without the need for aggressive lithography and etching [23]. Resonators with these qualities are clearly a major improvement over previous resonators (made in either nickel or polysilicon), since they allow the best of both worlds from a resonator standpoint: metal electrodes for low resistance interconnect (and thus, minimal Q -loading); and polysilicon (or polydiamond) structural materials, which to date have allowed much higher Q than nickel resonators. In addition, lateral resonators in general, whether disks or flexural mode, have advantages over vertical counterparts in that they (1) do not require underlying electrodes, so alleviate frequency uncertainties due to topography that sometimes plague vertical-mode resonators; (2) allow higher Q for CC-beam resonators, since they reduce substrate losses by moving parallel to substrate, rather than directly into it; and (3) provide more geometric flexibility, allowing for more general mechanical circuit topologies and for more transducer electrodes (e.g., for balanced operation). Figure 15 presents the SEM of a lateral FF-beam resonator supported at its nodal locations by second-mode flexural supports that takes full advantage of the above design flexibilities to achieve a Q of over 10,743 at 10.48 MHz [24].

With reference to Fig. 16, the process begins with steps similar to those used in surface micromachining to achieve a $2\mu\text{m}$ -thick polysilicon structure supported by an underlying sacrificial oxide layer. A thin film of oxide is then conformally deposited along the sidewalls of the polysilicon structure to define the eventual electrode-to-structure capacitive gap spacing (c.f., Fig. 16(a)). Next, the bottom sacrificial oxide is patterned and etched to expose the underlying

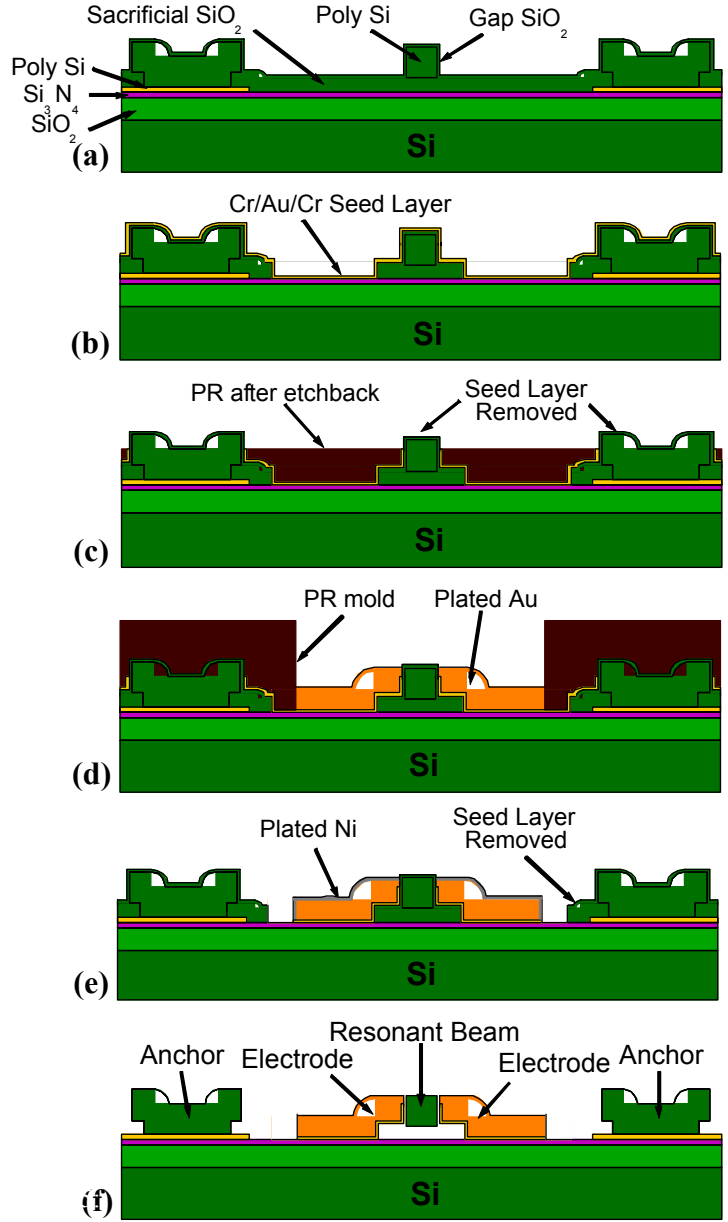


Fig. 16: Process flow for the multiple-metal-electrode, sub-micron gap, polysilicon lateral resonator technology.

nitride film in areas where metal electrodes are to be formed. In preparation for metal electroplating, a thin Cr/Au/Cr seed layer is evaporated over all areas (c.f., Fig. 16(b)), followed by an photoresist-assisted etch back procedure that removes the seed layer over the tops of the polysilicon structures to prevent metal from plating over them (c.f., Fig. 16(c)). A thick photoresist layer is then patterned to form a mold that, together with the sidewall sacrificial oxide, defines the eventual Au-plated electrodes. After removing the top layer of Cr to expose the Au seed layer (using the mold as a mask), Au is electroplated to form the electrodes and achieve the cross-section of Fig. 16(d). The photoresist mold is then removed, and a thin layer of Ni is plated over exposed Au electrode regions (with Cr blocking any plating in field regions) to protect them during a subsequent seed layer removal step (c.f., Fig. 16(e)). Structures are then released in HF to yield the final cross-section shown in Fig. 16(f).

From a frequency extension perspective, with its balanced symmetry (for higher Q), coupling flexibility (for an assortment of filter and mechanical circuit topologies), and higher power handling ability, the contour-mode disk resonator of Fig. 13 constructed via the process of Fig. 16 represents one of the best geometries available for future micromechanical signal processors at ultra-high frequency (UHF; 300 MHz - 3 GHz) and beyond. And it appears that silicon or polysilicon structural material will suffice for UHF frequency applications.

4.1.5. CVD Polydiamond Micromechanical Resonators

However, pursuant to attaining UHF and even higher frequencies with greater ease, the efforts of this grant soon moved towards other materials that possess higher acoustic velocities. Of the available materials, diamond was identified as one of the best candidates, since (1) its acoustic velocity was the highest among other candidates (including SiC); (2) diamond is well known as an inert, extremely stable material, very appropriate for communication reference applications; and (3) diamond can be deposited in polycrystalline form via a CVD process, and thus, is amenable to convenient MEMS fabrication techniques, like surface-micromachining.

Of the above advantages, the acoustic velocity of course is most relevant to attaining higher frequency. More specifically, since the resonance frequency of a mechanical resonator is generally directly proportional to the acoustic velocity of its structural material, polydiamond has great potential

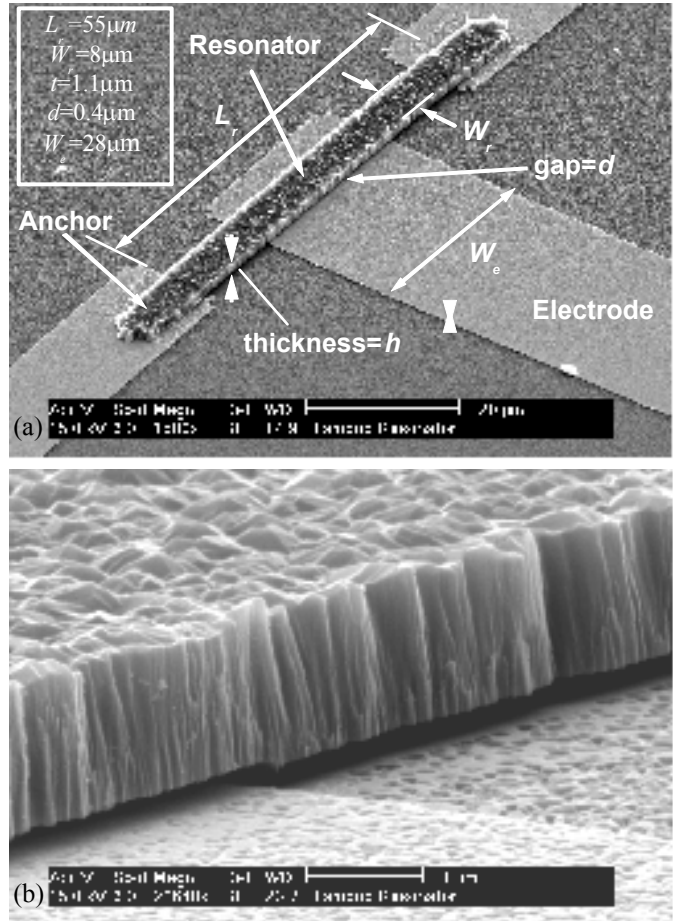


Fig. 17: (a) Wide-view and (b) zoom-in SEM's of a 3MHz CVD polydiamond CC-beam μ mechanical resonator with metal electrodes, all fabricated via the process of Fig. 18.

for more easily achieving the coveted UHF frequencies (0.3-3GHz) required for use in present and future wireless communication transceivers.

From a resonator stability perspective, due to the inert nature and inherent stability of diamond material, for which very little diffusion can occur even at high temperatures [25], diamond can potentially offer better aging characteristics than polysilicon, which is extremely important for communication frequency reference applications.

With the above as incentives, the researchers of this grant teamed up with Jim Butler and his research group at the Naval Research Laboratory to explore CVD polycrystalline diamond material as a structural material for high frequency micromechanical resonators. This investigation involved the fabrication and testing of various resonators previously achieved in polysilicon technology, but using CVD polydiamond as the structural material, provided by the Naval Research Laboratory. Both clamped-clamped beam and folded-beam, comb-driven micromechanical resonator designs were used, the former to allow HF frequency evaluation, the latter to facilitate measurement of the intrinsic Q of the polydiamond material. In particular, lower frequency, highly-compliant, folded-beam designs suffer less from anchor dissipation, so are more suited to determining the intrinsic Q of the structural material under vacuum.

Figure 17 presents scanning electron micrographs (SEMs) of a 3 MHz CVD polydiamond CC-beam micromechanical resonator fabricated via the surface micromachining process outlined in Fig. 18 [21]. If its length is much longer than its width or thickness, an expression for resonance frequency of a CC-beam can be written as [15]

$$f_o = 1.03K \sqrt{\frac{E}{\rho}} \frac{h}{L_r^2} [1 - g(d, V_p)]^{1/2} \quad (5)$$

which clearly depends on both beam dimensions (specified in Fig. 17) and structural material properties, specifically the Young's modulus E and the density ρ , both of which define the acoustic velocity, $\sqrt{E/\rho}$. In (5), κ is a frequency modification factor that accounts for beam topography [15], and the function g accounts for the effect of electrical stiffness [15].

The process flow of Fig. 18 differs from conventional polysilicon surface micromachining processes [15] in three key ways: (1) Cr/Au metal is used as the interconnect material rather than polysilicon, to lower interconnect losses for high frequency applications; (2) PECVD oxide is used as the sacrificial layer, which simplifies the release of sub-micron electrode-to-resonator gaps; and (3) low temperature CVD polydiamond is used

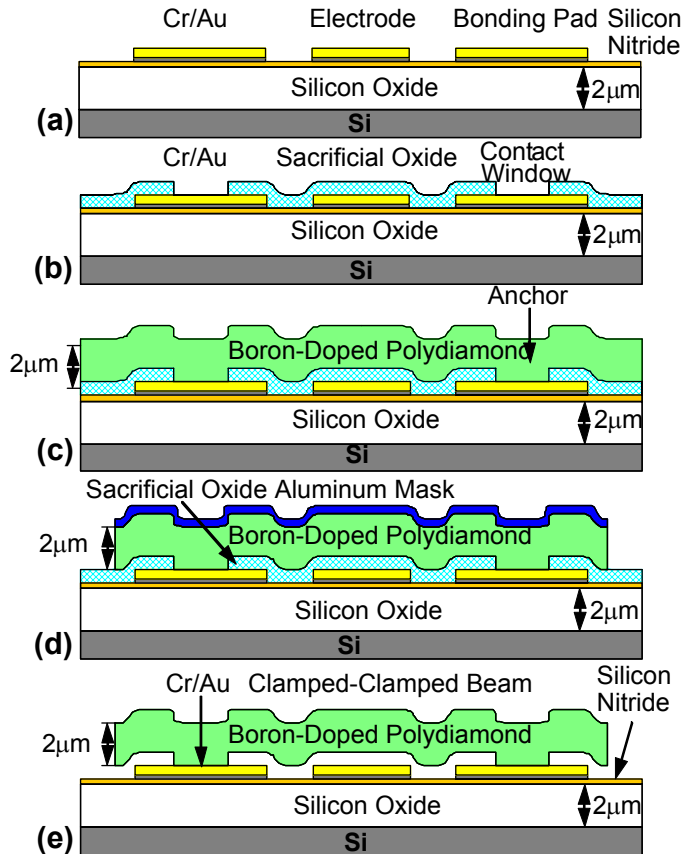


Fig. 18: Fabrication process flow for the polycrystalline diamond CC-beam resonator with metal electrodes.

as the structural material, with advantages as described above.

Among the various steps in any CVD polydiamond process, the formation of a diamond nucleation layer is perhaps the most important, since the size and density of nucleation particles has the greatest impact on the eventual size and coverage of diamond grains, hence, on the surface roughness of polydiamond films. Given the impact of surface roughness on the Q of previous high frequency polysilicon micromechanical resonators [13], smooth films are preferred.

For this work, a nucleation layer was established by (1) first pretreating the substrate to the diamond growth plasma conditions for a brief period of time, typically 10 to 30 minutes; then (2) putting the treated substrate into an ultrasonic bath of ultra disperse nanocrystalline diamond powder [22] in methanol for 10 to 60 minutes; followed by (3) immediate rinsing and washing with ethanol and nitrogen blow dry. Finally, the seeded substrate is returned to the growth reactor and doped diamond is grown to the desired thickness. Doping was achieved by the addition of dilute amounts of diborane to the reactants. The growth rate and film thickness was monitored *in situ* by diode laser reflectometry at 670 nm. Uniform and conformal nucleation densities in excess of 10^{11} cm^{-2} have been observed over a variety of dissimilar materials with this technique, enabling the fabrication of continuous films with thicknesses as little as 80 to 100 nm on Si or SiO_2 .

Polydiamond can be deposited and *in situ* doped with boron via a microwave PECVD process using as reactants 0.33% CH_4 and $6.7 \times 10^{-5}\%$ B_2H_6 in a flow of 900sccm of H_2 at 15Torr, excited by 800W of 2.45GHz microwaves, with a substrate temperature between 500 and 600°C. The material of this work was deposited at 540°C, which is low enough to allow the use of highly conductive metal electrodes for lower loss and higher power handling at GHz frequencies. Once deposited, the polydiamond is easily machinable via RIE, using an O_2/CF_4 chemistry that does not attack the underlying oxide at an excessive rate (making it amenable to fabrication via surface micromachining. Figure 17(b) presents a zoomed SEM shot of a fabricated polydiamond beam, showing grains on the order of 300nm and a surface roughness of about 100 nm for a 1.1 μm thick film. To etch the diamond material, an RIE recipe using O_2 and CF_4 at 50mTorr with a power of 250W was used, with an etch rate about 2 $\mu\text{m}/\text{h}$, and with very good results, as shown in the SEM of Fig. 17(b).

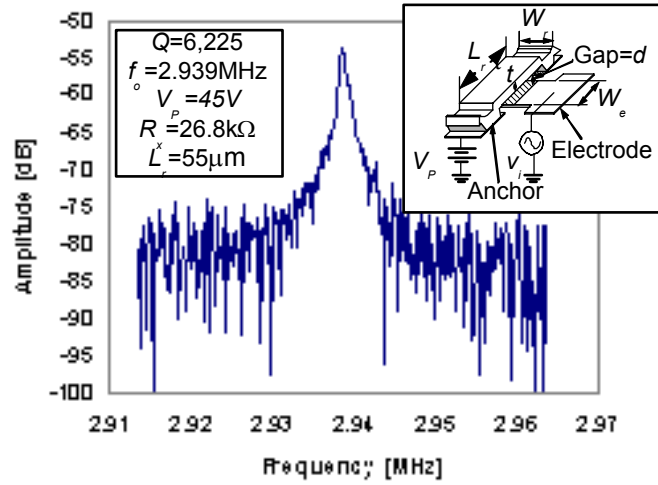


Fig. 19: Frequency characteristic for a 2.94MHz CVD poly diamond CC-beam resonator.

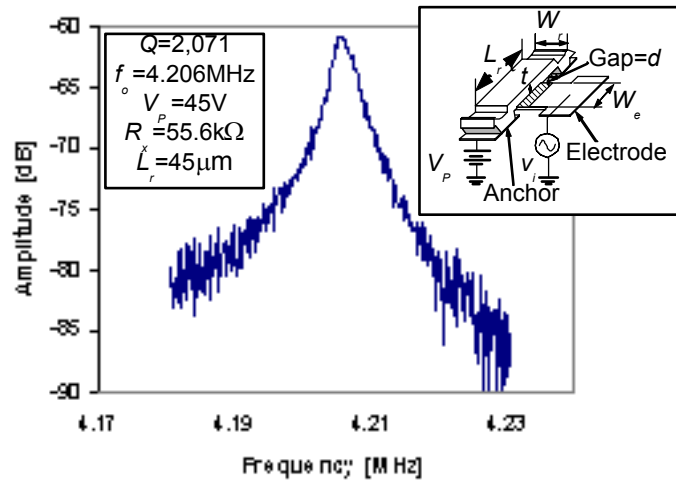


Fig. 20: Frequency characteristic for a 4.21MHz CVD poly diamond CC-beam resonator.

CC-beams were designed and fabricated with varying lengths with the intention of generating a plot of frequency versus beam length, from which Young's modulus can be more accurately extracted by curve fitting. Figures 19 and 20 present the frequency characteristics for 2.94 and 4.21MHz CC-beams, respectively, measured under 50 μ Torr pressure, showing Q 's of $\sim 6,000$ and $\sim 2,000$, both of which are comparable to values seen in polysilicon versions at similar frequencies. Figure 21 presents the desired plot of frequency versus beam length, from which a curve fit of Eq. (5) (shown) using the crystalline diamond density of 3,500kg/m³, yields a Young's modulus of 304GPa and an acoustic velocity of 9,320m/s. Although this value of acoustic velocity is larger than the 8,076m/s of polysilicon (by 15%), it is still not as large as potentially achievable, since *single-crystal* diamond has an acoustic velocity more than twice that of polysilicon.

To remedy this, a second run was done in which a higher nucleation density was achieved to create smoother films. Figure 22 presents the SEM of a folded-beam, comb-driven micromechanical resonator fabricated via this second run.

Upon testing, the CVD diamond folded-beam resonators of this particular run were found to be more resilient against moisture-induced stiction than previous polysilicon versions, and supercritical CO₂ drying was not necessary to obtain free-standing structures; i.e., no devices were stuck after a simple hot-plate-assisted air drying step. Figure 23 presents the measured frequency characteristic for the resonator of Fig. 22, showing a resonance frequency of 38.8 kHz and a Q of 19,500, which almost as good as values seen in identical polysilicon μ mechanical resonators. In addition, the measured frequency of 38.8 kHz is more than 80% higher than measured in equivalent polysilicon versions of this resonator, indicating that the Young's modulus for this run is 985 GPa, which is close to the expected value for single-crystal diamond! Needless to say, this

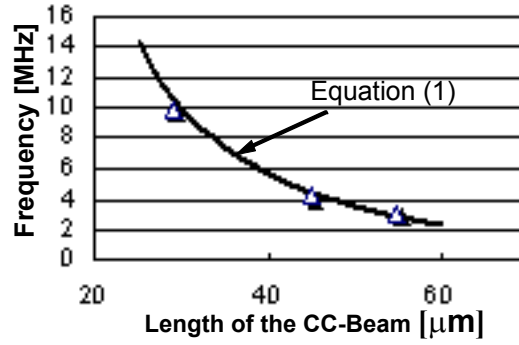


Fig. 21: Plot of frequency versus beam length for the CVD diamond resonators of this work. (The points are measured data; the curve is the theoretical prediction of Eq. (5).)

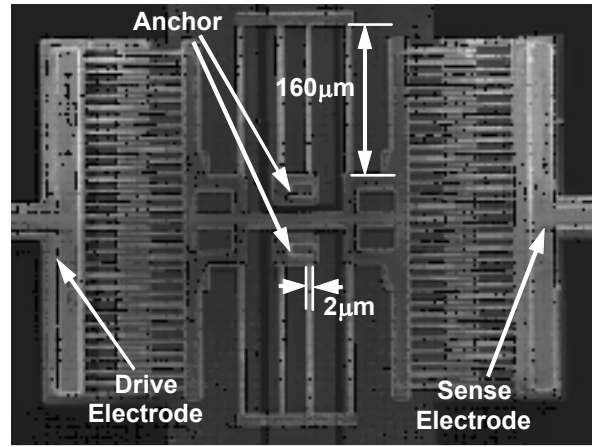


Fig. 22: SEM of a 38.8 kHz CVD polydiamond folded-beam, comb-driven μ mechanical resonator

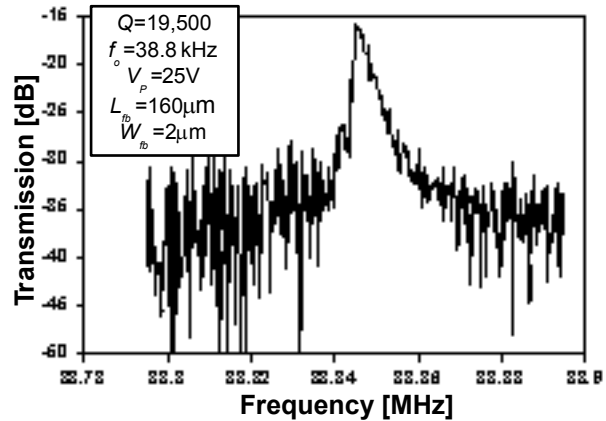


Fig. 23: Frequency characteristic for a 38.8 kHz CVD polydiamond folded-beam μ mechanical resonator.

result establishes polydiamond as an excellent material candidate for use in high- Q UHF filter and oscillator applications for communications, as well as other high- Q applications (e.g., gyroscopes, resonant sensors, etc.).

4.1.6. Technology Transfer

To transfer this technology to military-relevant users and laboratories, a number of fabrication runs were done with conservative, more robustly designed polysilicon CC-beam devices operating at 5, 10, and 20 MHz. These devices were then delivered to Raytheon TI Systems for vacuum packaging, using a technology they developed under the DARPA/MTO MEMS Program. After vacuum packaging into DIP packages, dies were sent back to the University of Michigan for final evaluations, then sent out to various military labs and industry users, including AFRL/ITI, CECOM, and the MAYO Foundation. Raytheon TI Systems also retained a good number of resonators for their own evaluations. At the time of this writing, Tim Schaeffer at the MAYO Foundation has reported that the resonators received have worked in their particular system. (Contact Tim Schaeffer for more information, as his application is classified, so he cannot tell me exactly what it is.)

4.2. Micromechanical Resonator Oscillator Design and Demonstration

While micromechanical resonators were being demonstrated with increasing frequencies, practical communication circuits that utilized the earlier resonator designs were also being explored. Of the many blocks in a communication transceiver that can benefit from MEMS implementation, the highly-stable, low phase noise, reference oscillator was the most straightforward to attack first, since its operation frequency is on the order of 10-20 MHz, which was in range early in the course of this grant. As a result, this grant pursued a reference oscillator as the first MEMS/ transistor system demonstration.

Among the oscillators achieved early in this grant were lower frequency prototypes using folded-beam micromechanical resonators, constructed in both polysilicon material [26] and nickel material [27]. (As will be detailed in Section 4.2.4, nickel was investigated as a vibrating micromechanical resonator material due to the ease with which it could be integrated together with transistor circuits.) Although these lower frequency oscillators proved helpful in predicting some of the issues that would need solving for higher frequency versions, they will not be detailed in this final report, as they have already been described in previous reports, and in the interest of maintaining a reasonable page count for this report.

4.2.1. A 10 MHz Micromechanical Resonator Pierce Oscillator

To attain an oscillator at a frequency more consistent with communication reference oscillators, a modified Pierce circuit topology was used to first demonstrate a ~ 10 MHz μ mechanical resonator reference oscillator, then to assess the ultimate frequency stability of such an oscillator via accurate measurement of its close-to-carrier phase noise [28].

Figure 24 presents the complete circuit schematic utilized to instigate and sustain oscillation. Although it maintains the phase noise advantages of the Pierce topology, this circuit differs substantially from the conventional Pierce, as it uses two transistors instead of one in order to compensate for the large series motional resistance R_x of the clamped-clamped beam (“CC-beam”) μ mechanical resonator used to set the oscillation frequency. The additional transistor is needed not for additional gain, but rather for buffering, to insure that the overall loop phase shift ($=180^\circ + \phi_1 + \phi_2 + \phi_3$) equals 0° (or 360°)—one of the fundamental conditions required for

Given the recent interest in “scaling-induced” physical noise mechanisms, such as adsorption-desorption noise (i.e., mass loading) or thermal fluctuation noise [19], that become more important as devices are scaled to achieve high frequencies, one might first suspect these noise sources as possible mechanisms. However, as shown in the predicted curves (using theory from [19]) for these noise mechanisms in Fig. 27, the dimensions of this 9.75 MHz resonator are large enough that the scaling-induced noise mechanisms should be insignificant even in comparison with noise predicted by Leeson’s equation, let alone the actual measured noise.

Closer inspection of Fig. 27 reveals that the slope of the phase noise curve at small frequency offsets is in fact not the $1/f^2$ predicted by Leeson’s equation or by scaling-induced noise theories, but rather $1/f^3$, and it is this $1/f^3$ component that significantly degrades the short-term stability of this oscillator, limiting the phase noise to -80 dBc at a 1 kHz offset from the carrier. Although investigations into this are ongoing, initial analyses suggest the following possible mechanisms for this $1/f^3$ phase noise component:

- (1) Non-linearity in the resonator capacitive transducer aliases $1/f$ electronic noise (e.g., from the sustaining amplifier) onto the carrier frequency, generating a $1/f^3$ component.
- (2) $1/f$ noise associated with the dc-bias V_P on the resonator structure modulates the electrical stiffness k_e of the resonator [15], inducing a $1/f^3$ phase noise component.
- (3) $1/f$ mechanical noise induces variations in the electrode-to-resonator gap spacing d_o , which then modulates the electrical stiffness k_e [15], generating a $1/f^3$ phase noise component.

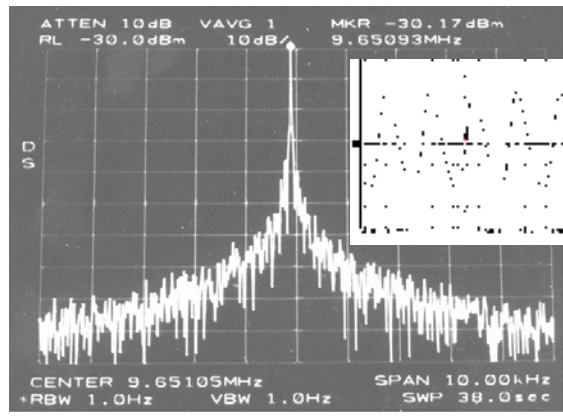


Fig. 25: Measured Fourier spectrum for the oscillator of Fig. 24, with an oscilloscope waveform in the inset.

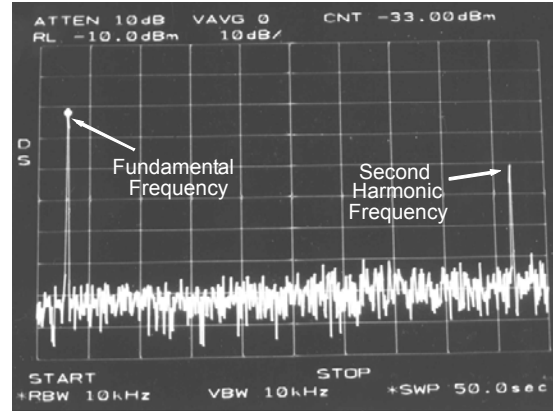


Fig. 26: Measured Fourier spectrum showing second harmonic oscillator output.

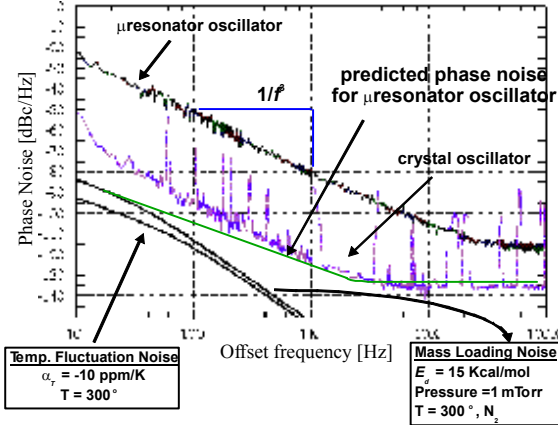


Fig. 27: Phase noise versus frequency of fset from the carrier for a 9.75 MHz CC-Beam Pierce oscillator and a 10 MHz crystal version. Theoretical phase noise plots for the CC-beam oscillator are also included.

Of the above, (1) is the most likely mechanism, since its expression for phase noise [28]

$$L\{f_m\} = \frac{1}{4Q_l^2} \left[\frac{1}{4V_P^2} + \frac{Q_l^2}{k_{\text{eff}}^2} \frac{(\epsilon_o A_o)^2 V_P^2}{d_o^6} \right] \cdot 2qK_1 I_B R_s^2 \cdot \frac{f_o^2}{f_m^3} \quad (6)$$

most closely matches the measured data. In (6), K_1 is the flicker noise coefficient for a bipolar transistor, I_B is its base current, and R_s is the transresistance gain of the sustaining amplifier. Assuming a $1/f$ noise corner of 5 MHz, $I_B=0.5$ mA, and $R_s=14$ k Ω , (6) gives -81 dBc/Hz @ 1 kHz for the oscillator of Fig. 24. This value agrees very well with the data of Fig. 27, and thus, lends confidence that mechanism (1) is most responsible for $1/f^3$ phase noise. This is rather fortunate, since it implies that the $1/f^3$ phase noise component can be reduced by minimizing the $1/f$ noise of the sustaining amplifier—something that can easily be done by improving the $1/f$ noise performance of the input transistor in the sustaining amplifier. Work to remove this $1/f^3$ phase noise component is presently underway by this PI under the DARPA/MTO NMASP Program.

4.2.2. Temperature Compensation

In addition to short-term stability, reference oscillators (and virtually all other communication components, including the filters to be discussed in Section 4.3) must also satisfy stringent long-term stability specifications. Of the various physical phenomena that generate long-term frequency instabilities, temperature changes are among the most important. At the start of this grant, temperature stability was perhaps the performance category where micromechanical resonators were most lacking when compared with quartz crystals. In particular, at the start of this grant the total frequency excursion of a typical clamped-clamped beam polysilicon micromechanical resonator over the military temperature range was almost 70X worse than that of the best AT-cut quartz crystal.

Pursuant to closing the gap between micromechanical resonators and quartz, two techniques were developed under this grant to compensate for the temperature dependence of micromechanical resonators. The first, dubbed “geometric-stress compensation”, utilizes strategic geometric design to realize a temperature-dependent mechanical stiffness that counteracts frequency changes due to Young’s modulus temperature dependences [30]. Figure 28 presents the perspective-view schematic of a geometric-stress temperature-compensated resonator, indicating key components and specifying a preferred excitation and measurement configuration. As shown, this structure consists of a beam that is clamped to the substrate at one end, but supported at the other by a folded struc-

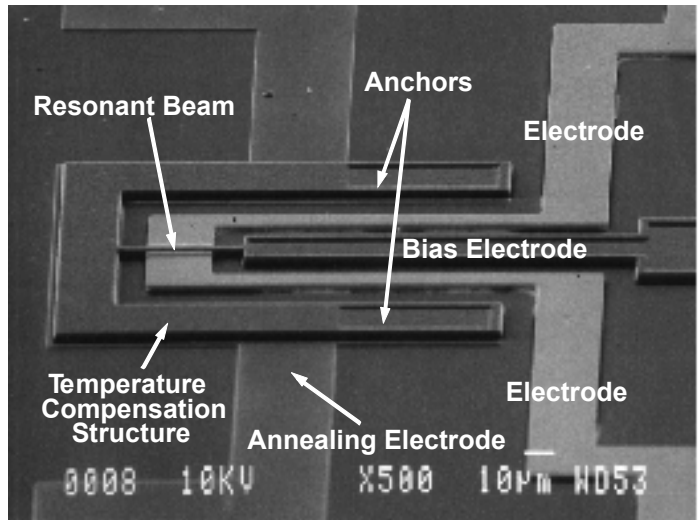


Fig. 29: SEM of a 13.5 MHz mechanically temperature-compensated resonator: (a) Perspective view. (b) Close-up view around the electrodes.

ture comprised of a truss section attached to two outer beams. Metal electrodes are positioned on either side of the resonator beam to allow lateral (i.e., x-directed) excitation using the voltage configuration shown. To insure that only the resonator beam vibrates when excitation signals are applied, the outer support beams are made much wider than the resonator beam, making them rigid against lateral motions. The outer beams are also designed to be longer than the resonator beam, so they will expand faster than it with increasing temperature, generating a net tension in the resonator beam. This tensile stress serves to increase the beam's resonance frequency, and thus, oppose frequency decreases caused by Young's modulus temperature dependence, resulting in a smaller overall resonance frequency excursion over a given temperature range.

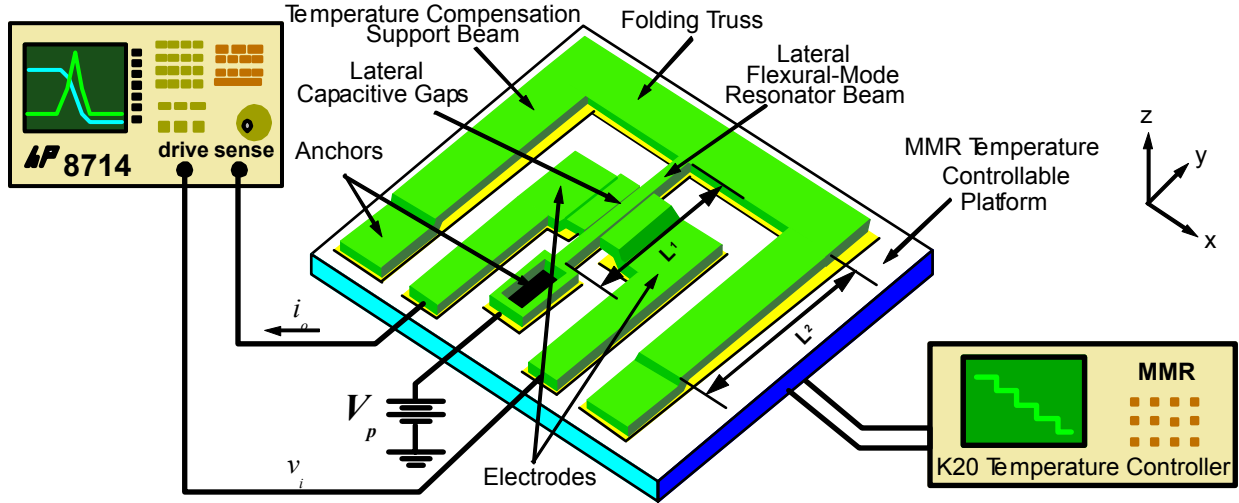


Fig. 28: Perspective-view schematic of a mechanically temperature-compensated micromechanical resonator and test set-up.

Figure 29 presents the SEM for a 13.5 MHz version of this temperature-insensitive resonator design fabricated via the sub-micron lateral gap process technology summarized in Fig. 16. Figure 30 presents a plot of fractional frequency change versus temperature for the resonator of Fig. 29 with varying L_1/L_2 beam ratios (see Fig. 28). From this plot, control of the resonance frequency temperature dependence can clearly be seen. In particular, for L_2/L_1 beam ratios from 30/40 to 60/40, the temperature coefficient decreases from $-35.9 \text{ ppm}/^\circ\text{C}$ for the $L_2/L_1=30\mu\text{m}/40\mu\text{m}$ device to $-2.5 \text{ ppm}/^\circ\text{C}$ for the $L_2/L_1=60\mu\text{m}/40\mu\text{m}$ device. Unfortunately, however, for higher beam ratios, the temperature coefficient is seen to degrade. This can be explained via a mechanism where the support beams bend upwards or downwards when the stress in the beams becomes too large in devices with large L_2/L_1 beam ratios,

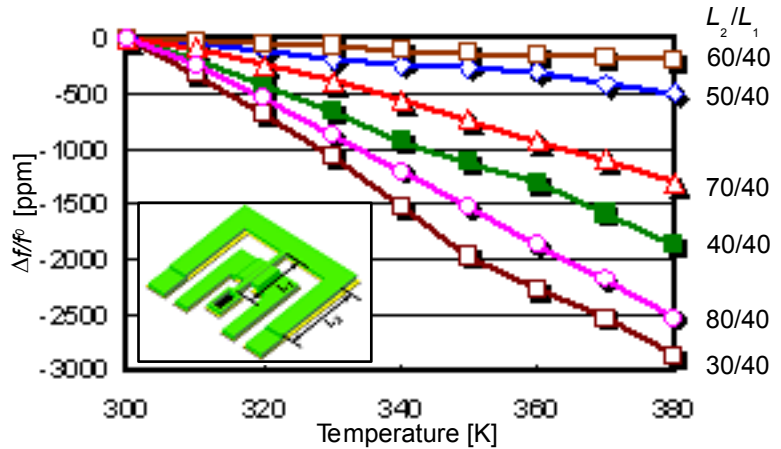


Fig. 30: Plots of fractional frequency change versus temperature for temperature compensated micromechanical resonators with various L_1/L_2 compensation ratios.

thereby suppressing and eventually reversing tensile stresses. Such a mechanism has been verified via finite element analysis, and this second order effect remains a limitation of the geometric-stress compensation technique.

In addition to the described support beam bending problem, the geometric-stress compensation method may also suffer from long-term stress-relaxation effects that allow the temperature dependence to change with time. Beyond this, the need to include geometric-stress inducing support beams that slightly influence the resonance frequency of the primary resonator beam also complicates the overall resonator design. This can be especially troublesome if the resonator were to be used in a micromechanical filter, for which the complexity of constituent resonators should be minimized to allow easy access to them via coupling beams.

In the effort to remedy the above deficiencies, the last six months of this grant have yielded a major breakthrough in micromechanical resonator thermal stability. In particular, polysilicon micromechanical resonators utilizing a novel *temperature-dependent electrical stiffness* design technique [31] to compensate for temperature-induced frequency shifts have been demonstrated with greatly reduced temperature coefficients (TC_f 's) on the order of -0.24 ppm/ $^{\circ}\text{C}$, which is 67 times smaller than exhibited by previous uncompensated resonators. With this new resonator design, the total frequency excursion over a 300K to 380K temperature range has been reduced from 1,280 ppm for an uncompensated device [18] to only 18 ppm, which for the first time, is now small enough to erase lingering concerns regarding the temperature stability of MEMS-based resonators targeted for communication applications. In addition to outright better performance, this technique offers numerous other advantages over previous compensation methods, including: (1) no dc power consumption; (2) voltage-control of the temperature coefficient; (3) ease of fabrication, which makes it flexible enough to use on a variety of different resonator designs; and (4) less susceptibility to stress relaxation (which is a potential problem for the geometric-stress compensation method discussed above [30]).

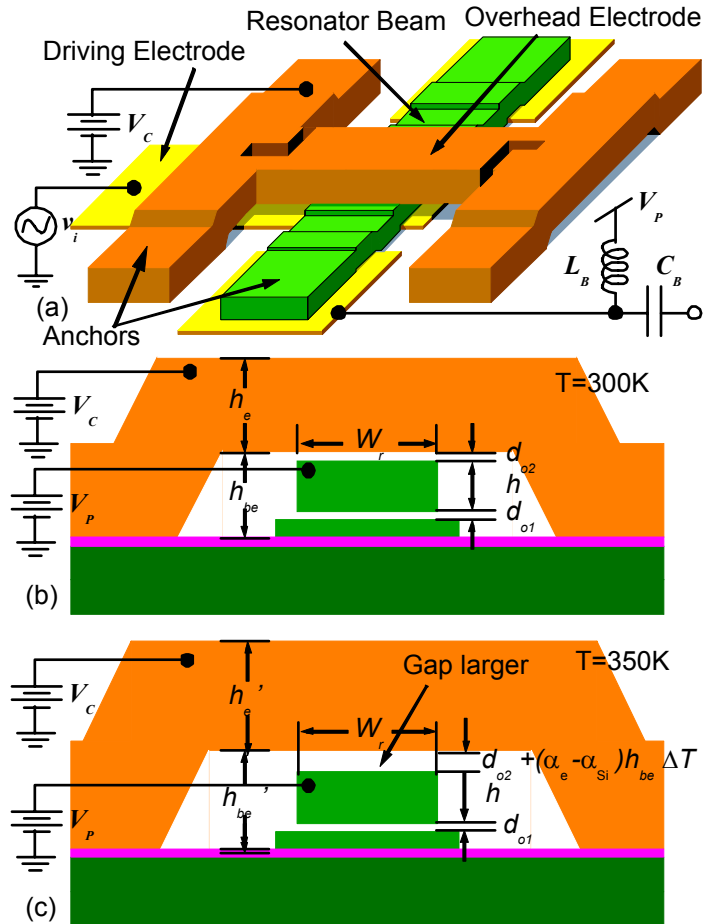


Fig. 31: (a) Perspective schematic of a stiffness-compensated micromechanical resonator, with effective cross-sections under different temperatures in (b) and (c).

Figure 31(a) presents the perspective-view schematic of an electrical stiffness-compensated temperature insensitive micromechanical resonator, indicating key components and specifying a preferred excitation configuration. As shown, this device consists of a polysilicon clamped-clamped beam (CC-beam) resonator, over which a metal electrode spaced 1000\AA above the beam has been added as the key instrument for temperature compensation. The anchoring structure for this top electrode includes slits to prevent compression induced bending of the electrode due to temperature increases. As shown in the effective cross-section of Fig. 1(b), the overhead electrode is supported by blocks constructed of a material that expands faster than the structural material of the mechanical resonator and its anchors. With this selection of materials, when the temperature is increased, expansions are such that the bottom side of the top electrode moves vertically upwards faster than the top of the resonator beam, resulting in a net increase in the top electrode-to-resonator gap spacing d_{o2} , as shown in the higher temperature cross-section of Fig. 1(c). This increase in the gap spacing then leads to a decrease in the top-electrode-to-resonator electrical spring constant and a corresponding increase in the resonance frequency, which then counteracts the decrease in frequency caused mainly by Young's modulus temperature dependence. Accounting for this mechanism, the expression for the temperature coefficient of the resonance frequency can be written as

$$TCf = (\alpha_{E_r} - \alpha_r) + \frac{3}{2} \frac{(V_P - V_C)^2 \epsilon_o A_{o2}}{d_{o2}^4 k_m} (\alpha_e - \alpha_r) h_{be}, \quad (7)$$

where α_{E_r} is the temperature coefficient of the Young's modulus, α_r and α_e are the thermal expansion coefficients of the resonator and electrode, respectively, k_m is the mechanical stiffness of the resonator (with no applied dc-bias V_P), m_r is the effective dynamic mass of the resonator, k_e is the electrical stiffness, V_P is the dc bias voltage, V_C is the dc control voltage on the top electrode, A_{o2} is the top electrode-to-resonator overlap area, ϵ_o is the permittivity in vacuum, and d_{o2} is the gap spacing between the top electrode and the resonator. As indicated in (7), the electrical stiffness generated across an electrode-to-resonator capacitive gap depends strongly on not only the gap spacing d_{o2} , but also on the voltage applied across the gap ($V_P - V_C$). Thus, by changing V_C , the total electrical stiffness as a function of temperature can be optimized to null the TC_f of the resonator beam—a distinct advantage over other compensation methods.

The process flow for constructing the overhead electrode involves a sequence of molded metal electroplating steps, and is

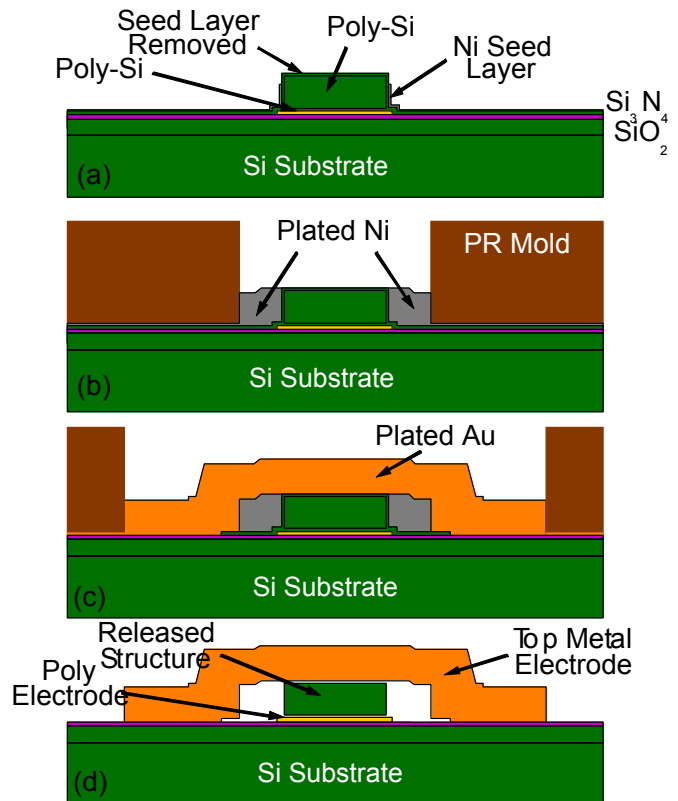


Fig. 32: Process flow cross-sections for top metal electrode formation. (a) After standard surface micromachining, deposit top sacrificial oxide and seed layer. (b) After molded electroplating of sacrificial Ni spacer. (c) After molded electroplating of Au top electrode. (d) After HF release.

summarized in Fig. 32. Figure 33 presents the SEM photograph of a fabricated device. Figure 34 presents a frequency characteristic measured under 50mTorr vacuum for the resonator of Fig. 33, showing a Q of 4,000, which is on par with previous CC-beams in this frequency range. Figure 35 presents a plot of fractional frequency change versus temperature for the resonator of Fig. 33 with varying values of applied dc-bias ($V_P - V_C$) across the top electrode-to-resonator gap. Clearly, the slope of the frequency versus temperature curve is adjustable via V_C . With $(V_P - V_C) = 8V$, the frequency versus temperature curve is flattest, achieving a $TC_f = -0.24 \text{ ppm}/^\circ\text{C}$ and yielding a total frequency excursion of only 17.8 ppm from 300K to 380K—the best to date

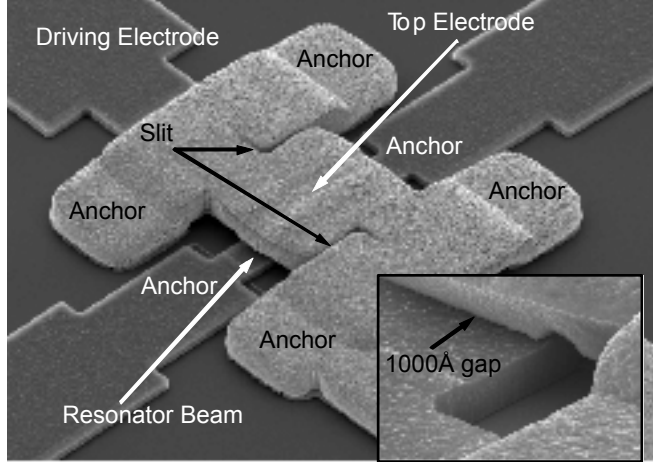


Fig. 33: SEM of a fabricated 10MHz stiffness-compensated temperature-insensitive micromechanical resonator, with an inset zoom in on the gap.

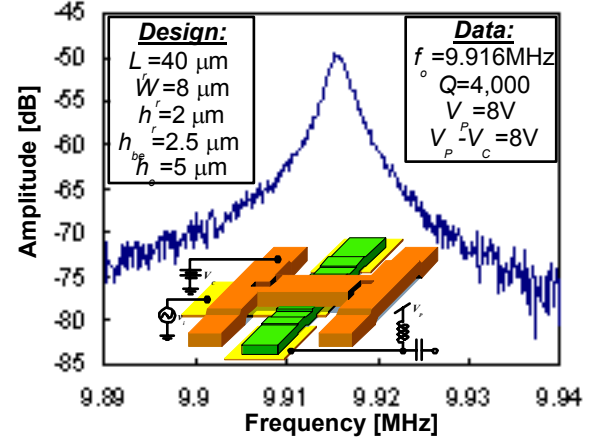


Fig. 34: Measured frequency characteristic for the 10MHz stiffness-compensated resonator of Fig. 33. (The inset shows the measurement setup.)

for any micromechanical resonator without assistance from active electronics.

Via the described stiffness-compensation design technique, the temperature stabilities of μ mechanical resonators have been reduced to levels rivaling that of the best AT-cut quartz crystals, and this constitutes a major step towards the use of these devices in stringent communications reference oscillator applications. Although the demonstrated performance is extremely encouraging, it should be mentioned that work towards establishing μ mechanical resonators as practical frequency references is still unfinished, since hysteresis in the temperature curves is yet untested, and sufficient aging and thermal stability must still be demonstrated under packaged environments. Work towards these ends must continue.

4.2.3. Localized Annealing for Frequency Trimming

Although a major success, the demonstration of a method to achieve adequate temperature stability is just one of many achievements needed before micromechanical resonator oscillators can begin to ser-

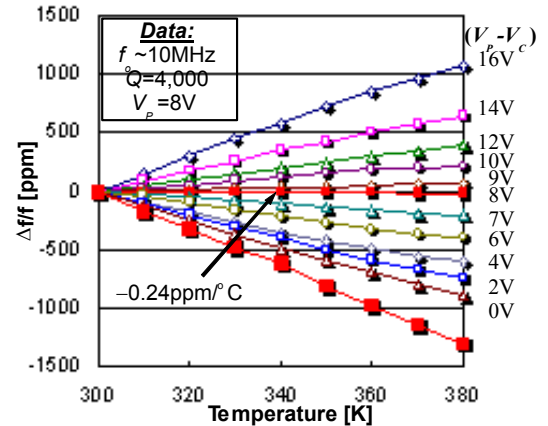


Fig. 35: Plot of fractional frequency change versus temperature for the 10MHz stiffness-compensated resonator of Fig. 33. Plotted as a function of the TC_f control voltage, $(V_P - V_C)$.

vice military and commercial wireless transceivers. Another extremely important capability instrumental to the economical manufacture such oscillators is the ability to trim micromechanical resonator frequencies to exact values. In particular, for the case of reference oscillators, the oscillation frequency must often be accurate to within 10 ppm of a desired value. Although the dc-bias applied to a capacitively-transduced micromechanical resonator can be used to tune its resonance frequency [15], a more permanent trim technique is often preferable, mainly to eliminate the need for a stable, controllable dc-bias in the oscillator circuit. In addition to oscillators, frequency trimming is also required for filters. For the case of filters, a permanent trim technique is again more desirable than mere dc-bias trimming, and even more so than for oscillators, since for filters many resonators must be trimmed, and dc-bias-based frequency tuning would require too many leads if numerous filters are needed.

To address this problem, an electrical-based frequency trimming technique was demonstrated, based upon filament-like heating or annealing of a micromechanical resonator, which alters the stress distribution in the structure, ultimately changing its frequency [32]. Figure 36 presents a schematic depicting details of this filament annealing procedure as applied to a properly biased and excited comb-driven, folded-beam μ mechanical resonator [4] with sense electronics. The resonator design is similar to predecessors [4] in all respects, except for the provision of distinct leads to both anchor points. During normal resonator operation, the pulse voltage generator v_{anneal} is inactive and provides the ground voltage for all components in this resonator system. In this configuration, the anchor leads along with the ground plane are tied to the dc-bias voltage V_p , and an ac signal is applied to one or more of the transducer electrodes to induce vibration. Once vibration is established, an output current is generated via the dc-biased, time-varying capacitor at the output electrode. This current is then sensed and amplified to a voltage by the transresistance amplifier.

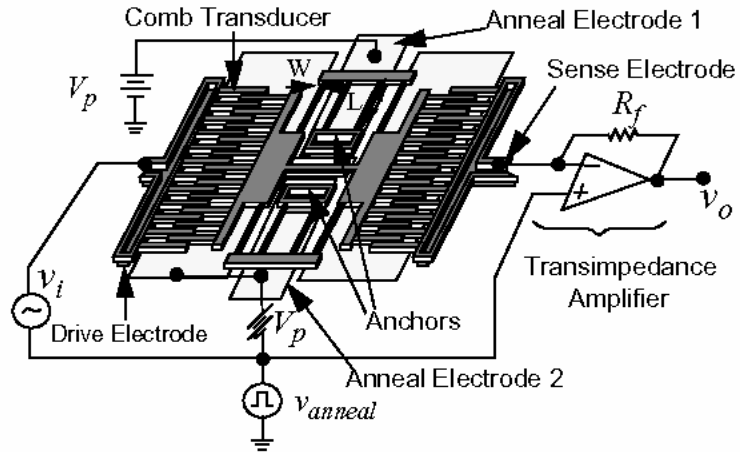


Fig. 36: Perspective-view schematic depicting details of the filament annealing procedure, showing circuit details and indicating key components.

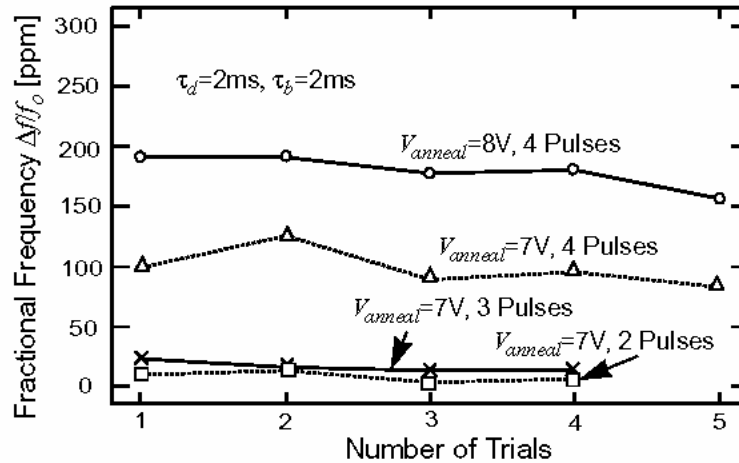


Fig. 37: Plot of frequency change versus anneal trial with the number of pulses as a third variable, indicating some consistency from trial to trial for a given resonator.

To anneal the μ resonator, the pulse voltage generator v_{anneal} is activated. Depending on the requirements, v_{anneal} is made to emit one or more voltage pulses of magnitude V_{anneal} for each annealing cycle. During each pulse, the potentials of the input and output electrodes, the ground plane, and one of the resonator anchors are raised by V_{anneal} , while the potential at the remaining resonator anchor remains constant at V_p . Thus, each pulse effectively applies a voltage across the resonator, from anchor to anchor, of magnitude V_{anneal} , which then sources a current I_{anneal} from anchor to anchor. This current flows through the resonator structure, dissipating a power given by

$$P_{anneal} = I_{anneal}^2 R_{struct}, \quad (8)$$

where R_{struct} is the resistance between the anchors of the resonator. Heat is thus generated throughout the resonator structure, raising its overall temperature and effectively annealing it. Frequency changes then result predominantly from anneal-activated stress changes in the structure.

Although long anneals using long voltage pulses can induce significant, permanent frequency shifts in released micromechanical resonators, they are not conducive to precise trimming of frequencies. For better precision, short pulses on the order of milliseconds are more appropriate. Figure 37 presents a plot of fractional frequency change versus trial with the number of pulses per trial as a third variable. For each trial, $V_{anneal}=7V$, $\tau_d=2$ ms, and $\tau_b=4$ ms (i.e., a 50% duty cycle was used). As shown, although little or no frequency change was seen for one and two pulse anneals, the frequency change per trial was very consistent for three and four pulse anneals. In addition, $\Delta f/f_0$ increased with the number pulses for these cases, which suggests some influence from total annealing time and/or thermal cycling on the frequency change per trial.

Beyond trimming of frequencies, the above localized annealing method has also been shown to raise the Q of micromechanical resonators [32], even using only annealing pulses. As Q -enhancement via localized annealing has been covered in previous reports and in [32], it will not be expanded upon here in the interest of this report's page count. Some aspects of it, however, are covered in the next section, in the context of *in situ* localized annealed Q -enhancement.

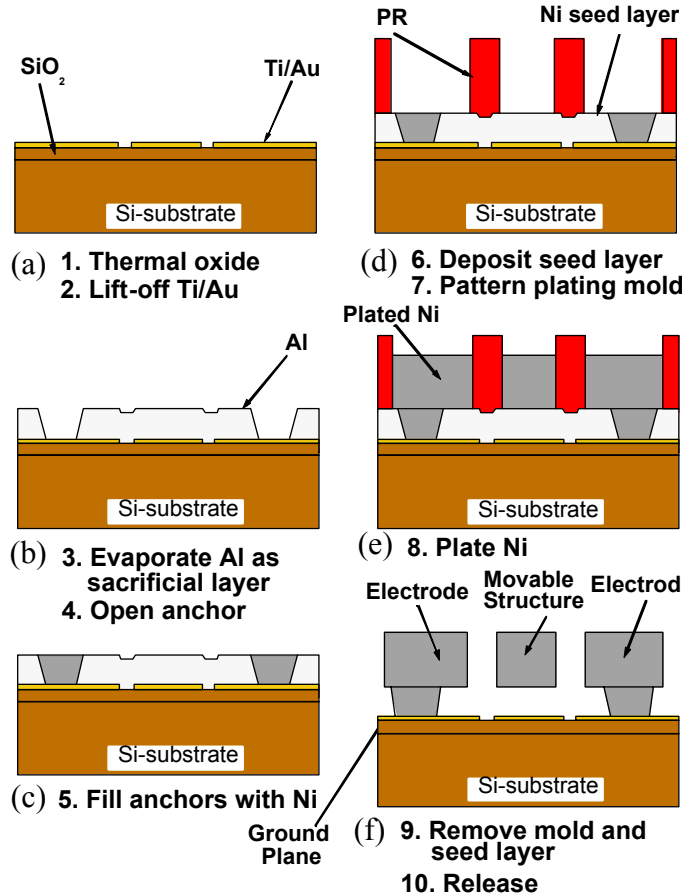


Fig. 38: Nickel surface micromachining process flow.

4.2.4. Nickel Micromechanical Resonators, Q -Enhancement, and Aging Studies

As discussed more fully in the Semi-Annual reports, excessive series resistance in polysilicon interconnect is responsible for Q -degradation in micromechanical resonators used for filters and oscillators, causing undue insertion loss in the former, and compromised phase noise performance in the latter. In part for this reason, and also because nickel is more amenable to direct planar integration with integrated circuit transistors (see Section 4.5.2), electroplated nickel was investigated as a potential structural material for use in high- Q resonator applications.

Several versions of an electroplated-nickel surface micromachining process technology, using aluminum as the sacrificial material, were developed over the course of this grant. The fabrication technology for nickel MEMS evolved as the importance of solid anchors for high Q operation became better understood. Figure 38 presents a cross-sectional flow diagram depicting the fabrication procedure for the most advanced process used to manufacture the nickel resonators of this work, which features selective electroplating of nickel plugs to fill in contact anchor openings before plating the actual nickel structures [27]. As shown in Fig. 38(f), weak points in the resonator-to-anchor attachments are eliminated with this process (provided there are no adhesion problems between successive nickel layers). Figure 39 shows the scanning electron micrograph (SEM) for a folded-beam, comb-driven nickel μ mechanical resonator fabricated via this latest process. Figure 40 shows a scanning electron micrograph (SEM) of a completed nickel resonator, featuring a geometric temperature compensation design (as detailed in Section 4.2.2, but this time for a folded-beam resonator) with the addition of special electrodes for localized annealing. A zoom-in SEM is also shown to better convey the surface roughness of the structural material.

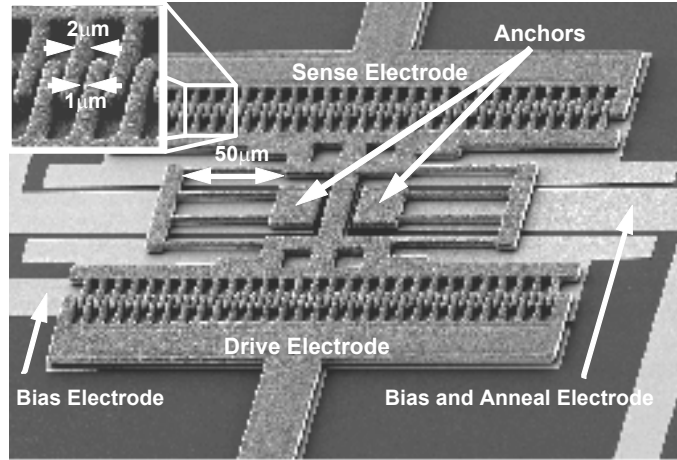


Fig. 39: SEM for a folded-beam, comb-driven Ni μ mechanical resonator using the new rigid-anchor process flow.

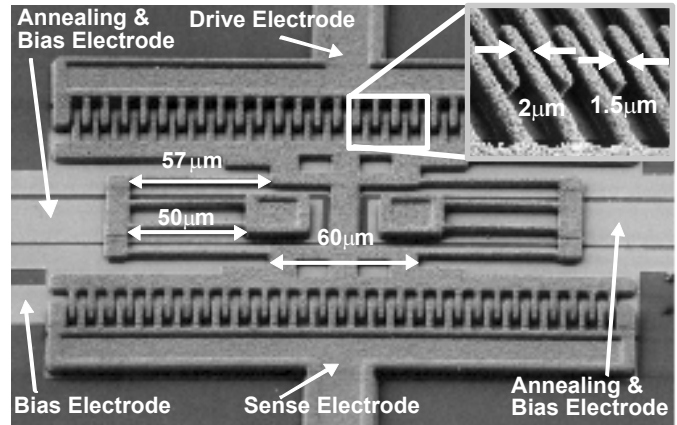


Fig. 40: SEM of a geometric-stress compensated nickel micromechanical resonator.

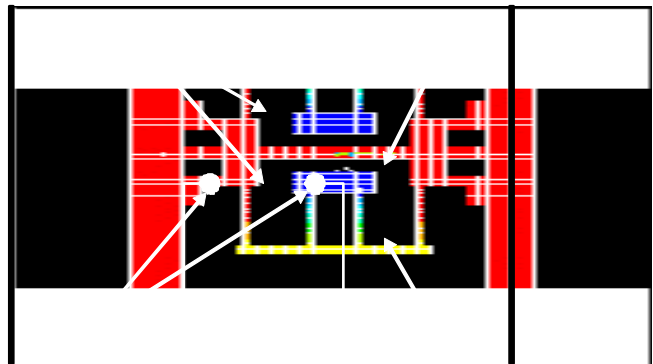


Fig. 41: FEM simulation of the temperature distribution on a localized annealed nickel micromechanical resonator.

Nickel μ mechanical resonators have so far proven very useful for attaining a better understanding of the physical mechanisms responsible for Q degradation and resonance instability in micro-scale mechanical resonators. In particular, freshly fabricated comb-transduced, folded-beam nickel μ mechanical resonators seem to be more susceptible to contamination than their polysilicon counterparts. This is supported by the observation that nickel μ resonator performance can consistently be improved via a set post-processing procedure involving localized annealing and an effective “work hardening” procedure. Specifically, upon initial testing, approximately 50% of freshly fabricated Ni μ resonators show inadequate Q and stability, consistent with previous versions of such resonators. It was discovered that a given resonator’s performance can be improved by operating it for a half-hour period at a very high temperature, achieved using a localized annealing procedure, in which voltages are applied across the resonator anchors, sending currents through the structure that heat it to temperatures exceeding 886°C . Figure 41 presents the temperature profile over a localized annealed Ni resonator with 1V applied between its anchors obtained via finite-element simulation (using ANSYS).

Figure 42 presents a plot of frequency versus time for two Ni μ mechanical resonators, both with Q ’s around 5,000 immediately after fabrication [27]. Of the two resonators, one is merely operated right after fabrication, while the other is taken through a post-process step in which it is operated for 1.5 hours while localized annealed to 886°C . After this post-process step, both resonators are taken to 127°C , where the post-processed one clearly shows better frequency stability. After operation at 127°C for a half hour, both resonators are taken down to 47°C , where again the annealed resonator exhibits much better stability. The Q of the annealed resonator is also now 13,297. Fig. 43 presents measured frequency characteristics for the nickel resonator before and after localized anneal-based post-processing, clearly showing the Q increase (along with a frequency decrease). The Q and stability enhancements of Fig. 43 were repeatable for all Ni μ resonators that exhibited low Q right after fabrication.

Once enhanced, μ resonator Q ’s remain high as long as they are kept in a controlled, vacuum environment. When removed from vacuum and exposed to less controlled environments, resonators often again exhibit low Q when returned to vacuum (although not as low as their values right after fabrication), but in most cases could again be taken back to high Q ’s via another localized annealing step.

To quantify these findings, the effect of humidity on device operation was investigated as follows:

- (i) *In situ* anneal a device in vacuum to achieve good stability and high Q ;
- (ii) place the device in a humidity chamber for a specified length of time and at specific values of percent humidity and temperature;
- (iii) return the device to vacuum and test immediately without any annealing, determining the frequency, Q , and stability, if possible; and

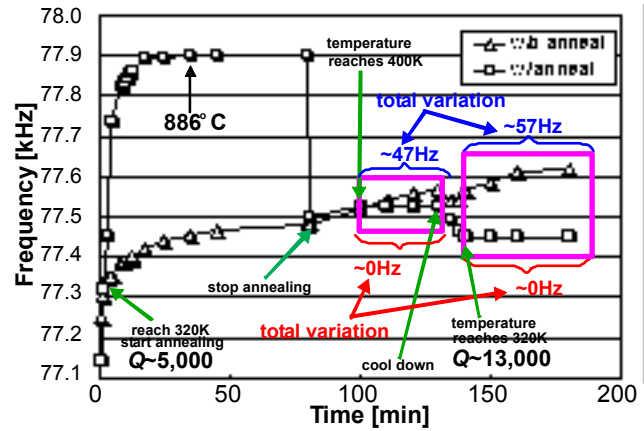


Fig. 42: Frequency versus time plot summarizing the procedure used to enhance the Q and frequency stability of a nickel micromechanical resonator.

(iv) *in situ* anneal the device and again determine frequency, Q , and stability.

The above procedure was applied to several nickel μ resonators under a variety of humidities and exposure times, and at chamber temperatures of 27°C and 50°C. Table I presents a subset of the results obtained at 50°C, plus results obtained under less controlled, but more natural, environments. The major observations over the course of these experiments can be summarized as follows:

- (1) Although all devices were designed to be identical, a rather large spread in frequencies is seen ($\sim 13\%$), about 30X higher than observed for polysilicon counterparts.
- (2) None of the environmental exposures noticeably affected the drift stability of any of the devices once returned to and operated in vacuum.
- (3) Exposures at 27°C had no effect on any devices, even at 90% humidity for 90 min.
- (4) Resonators exposed to environments with lower humidity-time totals at 50°C (e.g., cases 4, 6) were unaffected in both Q and stability.
- (5) For larger humidity-time totals (e.g., cases 1, 2, 3, 5) resonator Q 's were degraded, some so severely that they could not be operated after exposure. *In situ* localized annealing was able to recover original Q 's in all cases, except 1 and 3.
- (6) Q 's were recovered instantly by annealing alone (i.e., *in situ* not required).
- (7) Under particularly severe conditions (e.g., 1), *in situ* annealing could not recover the original Q .
- (8) For most cases in Table I, the frequency increases after exposure to humidity.

One possible explanation for observation (8) is mass removal by either (i) corrosion; or (ii) cleaning of device surfaces, both enabled via exposure to humid environments and accelerated by annealing.

Observation (2) seems to preclude a wet contaminant removal based mechanism for stability enhancement, supporting instead a mechanism where the combined operation (i.e. “working”) and annealing of a nickel μ resonator serve to redistribute or eradicate defects from the material towards a more relaxed, stable, and higher Q state.

Observation (6) gives evidence that before annealing, the Q -degradation in the Ni-plated devices of this work is dominated by surface contamination, which is removed by high temperature annealing to achieve higher Q 's. Once contaminants are removed, structural defects or internal stress fields take over as dominant loss mechanisms (best removed via *in situ* annealing). In addition, the fact that the Q of already annealed devices changes only when subjected to the rather high humidity-time totals of cases 1 and 3 in Table I, but not for others, gives some evidence that localized annealing under controlled environments may even also serve to passivate device surfaces against further contaminant-based Q -degradation.

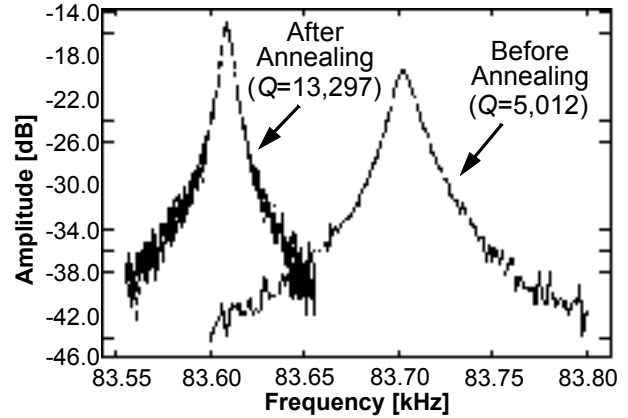


Fig. 43: Measured spectra for a nickel micromechanical resonator operated at a pressure of 30 μ Torr and a temperature of 47°C before and after localized annealing.

4.3. Micromechanical Signal Processor Circuit Design and Demonstration

Arguably, the activity with the farthest reaching impact developed under this grant has been the demonstration of the first micromechanical signal processing circuits with performances that equal or better the performances of off-chip macroscopic acoustic resonator circuits, and the demonstration of the first micromechanical mixer-filter (“mixler”) devices, all of which have potentially revolutionary impact on future communication transceivers.

Table I: Environmental Q -Degradation and Anneal-Activated Restoration

No.	Environments	Before Exposure		After Exposure		Annealing Techniques (Time[min])	After Annealing	
		f_o [Hz]	Q	f_o [Hz]	Q		f_o [Hz]	Q
1	50°C / 90% humidity / 90min	79,524	7,695	87,174	3,920	<i>in situ</i> (10)	87,176	4,198
2	50°C / 90% humidity / 15min	76,436	7,269	no resonance		static (0.2)	76,501	7,235
3	50°C / 80% humidity / 90min	81,016	6,688	91,476	2,179	<i>in situ</i> (10)	91,504	2,600
4	50°C / 80% humidity / 15min	88,392	8,302	88,511	8,475	n/a	n/a	n/a
5	50°C / 70% humidity / 90min	77,101	7,042	78,333	4,061	<i>in situ</i> (10)	77,133	7,269
6	50°C / 70% humidity / 60min	77,038	7,081	77,101	7,042	n/a	n/a	n/a
7	on an outside tree / 3 days	72,923	6,706	no resonance		<i>in situ</i> (20)	73,031	6,318
8	under a stairway / 3 days	82,768	6,941	no resonance		<i>in situ</i> (8)	83,790	7,418
9	inside EECS Building / 3 days	85,679	7,348	85,442	6,417	<i>in situ</i> (13)	85,664	7,252

4.3.1. Micromechanical Filters

The measured spectrum of Fig. 7 represents the frequency characteristic for a second-order, single-pole, bandpass filter centered at 8.5 MHz. Although useful for some applications, such as pilot tone filtering in mobile phones, second-order filter characteristics are generally inadequate for the majority of communications applications. Rather, bandpass filters such as depicted generically in Fig. 3 are required, with flatter passbands, sharper roll-offs, and greater stopband rejections.

To achieve the characteristic of Fig. 3, a number of micromechanical resonators are coupled together by soft coupling springs [15], [14], [33], as illustrated schematically in Fig. 44(a) using ideal mass-spring-damper elements. By linking resonators together using (ideally) massless springs, a coupled resonator system is achieved that now exhibits several modes of vibration. As illustrated in Fig. 45 for the coupled three-resonator system of Fig. 44, the frequency of each vibration mode corresponds to a distinct peak in the force-to-displacement frequency characteristic, and to a distinct, physical mode shape of the coupled mechanical resonator system. In the lowest frequency mode, all resonators vibrate in phase; in the middle frequency mode, the center

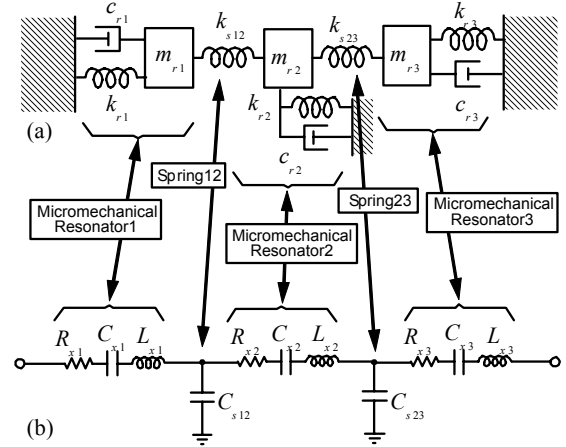


Fig. 44: (a) Equivalent lumped parameter mechanical circuit for a mechanical filter (b) Corresponding equivalent LCR network.

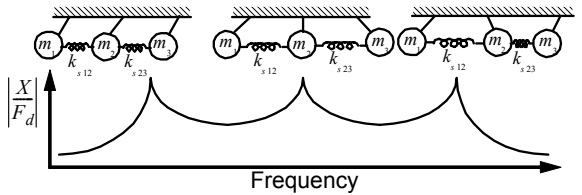


Fig. 45: Mode shapes of a three-resonator micromechanical filter and their corresponding frequency peaks.

resonator ideally remains motionless, while the end resonators vibrate 180° out of phase; and finally, in the highest frequency mode, each resonator is phase-shifted 180° from its adjacent neighbor. Without additional electronics, the complete mechanical filter exhibits the jagged passband seen in Fig. 45. As will be shown, termination resistors designed to lower the Q 's of the input and output resonators by specific amounts are required to flatten the passband and achieve a more recognizable filter characteristic, such as in Fig. 3.

In practical implementations, because planar IC processes typically exhibit substantially better *matching* tolerances than *absolute*, the constituent resonators in μ mechanical filters are normally designed to be identical, with identical dimensions and resonance frequencies. For such designs, the center frequency of the overall filter is equal to the resonance frequency f_o of the resonators, while the filter passband (i.e., the bandwidth) is determined by the spacings between the mode peaks.

The relative placement of the vibration peaks in the frequency characteristic—and thus, the passband of the eventual filter—is determined primarily by the stiffnesses of the coupling springs (k_{sij}) and of the constituent resonators at the coupling locations (k_r). Specifically, for a filter with center frequency f_o and bandwidth B , these stiffnesses must satisfy the expression [33]

$$B = \left(\frac{f_o}{k_{ij}} \right) \left(\frac{k_{sij}}{k_r} \right) \quad (9)$$

where k_{ij} is a normalized coupling coefficient found in filter cookbooks [16]. Note from (9) that filter bandwidth is not dependent on the absolute values of resonator and coupling beam stiffness; rather, their ratio k_{sij}/k_r dictates bandwidth. Thus, the procedure for designing a mechanical filter involves two main steps: first, design of a mechanical resonator with resonance frequency f_o and adjustable stiffness k_r ; and second, design of coupling springs with appropriate values of stiffness k_{sij} to enable a desired bandwidth within the adjustment range of resonator k_r 's.

To take advantage of the maturity of LC ladder filter synthesis techniques, the enormous database governing LC ladder filter implementations [16] and the wide availability of electrical circuit simulators, realization of the μ mechanical filter of Fig. 44(a) often also involves the design of an LC ladder version to fit the desired specification. The elements in the LC ladder design are then matched to lumped mechanical equivalents via electromechanical analogy, where inductance, capacitance, and resistance in the electrical domain equate to mass, compliance, and damping, respectively, in the mechanical domain. Figure 44(b) explicitly depicts the equivalence between the filter's lumped mass-spring-damper circuit and its electrical equivalent circuit. As shown, for this particular electromechanical analogy (the current analogy), each constituent resonator corresponds to a series LCR tank, while each (massless) coupling spring ideally corresponds to a shunt capacitor, with the whole coupled network corresponding to an LC ladder bandpass filter.

4.3.2. *A Two-Resonator, Tunable, Switchable, VHF Micromechanical Filter*

Figure 46 shows the perspective-view schematic of a practical two-resonator micromechanical filter [15], [14], capable of operation in the HF to VHF range. As shown, the filter consists of two μ mechanical clamped-clamped beam resonators, coupled mechanically by a soft spring, all suspended $0.1 \mu\text{m}$ above the substrate. Conductive (polysilicon) strips underlie each resonator, the center ones serving as capacitive transducer electrodes positioned to induce resonator vibration in a direction perpendicular to the substrate, the flanking ones serving as tuning electrodes

capable of voltage-controlled tuning of resonator frequencies. The resonator-to-electrode gaps are determined by the thickness of a sacrificial oxide spacer during fabrication and can thus be made quite small (e.g., 0.1 μm or less) to maximize electromechanical coupling.

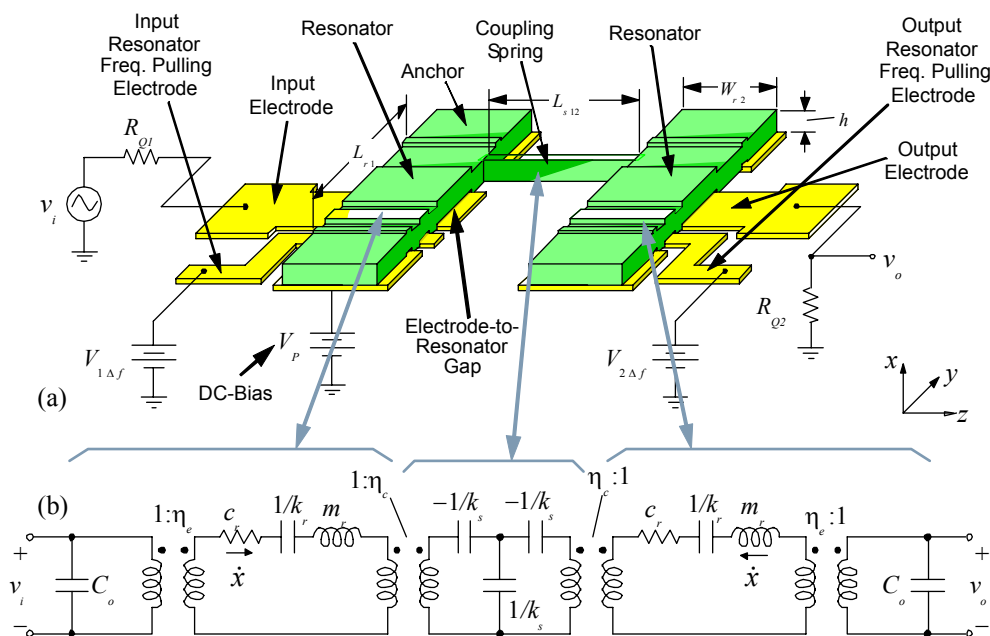


Fig. 46: (a) Perspective-view schematic of a two-resonator VHF μ mechanical filter with typical bias, excitation, and signal conditioning electronics. (b) Electrical equivalent circuit for the filter in (a). Here, m , k , and c denote the mass, stiffness, and damping of the (identical) resonators at the drive electrode locations, and $\eta = V(\partial C/\partial x)$ and $\eta = (k/k)^{0.5}$ are turns ratios modeling electromechanical coupling at the inputs and mechanical impedance transformations at low velocity coupling locations.

In effect, the operation of the above filter can be briefly summarized as follows:

- (3) the mechanically processed signal appears as motion of the output resonator and is re-converted to electrical energy at the output transducer, ready for processing by subsequent transceiver stages.

As can be surmised from Fig. 44(b), the network topologies for the mechanical filters of this work differ very little from those of their purely electronic counterparts, and in principal, can be designed at the system-level via a procedure derived from well-known, coupled resonator ladder filter synthesis techniques. In particular, given the equivalent LCR element values for a prototype μ mechanical resonator, it is possible to synthesize a mechanical filter entirely in the electrical domain, converting to the mechanical domain only as the last step. However, although possible, such a procedure is not recommended, since knowledge and ease of design in both electrical and mechanical domains can greatly reduce the effort required.

The design procedure for the two-resonator micromechanical filter of this work can be itemized as follows:

- (1) *Design and establish the μ mechanical resonator prototype to be used, choosing necessary geometries for the needed frequency and insuring that enough electrode-to-resonator transducer coupling is provided to allow for predetermined termination resistor values.* With predetermined values of W_r , h , W_e , V_P , and R_Q , this amounts to solving for the resonator length L_r and electrode-to-resonator gap spacing d that simultaneously satisfy the frequency equation and the equation for the needed termination resistor [15]:

$$R_{Q_n} = \left(\frac{Q_{res}}{q_n Q_{fltr}} - 1 \right) \frac{c_r}{\eta_e^2} = \left(\frac{Q_{res}}{q_n Q_{fltr}} - 1 \right) R_{x_n}, \quad (10)$$

where Q_{res} is the uncontrolled quality factor of the constituent resonators, $Q_{fltr} = f_o/B$, n refers to the port in question, q_n is a normalized q parameter obtained from a filter cookbook [16], c_r and η_e are defined in the caption of Fig. 46(b), and R_x is the series motional resistance of an end resonator.

- (2) *Choose a manufacturable value of coupling beam width W_s and design coupling beam(s) corresponding to a “quarter-wavelength” of the filter center frequency.* Here, the coupling beam is recognized as an acoustic transmission line that can be made transparent to the filter when designed with quarter-wavelength dimensions [15]. For a flexural-mode coupling beam, neglecting rotational movements at the resonator attachment points, quarter-wavelength dimensions are achieved when W_s and L_s are chosen to satisfy the expression [15]

$$H6 = \sinh \alpha \cos \alpha + \cosh \alpha \sin \alpha = 0, \quad (11)$$

where $\alpha = L_s(\rho W_s h \omega^2 / (EI_s))^{0.25}$, $I_s = W_s h^3 / 12$, and needed dimensions are given in Fig. 46(a). Note that in choosing W_s and L_s to satisfy (11), the coupling beam stiffness k_{s12} is constrained to a particular value, given by [15]

$$k_{s12} = - \frac{EI_s \alpha^3 (\sin \alpha + \sinh \alpha)}{L_s^3 (\cos \alpha \cosh \alpha - 1)}. \quad (12)$$

Note that this also constrains the ability to set the bandwidth of the filter via the coupling beam dimensions, and thus, necessitates an alternative method for setting bandwidth.

- (3) *Determine the coupling location(s) on the resonators corresponding to the filter bandwidth of interest.* This procedure is based upon two important properties of this filter and the resonators comprising it: First, the filter bandwidth B is determined not by absolute values of stiffness, but rather by a ratio of stiffnesses (k_{s12}/k_r); and second, the value of resonator stiffness k_r varies with location (in particular, with velocity) and so can be set to a desired value by simply choosing an appropriate coupling beam attachment point. Specifically, the resonator stiffness k_r can be expressed as [15]

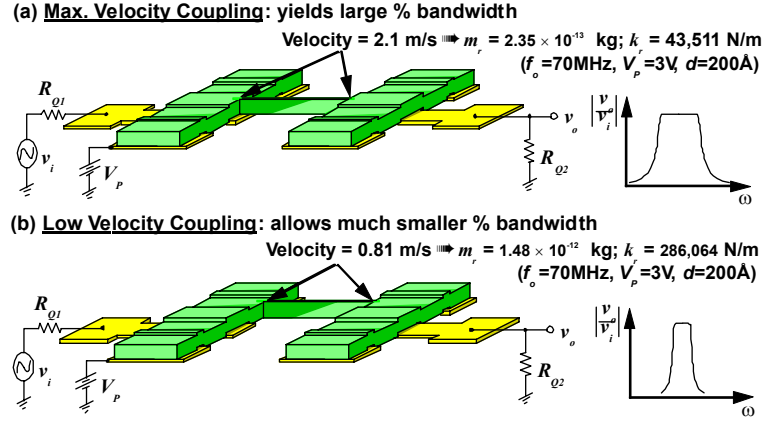


Fig. 47: Filter schematics showing (a) maximum velocity coupling to yield a large percent bandwidth and (b) low velocity coupling to yield a smaller percent bandwidth.

$$k_r(y) = \omega_o^2 m_r(y), \quad (13)$$

where ω_o is the radian resonance frequency, m_r is effective mass as a function of location given by

$$m_r(y) = \frac{\rho W_r h \int_0^{L_r} [X(y')]^2 dy'}{[X(y)]^2}, \text{ where } X(y) = (\cos ky - \cosh ky) - \sigma_n (\sin ky - \sinh ky), \quad (14)$$

and where ρ is the density of the structural material, $k = 4.73/L_r$ and $\sigma_n = 0.9825$ for the fundamental mode, and dimensions are indicated in Fig. 7. Figure 47 illustrates how the choice of coupling beam attachment point can greatly influence the bandwidth of a mechanical filter. In Fig. 47(a), the coupling beam is attached at the highest velocity point, where the resonator presents its smallest stiffness, resulting in a very wide filter bandwidth. On the other hand, Fig. 47(b) depicts coupling at a lower velocity point closer to the resonator anchors, where the resonator presents a much higher stiffness, leading to a much smaller percent bandwidth, as dictated by (9). In effect, the bandwidth of the filter is set not by choosing the coupling beam stiffness k_{s12} , but rather by choosing an appropriate value of resonator stiffness k_r to satisfy (9), given a k_{s12} constrained by quarter-wavelength design.

- (4) *Generate a complete equivalent circuit for the overall filter and verify the design using a circuit simulator.* Figure 46(b) presents the equivalent circuit for a two-resonator micromechanical filter along with equations for the elements.

Through the electrical spring stiffness k_e , the resonance frequency of this device is tunable via adjustment of the dc-bias voltage V_P , and this can be used advantageously to implement filters with tunable center frequencies, or to correct for passband distortion caused by finite planar fabrication tolerances. This, combined with the switchability attained by merely switching the dc-bias voltage V_P on or off, makes the micromechanical filter of Fig. 46 nearly ideal for the RF channel-select architecture of Fig. 85 (to be described). The switching nature of this device can actually be further exploited to implement a combined mixing and gain function in this same device. In particular, by introducing a local oscillator signal into the bias voltage of the input resonator, the square law voltage-to-force transfer function in the input transducer can be harnessed for both mixing and parametric gain. Using this principle, mixing, filtering, and gain in a single micromechanical device was recently demonstrated [34].

The SEM for a 34.5 MHz, two-resonator, low-velocity coupled micromechanical filter constructed of phosphorous-doped polysilicon is shown in Fig. 48 along with relevant design dimensions. The measured transmission spectrum for an $L_r/8$ -coupled version of this filter achieved with $V_P=15V$ and $R_{Qn}=2k\Omega$ is presented in Fig. 49. As shown, a percent bandwidth of 1.3% was achieved with an associated insertion loss of less than 2 dB at its peak, and a stopband rejection exceeding 20 dB. With the use of additional resonators, even better performance is achievable, with sharper roll-offs (i.e., smaller shape factors) and larger stopband rejections [14].

4.3.3. High-Order Micromechanical Filters

The described two-resonator filters, although useful in many instruments, lack the required passband-to-stopband roll-off steepness for use in the majority of communications applications. To achieve steeper roll-offs, higher filter order is required, which in turn requires the use of more resonators. For the case of the mechanical filters of interest, filter order is equivalent to two times the number of resonators used.

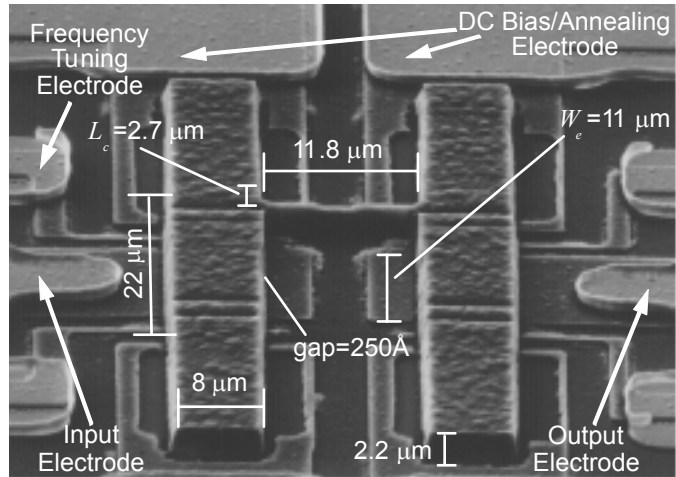


Fig. 48: SEM of a 34.5 MHz switchable, tunable, μ mechanical filter with important dimensions.

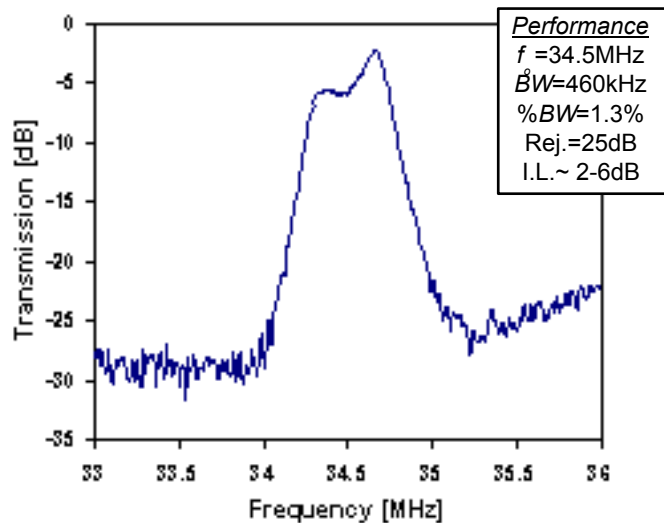


Fig. 49: Measured transmission spectrum for a VHF two-resonator micromechanical filter, such as shown in Fig. 48.

For the purpose of demonstration, higher order three-resonator filters were designed using more conservative folded-beam, capacitive-comb transduced resonators. As previously mentioned, such resonators are not optimized for high frequency operation. However, they are advantageous for research purposes, since control and operation of these classic resonators is facilitated by the availability of direct visual observation. Furthermore, it was anticipated (correctly) that filters with more than

two resonators are substantially more difficult to demonstrate, since they are much more susceptible to fabrication mismatch tolerances and electrical parasitics than are two-resonator filters. Given this sensitivity to electrical parasitics, and given that board-level sense electronics were being used for this first demonstration, lower operation frequency was a welcome simplification.

Figure 50 presents a perspective view schematic of the designed three-resonator filter [14], explicitly depicting its lumped mass-spring-damper equivalent circuit. As previously mentioned, folded-beam comb-driven resonators are utilized, coupled at their folding-trusses by flexural mode beams. Coupling is done at the folding-trusses to take advantage of the lower resonance velocity at these locations, which relaxes requirements on coupling beam dimensions for filters with very small percent bandwidth [14]. Also, as shown in Fig. 50, all resonators in this design are also equipped with parallel-plate frequency tuning electrodes, which allow the passband to be corrected by adjustment of dc-bias voltages, in the event of substantial post-fabrication resonator-to-resonator frequency mismatch [14].

Three-resonator filters using the design of Fig. 50 were fabricated using a polysilicon surface micromachining process, in which the structural material was doped via phosphorous implantation. Wide-view and close-in scanning electron micrographs of a fabricated three-resonator filter are presented in Fig. 51. Figure 52 shows the measured spectrum for this filter, indicating a center frequency of 360 kHz with a bandwidth of 450 Hz, more than 48 dB of stopband rejection, and an impressive insertion loss (for this 0.125% bandwidth filter) of only 0.8dB. All things equivalent, this performance (particularly insertion loss) rivals or betters that of crystal filters, which are some of best filters currently available (but also some of the bulkiest).

It should be noted that a significant amount of passband tuning was required for this particular filter. Although the degree of tuning necessary was consistent with the matching tolerances available in our research laboratory, it is expected that some amount of frequency trimming or tuning will still be beneficial for better-controlled production line filters, as even small resonator-to-resonator mismatches can generate passband distortion in filters with extremely small percent

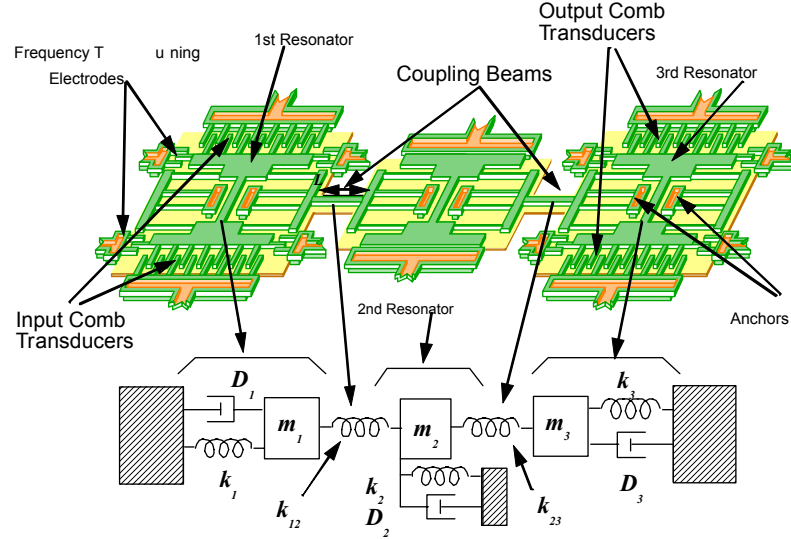


Fig. 50: Perspective view schematic of the designed three-resonator micro mechanical filter, showing the equivalence to a lumped mass-spring-damper mechanical circuit.

bandwidth. A frequency trimming technique suited for this was described in Section 4.2.3 of this report.

4.3.4. Parallel Microresonator Filters

With the recognition that trimming or tuning will probably be necessary anyway for small percent bandwidth filters, we also investigated an alternative filter architecture, in which parallel resonators are coupled electrically, rather than mechanically. By dispensing with rigid mechanical spring coupling, this parallel-resonator filter architecture both alleviates fabrication complexity associated with coupling springs (which can require submicron resolution for small filter bandwidths), and introduces real-time reconfigurability and bandwidth-tuning capabilities previously unavailable with spring-coupled architectures. Figure 53 presents a schematic diagram depicting this parallel resonator filter architecture, along with the bias and excitation scheme used to operate the filter [36]. As shown, a dc bias potential V_P is applied to the resonator and ac voltage inputs of opposite polarity are applied to each of the underlying resonator electrodes. A dc voltage V_{Af} is also added to one of the inputs. The dc bias V_P serves to enhance force components at the frequency of the excitation signal and to provide an output current when the beam vibrates. V_{Af} serves to electrostatically tune the frequency of one of the resonators, thus tuning the frequency difference between the constituent resonators. Such tuning is made possible by the nonlinear dependence of resonator-to-electrode capacitance on displacement, and is governed via the expression [36]

$$f_o' = f_o \left(1 - \frac{(V_P - V_{Af})^2}{k_r} \frac{C_{on}}{d^2} \right)^{1/2} \quad (15)$$

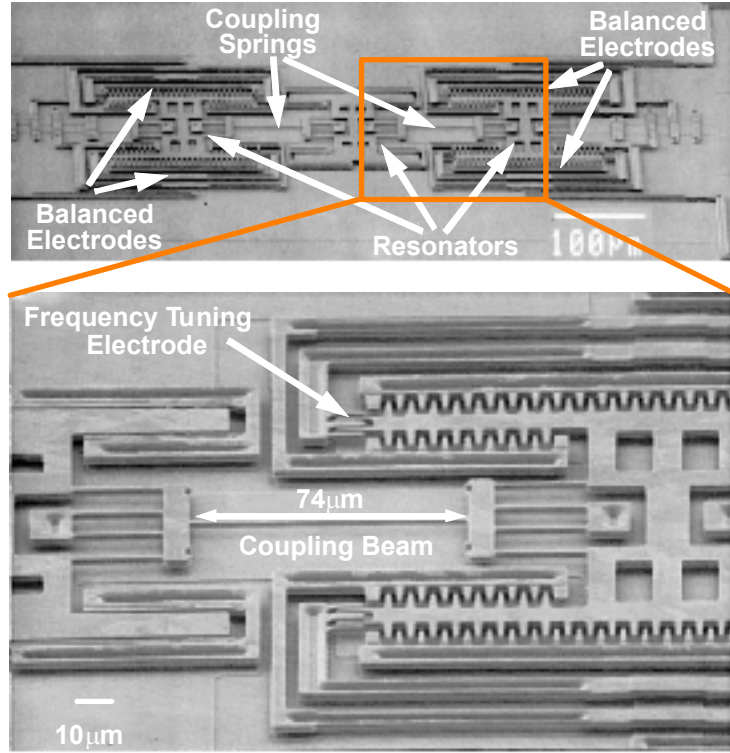


Fig. 51: Wide-view and close-in SEM's of a fabricated three-resonator micromechanical filter.

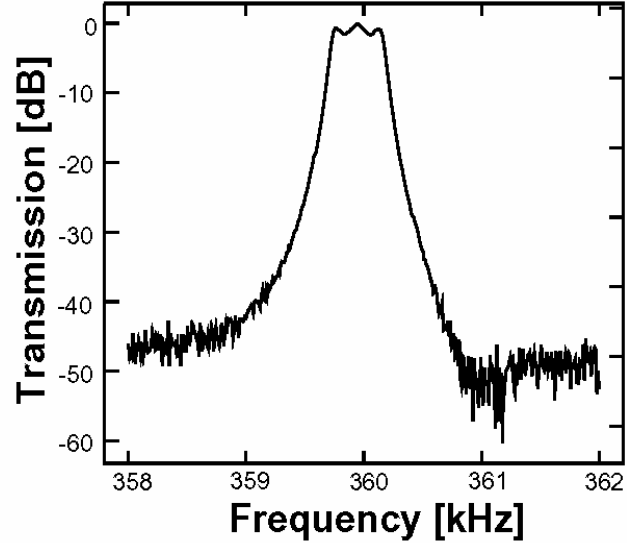


Fig. 52: Measured frequency spectrum for the filter of Fig. 51.

where f_0 is the initial beam resonance frequency, f_0' is the adjusted resonance frequency, k_r is the effective spring constant of the beam, C_{on} is the static resonator-to-electrode capacitance at electrode n , and d is the resonator-to-electrode gap spacing. For the filter of this work, 3.3% frequency tuning was feasible over a 2 V change in $V_{\Delta f}$.

When the frequency of the ac input signal enters the passband of one or both of the constituent resonators, the resonator(s) vibrate in a direction perpendicular to the substrate, creating dc-biased time varying capacitors between the resonators and their respective underlying electrodes. Currents are thus generated between the electrodes and resonators, given by $i_{xn} = V_{pn}(\partial C_n / \partial t)$, where V_{pn} is the dc voltage between resonator and electrode at port n , and C_n is the electrode-to-resonator overlap capacitance at port n . The output currents from the constituent resonators are then summed into Q -control resistor R_Q , then buffered to an output voltage.

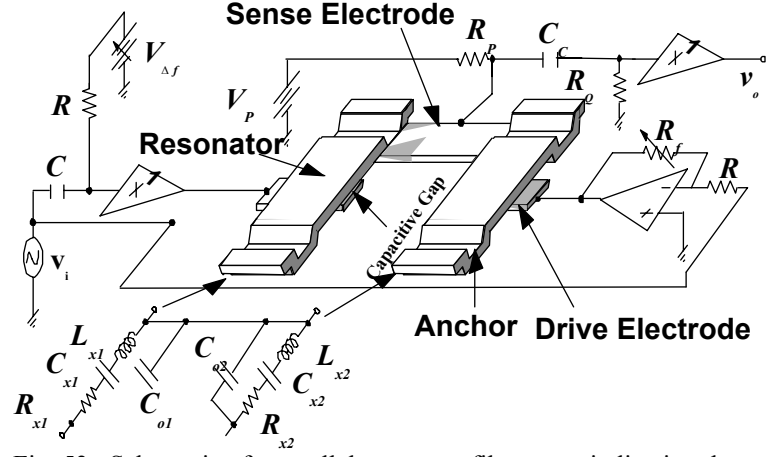


Fig. 53: Schematic of a parallel-resonator filter, indicating the required bias and excitation scheme, and identifying key components.

As before, the mechanical resonators comprising the filter can be modelled in the electrical domain via electromechanical analogy, where each mechanical resonator corresponds to an equivalent series LCR circuit. The equivalent circuit representing the filter and electrode configuration is also shown in Fig. 53, along with equations for the elements. Using this circuit in combination with Fig. 53, the filter is seen to operate via combination of the properly phased current outputs of the individual resonators. As shown in Fig. 54, inputs v_i at frequencies between the resonances of the microresonators generate output currents that are in phase, and thus, add, creating a flat passband in this frequency range. Those at frequencies outside this interval generate output currents 180° out of phase, which subtract to provide a steeper roll-off and improved stopband rejection. As shown, a two-resonator filter made in this manner provides a fourth order bandpass characteristic. Higher order filters, with sharper roll-offs and larger stopband rejections, can also be implemented using the same principles with a larger number of micromechanical resonators.

The bandwidth and ripple of the prototype fourth order filter is determined by the frequency separation Δf of the constituent resonators and their quality factor Q . The frequency separation Δf can be controlled via $V_{\Delta f}$, as governed by (15), while the Q of the constituent resonators is controllable through the resistor R_Q in Fig. 53. Thus, by adjusting these two variables, a wide variety of bandwidths are possible, and adaptive filters should be achievable through intelligent circuitry. For a maximally flat passband (i.e., a Butterworth characteristic), Δf and Q should be chosen such that

$$Q = \frac{f_c}{\Delta f}, \quad (16)$$

where f_c is the center frequency of the filter.

An HF version of this filter was implemented by combining the outputs of two stand-alone resonators fabricated on the same die as the filter of Fig. 7. Using the set-up of Fig. 53 in our custom vacuum chamber, filter characteristics were obtained, and are shown in Fig. 55. Here, the filter is seen to be centered at 14.5 MHz with a bandwidth of 12 kHz, corresponding to an overall filter Q of 1,208. The insertion loss of about 13 dB is caused by two sources: (1) low resonator Q ; and (2) off-chip, board-level parasitic capacitance, which causes phase lag in the individual resonator responses, consequent passband distortion, and insertion loss after passband correction. The Q of the individual resonators was only 2,000 due to the use of boron source doping, which pitted the surface of polysilicon structural material, probably degrading the Q . The parasitic capacitances can be greatly reduced via full integration or an on-chip bonding approach. However, the observation still remains that these parallel-resonator filters, although more tunable, seem to be more susceptible to electrical parasitics than their spring-coupled counterparts.

4.3.5. Micromechanical Mixer-Filters (“Mixlers”)

Beyond frequency filters, this grant demonstrated that micromechanical circuits can do much more than linear signal processing, and that nonlinear functions were also within the realm of possibilities. One major and potentially revolutionary accomplishment over the course of this grant was the demonstration of a mixer-filter device, that performs both low-loss frequency translation (i.e., mixing) and highly selective filtering of applied electrical input signals, all achieved using a passive micromechanical filter structure [34]. In particular, successful down-conversion of radio frequency (RF) signals from 50-200 MHz and subsequent filtering at a 34.5 MHz intermediate frequency (IF) with less than 5 dB of combined mixing conversion and filter insertion loss is demonstrated using this single, micromechanical device. Such a device can potentially replace both the filtering and mixing functions in heterodyning wireless communication transceivers (as shown in Figure 56), reducing both size (by orders of magnitude) and power dissipation over the off-chip macroscopic counterparts often used in current systems.

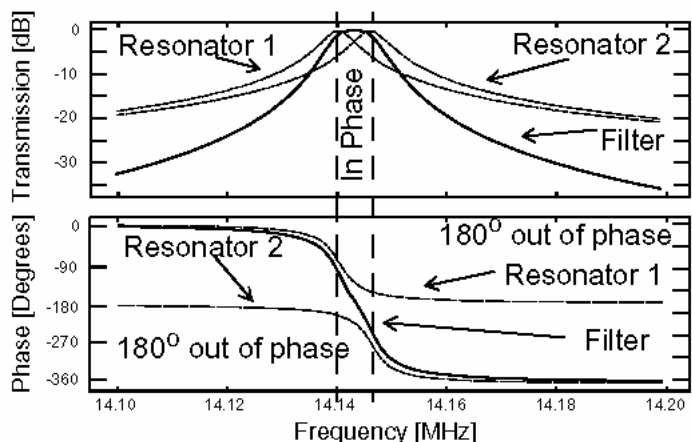


Fig. 54: Bode plot depiction of the mechanism behind parallel microresonator bandpass filters.

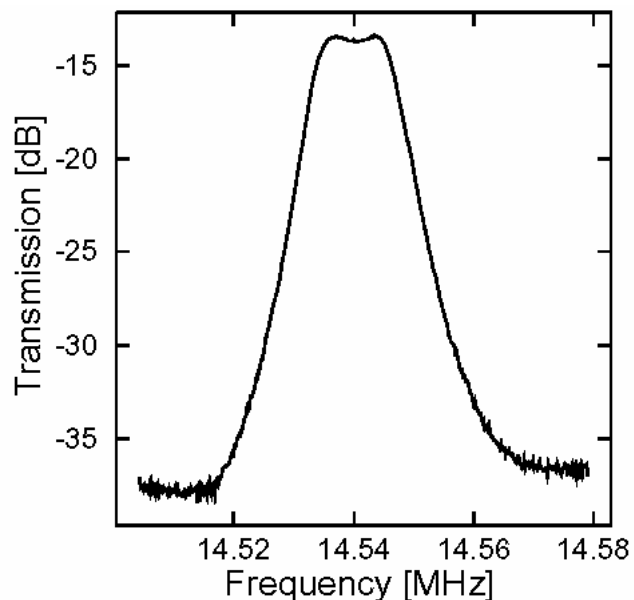


Fig. 55: Measured frequency spectrum for a 15 MHz parallel-resonator filter.

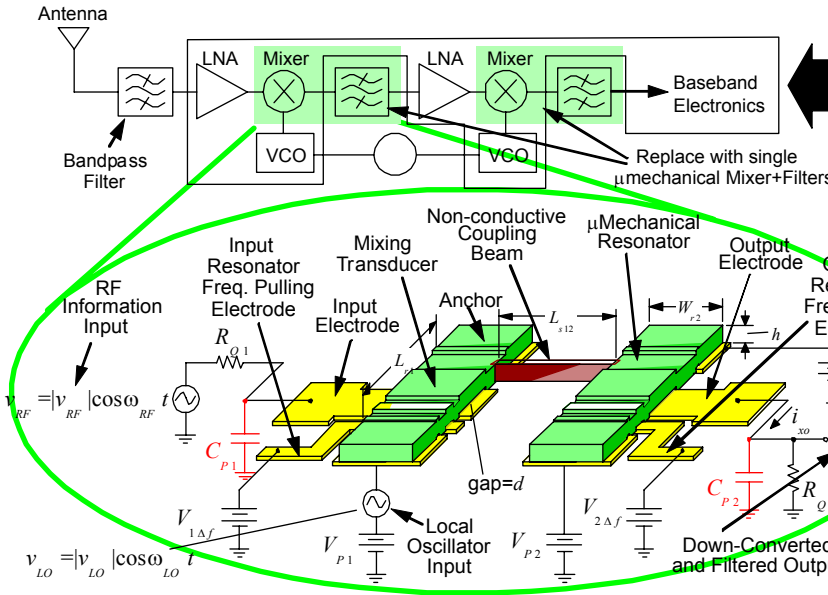


Fig. 56: Simplified block diagram of a wireless receiver, indicating (with shading) the components replaceable by the subject mixer+filter devices.

Fig. 57: (a) Schematic diagram of the described μ mechanical mixer+filter, depicting the bias and excitation scheme needed for down-conversion. (b) Equivalent block diagram of the mixer+filter scheme.

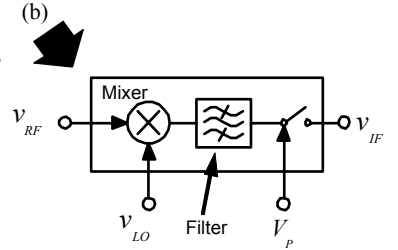


Figure 57(a) presents the perspective-view schematic of the mixer-filter, indicating important components and specifying the needed excitation configuration. As shown, this device is comprised of a frequency-tunable spring coupled micromechanical filter [13] with center frequency f_{IF} and with very specific input placements: a local oscillator input v_{LO} with frequency f_{LO} applied to the input resonator; an information (or RF) input v_{RF} with frequency $f_{RF}=f_{IF}+f_{LO}$ (consistent with actual inputs to communication transceivers) applied to the terminated input electrode; and one or more dc-biases V_{Pn} 's applied to the filter structure. Even though none of the applied signals shown in Figure 57(a) is within the passband of the micromechanical filter, a *force* component *within* the filter passband still arises at the input due to quadratic nonlinearity in the voltage-to-force capacitive input transducer. Specifically, this force F_i is given by:

$$F_i = -\frac{1}{2}(V_P + v_{LO} - v_{RF})^2 \left(\frac{\partial C_i}{\partial x} \right) = \dots + v_{LO} v_{RF} \frac{\partial C_i}{\partial x} + \dots + \frac{1}{2} |v_{LO}| |v_{RF}| \frac{\partial C_i}{\partial x} \cos(\omega_{RF} - \omega_{LO})t + \dots \quad (17)$$

where V_P is the applied dc-bias, v_{LO} is the local oscillator signal, v_{RF} is the input RF signal, dC_i/dx is the incremental change in beam-to-input electrode capacitance, and where the mixed component of interest has been singled out. The frequency of the force falls within the filter passband when $f_{RF}=f_{LO}+f_{IF}$, at which point vibration is induced in the micromechanical filter section, and a subsequent filtered signal is generated by the dc-biased, time varying capacitor at the output transducer. Note from (17) that gain is also possible via this device if the amplitude of the local oscillator $|v_{LO}|$ is chosen sufficiently large. A parametric amplification is in fact attained in this fashion, where ac (rather than dc) power is used to obtain gain. Thus, if designed correctly, the overall micromechanical filter device can serve a combined mixer-filter-gain function, replacing all three of these components in each down-conversion step within a super-heterodyne receiver.

Figure 58 shows SEM's of the 34.5 MHz two-resonator filter used to demonstrate the mixer+filter function, with appropriate dimensions indicated in Table II. The experimental set-up used to evaluate the performance of this device is depicted schematically in Figure 59. Here, a 15 MHz local oscillator and input signals around 50 MHz are supplied by two function generators, and a spectrum analyzer is used to sense the output signal at the IF frequency (i.e, the filter passband frequency, centered around 34.5 MHz). Figure 60 shows the spectrum obtained when sweeping the RF input v_{RF} over a 47 MHz to 55 MHz frequency range while detecting and hold-

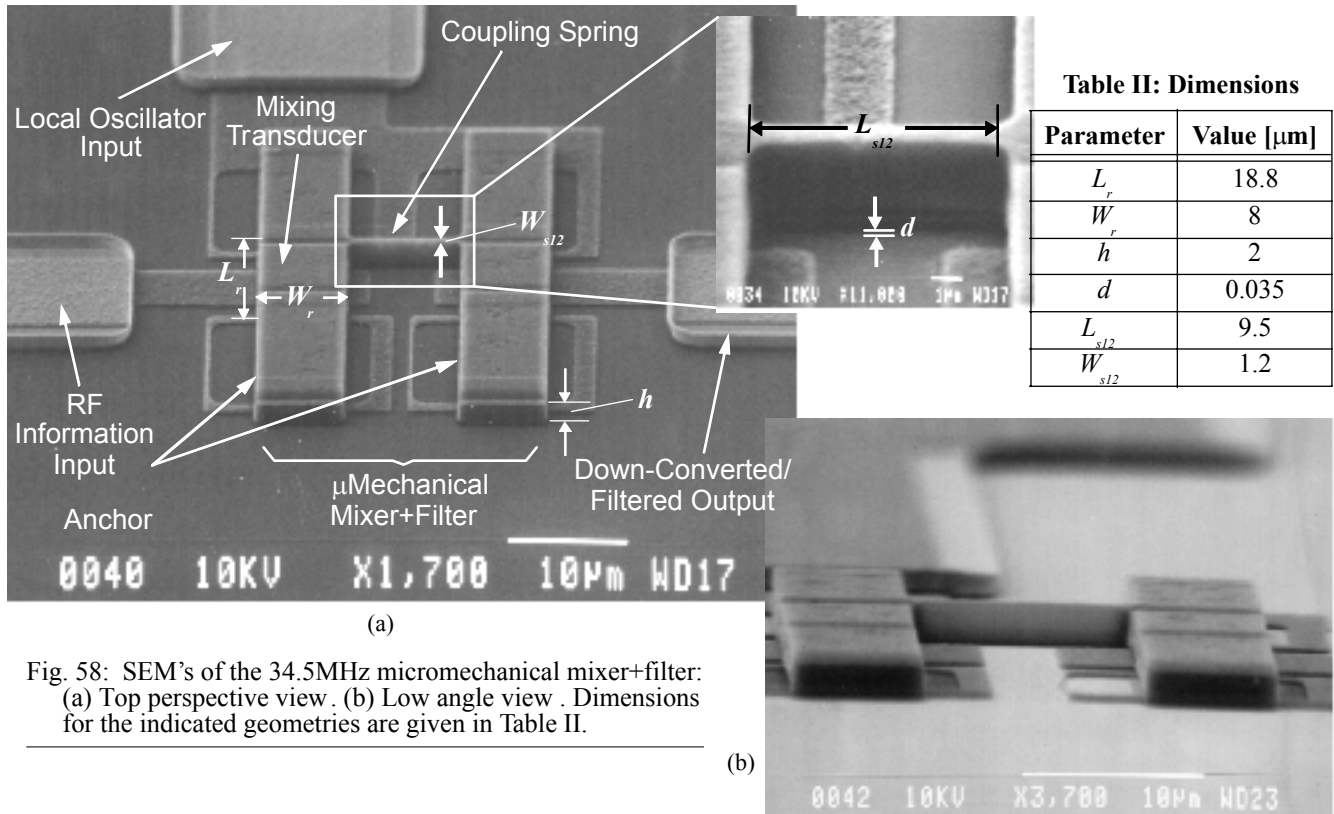


Fig. 58: SEM's of the 34.5MHz micromechanical mixer+filter: (a) Top perspective view. (b) Low angle view. Dimensions for the indicated geometries are given in Table II.

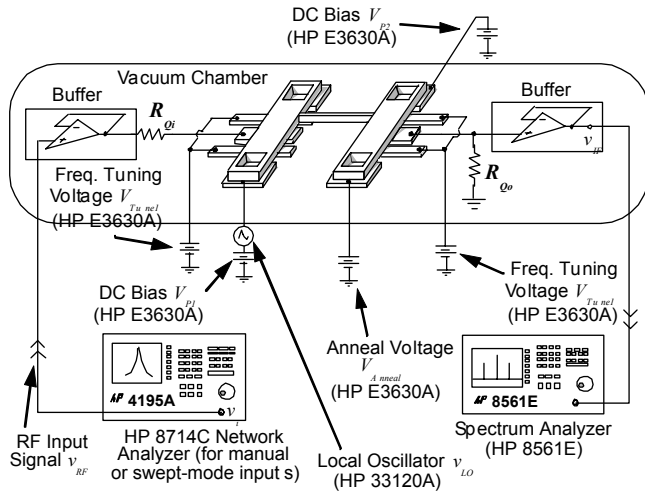
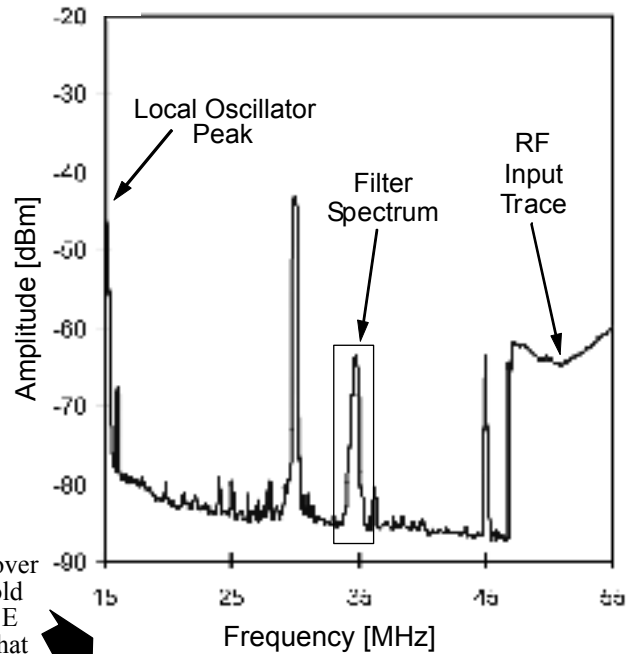


Fig. 59: Experimental set-up for mixer+filter evaluation.

Fig. 60: Spectrum obtained when sweeping the RF input v_{RF} over a 47MHz to 55MHz frequency range while detecting and holding outputs (using the MAX HOLD function on an HP 8561E Spectrum Analyzer) over a 15MHz to 55MHz range. Note that some peaking is seen in the filter spectrum, because the micro mechanical filter is not terminated exactly. A flatter spectrum is achievable with proper termination.



ing outputs (using the MAX HOLD function on an HP 8561E Spectrum Analyzer) over a 15 MHz to 55 MHz range. This procedure allows measurement of a network spectrum using an input signal at a different frequency from the sensed signal and clearly shows the “max held” RF

input trace (47-55 MHz) and the resulting filter response trace at the IF frequency (34.5 MHz), indicating down-conversion of inputs from RF to IF. RF inputs as high as 200 MHz (limited only by our function generators) have also been down-converted, and theory predicts successful mixing for RF input frequencies past 20 GHz.

4.4. Other RF MEMS Devices

Although the focus of this work was on vibrating RF MEMS devices, some work was also done on micromechanical tunable capacitors over the course of this grant. In particular, a high- Q , tunable, micromechanical capacitor has been realized using an IC-compatible, electroplated-metal, surface-micromachining technology and demonstrated with quality (Q -) factors in excess of 290—the highest reported to date for on-chip tunable capacitors at frequencies near 1 GHz [35]. The key feature in this design that makes possible such high on-chip Q is the method for capacitive tuning, which in this design is based on moving the dielectric between the capacitor plates, rather than moving the plates themselves, as done in previous designs. One version of this design achieves a measured Q of 291 at 1 GHz ($C=1.21\text{pF}$) with a tuning range of 7.7% over 10V of control voltage, and an expected self-resonant frequency (SRF) of 19GHz. In another design, with a wider tuning range of 40% over 10V, a Q of 218 is achieved at 1 GHz ($C=1.14\text{pF}$).

Figure 61 presents conceptual and perspective-view schematics of the new tunable capacitor design, identifying key components and specifying a preferred actuation voltage configuration. As shown, the structure features a bottom capacitor plate fixed to the substrate, and a top capacitor plate suspended above the former, but rigidly anchored to the substrate, and unable to move. Both plates are constructed of copper (Cu) to minimize their total series resistance, and thus maximize the device Q . A dielectric slab is suspended between the two plates and anchored to the substrate outside the two plates via spring structures. This dielectric is free to move, and can be electrostatically displaced to alter either the overlap between it and the capacitor plates, or the fringing fields between them. In the former case, when a DC bias is applied between the two plates, the charges on the capacitor plates exert an electrostatic force on the induced charges in the dielectric to pull the dielectric into the gap, as shown in Fig. 61(a). The waffle shape of the structure shown in Fig. 61(b) (also in Fig. 63) is designed to minimize the travel distance (or the needed voltage) required for a given change in capacitance, and to provide etchant access paths during a sacrificial-layer etching step in the fabrication process.

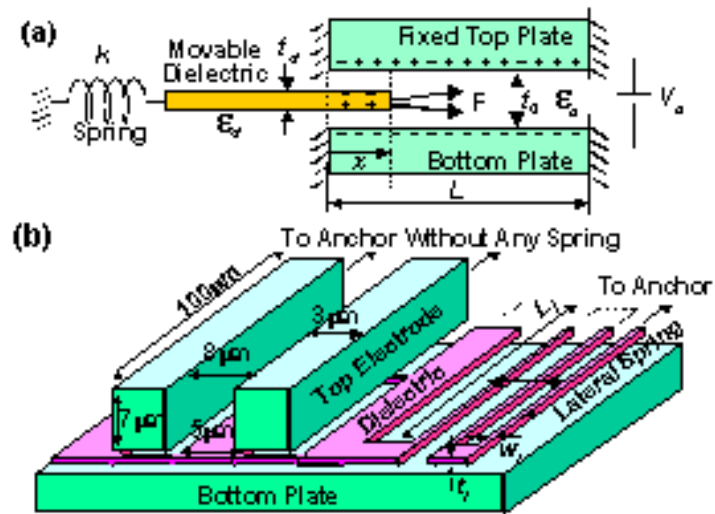


Fig. 61: Micromachined tunable capacitor. (a) Conceptual schematic. (b) Actual structure designed with a lateral spring.

Via use of a movable dielectric rather than a movable top capacitor plate (as done in previous designs [37], [38]), the tunable micromechanical capacitor of this work benefits from the following key advantages: (1) Unlike its predecessors, the top capacitor plate in this design need no

longer be suspended by lengthy springs that can add series resistance, and thus, lower the Q . Instead, a very thick top plate can be used without any suspension to lower series resistance and greatly increase the Q . (2) The tuning range in this design is set by the ratio of the dielectric thickness to the capacitive plate gap, and can be made quite large via proper design, without concern for pull-down phenomena that often limit previous movable-top-plate designs [37]. (3) No top-to-bottom plate electrical shortage can happen in this movable dielectric design.

Figure 62 illustrates the fabrication process used for this work. The process begins with the thermal growth of $1\mu\text{m}$ of SiO_2 to serve as an isolation layer between eventual metal structures and the silicon substrate. Next, the bottom capacitor plate is formed by first evaporating $300\text{\AA}/2000\text{\AA}$ of a Cr/ Cu seed layer, then electroplating $5\mu\text{m}$ of copper (Cu) (for which the sheet resistance = $4.2\text{m}\Omega/\text{sq.}$). 3000\AA of nickel (Ni) is then electroplated above the Cu (c.f., Fig. 62(a)) to serve as a buffer layer to prevent Cu contamination of etch chambers during subsequent RIE processes. Next, a 2000\AA aluminum (Al) sacrificial layer is evaporated and patterned to form vias through which a subsequent PECVD nitride dielectric film adheres to the underlying Ni. The nitride film is patterned via RIE to form the movable dielectric plate (c.f., Fig. 62(b)), then submerged under $0.9\mu\text{m}$ of a second sacrificial Al film that defines the spacing between the dielectric plate and the eventual top metal plate. Due to the valley-like topography between the fingers of the etched dielectric, the deposition of $0.9\mu\text{m}$ of Al actually results in only a $0.3\mu\text{m}$ gap between the top plate and the dielec-

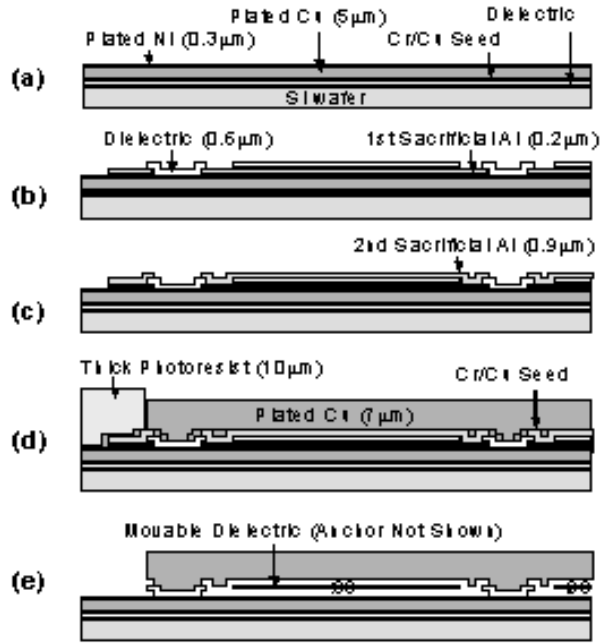


Fig. 62: Simplified fabrication process for the tunable-dielectric micromechanical capacitor.

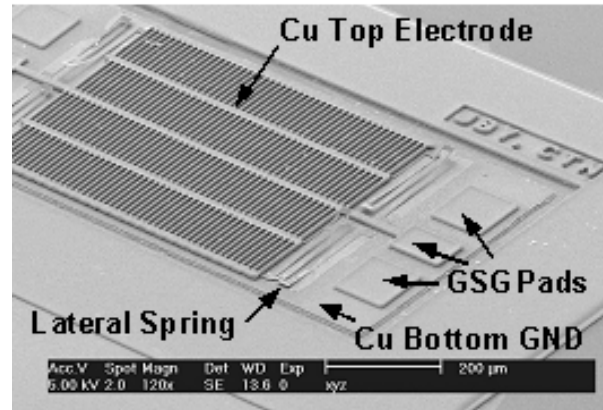


Fig. 63: SEM of a fabricated lateral spring movable-dielectric micromechanical capacitor.

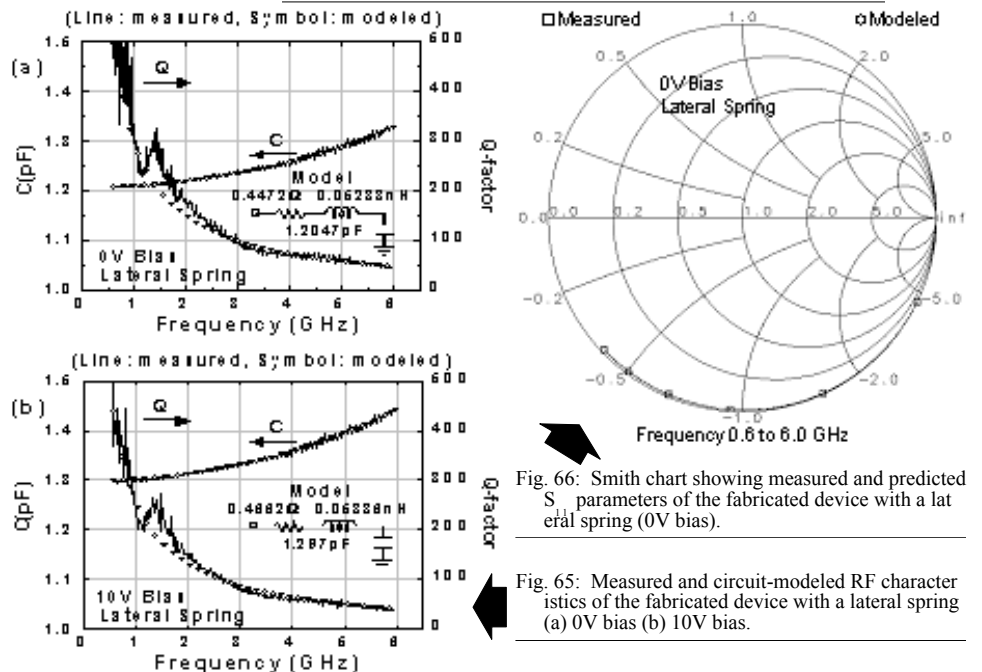


Fig. 66: Smith chart showing measured and predicted S_{11} parameters of the fabricated device with a lateral spring (0V bias).

Fig. 65: Measured and circuit-modeled RF characteristics of the fabricated device with a lateral spring (a) 0V bias (b) 10V bias.

tric when the two are engaged.

After etching vias through the Al to define top plate anchors (c.f., Fig. 62(c)), the top plate is formed by first evaporating a thin Cr/Cu seed layer, then electroplating Cu through a defining photoresist mold to a thickness of $7\mu\text{m}$ —thick enough to insure that the top plate does not bend under applied actuation voltages. Finally, the two Al sacrificial layers are selectively etched to release the dielectric structure using a $\text{K}_3\text{Fe}(\text{CN})_6/\text{NaOH}$ solution, which attacks Al, but leaves Cu and the nitride dielectric intact, yielding the final cross-section of Fig. 62(e). After release, a critical point dryer is often used to dry the structure to prevent stiction [39]. Since all of the process steps in this flow are done at $\leq 200^\circ\text{C}$, this process should be amenable to post-IC integration with transistor circuits.

To characterize device performance, RF measurements from 0.6 to 6GHz were made using an HP8753ES s-parameter network analyzer together with GSG-tipped Cascade Microtech microwave probes. Figures 65 and 66 present measured and modeled data summarizing the RF performance for the serpentine-spring device of Fig. 63, showing a very high Q of 291 at 1 GHz (1.21pF), with a tuning bias of 0V. Using the circuit model of Fig. 65 to extend its reactance plot, the expected SRF for this device is 19GHz.

Figure 64 plots the tuning range of the fabricated device, which is smaller than expected by theory when assuming lateral motion of the dielectric (i.e., motion parallel to the substrate). At first, the smaller tuning range was attributed to frictional dragging caused by the aforementioned film stress problem. However, closer inspection of partial devices with flat dielectric plates (deposited under more optimal PECVD conditions) revealed that due to a design oversight, vertical motion, rather than lateral, was actually easier to induce. In particular, the widths of the serpentine suspension beams ended up larger than their thicknesses due to stress-based PECVD limitations, making the vertical spring constant of a single serpentine suspension k_v , given by

$$k_v = \frac{1}{3}EW_l \left(\frac{t_l}{L_l} \right)^3 \quad (18)$$

more than 10 times smaller than its lateral spring constant. This, combined with the finite vertical electrostatic force that arises upon application of the actuation voltage V_a due to the asymmetrical dielectric-to-metal gaps above and below the dielectric plate (shown in Fig. 62(e)), makes vertical motion more likely than lateral. Future designs are planned to correct this.

In the meantime, although lateral motion was originally de-

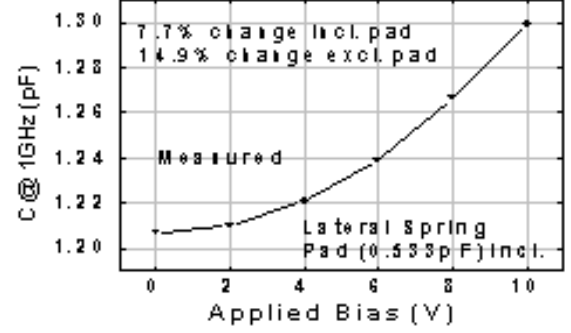


Fig. 64: Measured capacitance versus actuation voltage of the fabricated device with a lateral spring.

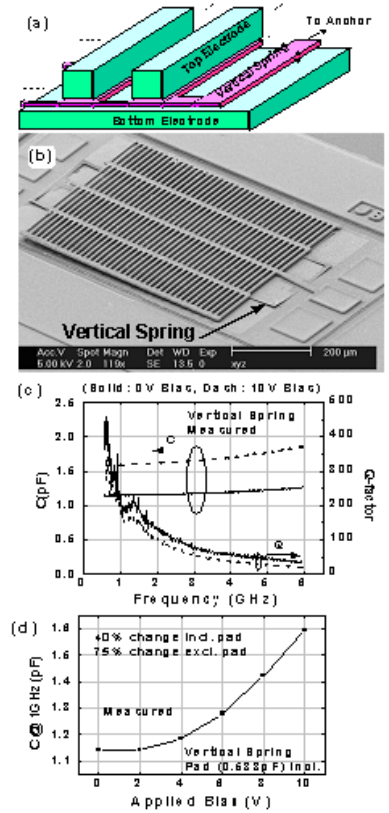


Fig. 67: A tunable capacitor with a vertical spring. (a) Device structure. (b) SEM photomicrograph of the fabricated device. (c) RF characteristic for both 0V and 10V bias voltage. (d) Measured tuning characteristic.

sired, Fig. 64 shows that vertical motion still offers a respectable amount of capacitance change due to fringing fields between the asymmetrical metal-to-dielectric gaps. The layout for the tunable capacitor fabrication run actually included devices specifically designed to move vertically, relying on only fringing fields to realize capacitance changes. Figure 67 shows the device structure, SEM, and measured RF performance for this vertically-designed device. In the design stage, this device was not expected to perform as well as the lateral version. However, this device actually benefited from film stress, so was able to achieve a much wider tuning range, approaching 40%, with a quality factor of 218 at 1 GHz.

Again, the Q 's measured for these movable-dielectric tunable μ mechanical capacitors are the highest reported for μ mechanical capacitors. Nevertheless, the Q 's attainable by vibrating micro-mechanical devices are still orders of magnitude higher than those posted by these tunable capacitors. Thus, given the importance of Q in determining the performance of communication applications, a vibrating micromechanical resonator will generally be a better resonator choice than an LC tank using a tunable capacitor for wireless applications—even the tunable capacitor of this work, which is one of the best available. It is for this reason that this grant focused mainly on vibrating micromechanical resonators and mechanical circuits made from them.

4.5. *Integrated MEMS/Transistor Merging Technologies*

The possibility of integration alongside integrated circuit transistors is among the most important potential benefits offered by vibrating RF MEMS technology. Given such a MEMS/transistor merging technology, the single-chip transceiver implementation depicted in Fig. 1 may soon become possible. When this grant began, technologies capable of integrating MEMS with IC transistors were already in existence [40]-[45]. However, each had their deficiencies for RF MEMS applications. For example, the BiMOSII process by Analog Devices [40] suffers from excessive capacitance in its MEMS-to-transistor interconnects, which are realized via diffused regions (with excessive diode capacitance to the substrate). Thus, although appropriate for low frequency accelerometer and gyroscope applications, BiMOSII is not suitable for high frequency RF MEMS applications. As another example, the MICS process [26], [42], [43], developed by the PI of this grant, is also deficient, in that although it greatly reduces capacitance in the MEMS-to-transistor interconnect, it does so using an unconventional tungsten metallization, so is not usable by the mainstream IC industry.

Pursuant to attaining a more practical method for merging RF MEMS and IC transistor technologies, this grant investigated three different approaches to integration: one based on bulk silicon MEMS, one using nickel as a micromechanical structural material, and one based on a bonded stamping technique.

4.5.1. *High Aspect-Ratio Gaps and a Merged Single-Crystal Si/CMOS Process*

A merged MEMS/transistor process technology [46] was demonstrated early in this grant that used an in-house BiCMOS process and a high aspect-ratio ECR/ICP etch technology to achieve sub-micron electrode-to-resonator gaps for lateral single-crystal silicon structures. This process technology actually resulted as part of an effort to investigate single-crystal silicon as a structural material for vibrating RF MEMS, with the main incentive being that single-crystal silicon was expected to exhibit a higher intrinsic Q and better aging stability than polysilicon. For the case of Q , single-crystal silicon resonators never achieved much higher Q than their polysilicon counterparts, mainly because anchor losses, not internal material losses, dominated the Q . In addition, single-crystal silicon was not pursued even for aging purposes, mainly due to the decreased flexi-

bility in arbitrarily positioning anchors for devices in single-crystal device processes. This decreased flexibility greatly restricted design freedoms for micromechanical filters, and as a result, polysilicon was preferred over single-crystal silicon for the work of this grant.

Nevertheless, a useful single-crystal silicon MEMS/transistor merging process was still demonstrated. An SEM showing a single-crystal μ mechanical resonator combined with BiCMOS transistors is presented in Fig. 68. The micromechanical resonator in the figure is $11\mu\text{m}$ -thick, $5\mu\text{m}$ -wide, and $500\mu\text{m}$ -long, with $3\mu\text{m}$ -wide comb fingers and $3\mu\text{m}$ -gaps between the fingers. Its resonance frequency was measured to be 28.9kHz —a conservative value, but necessary for this prototype process technology. The detection circuitry in Fig. 68 is transimpedance in nature, and utilizes a $3\mu\text{m}$ -gate length BiCMOS process, featuring two polysilicon layers for poly-to-poly capacitors and a single metal interconnect level.

The fabrication sequence used to attain the multi-technology system of Fig. 68 is summarized in Fig. 69. It begins with a selective, deep boron diffusion (Fig. 69(a) and (b)), the depth of which determines the thicknesses of the eventual micromechanical devices. Allowable thicknesses are limited by the maximum practical depth of a boron source diffusion, which is about

$15\mu\text{m}$ in our lab. After definition of boron diffused “micromechanical areas”, micromechanical processing is placed on hold, and conventional circuit processing proceeds as usual (Fig. 69(c)). Note that virtually any silicon-based circuit process can be used here, making this a generously modular process from a circuit perspective. Upon completion of circuits, a low-temperature oxide (LTO) is then blanket deposited (Fig. 69(d)) to serve as a passivation layer for the circuits, intended to protect them from subsequent micromechanical processing—in particular, from an impending ethylenediamine pyrocatechol (EDP) etch. After LTO deposition a nickel mask is then electroplated through a photoresist mold to serve as the etch mask during the dry etch that defines the resonator structure

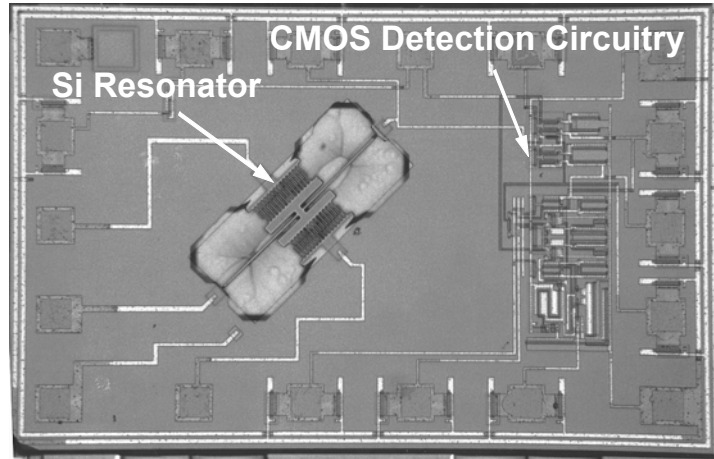


Fig. 68: 30 kHz micromechanical resonator integrated with BiCMOS detection circuitry.

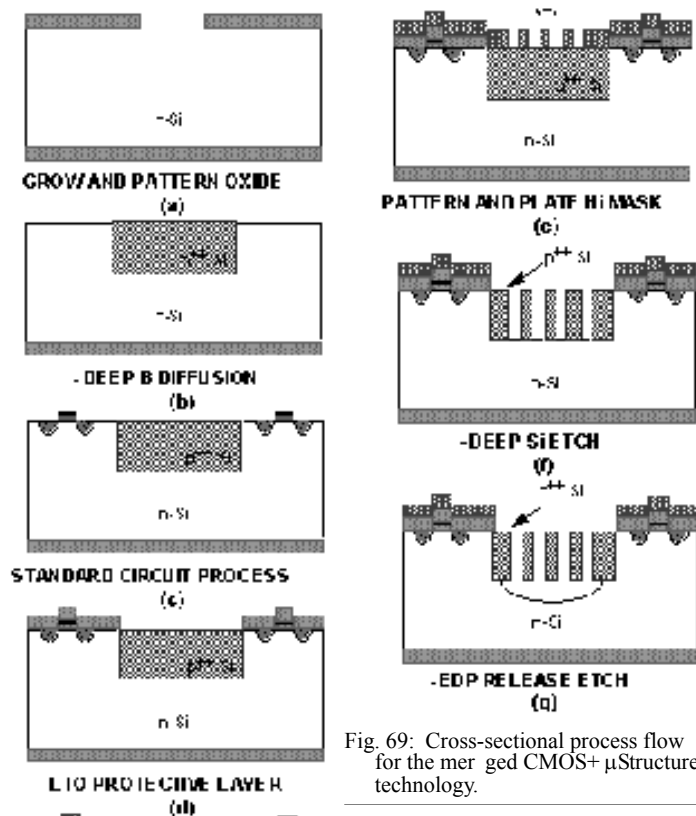


Fig. 69: Cross-sectional process flow for the merged CMOS+ μ Structures technology.

(Fig. 69(e)). This etch is performed via an inductively coupled high-density plasma (ICP) source using 250W of source power and 70W of stage power at 5 mTorr with 20 sccm of Cl_2 flow and a source-to-sample distance of 8 cm. With these process parameters, very high aspect-ratios in silicon are achievable, and the silicon is etched down through the boron diffused layer until undoped silicon is reached (Fig. 69(f)). Figure 70 presents an SEM showing 0.1 μm -gaps in 3.1 μm -thick, released single-crystal silicon cantilevers, patterned using the above technique. The cantilevers are 500 μm -long and 2 μm -wide, and were patterned using 80 W of ICP source power and 100 W of stage power at 1 mTorr, with 10 sccm of Cl_2 . Fig. 70 serves as clear evidence that sub-micron lateral gaps in relatively thick micromechanical structural material can be obtained through brute force sub-micron lithography and dry etching. (It should be noted that although e-beam lithography was utilized to define sub-micron lateral gaps in this work, Intel and other semiconductor manufacturers already have the ability to achieve 0.1 μm gaps via high throughput optical lithography.

After patterning devices, the whole wafer is then dipped in EDP, which selectively etches undoped silicon many times faster than boron doped silicon, and thus, undercuts and releases the boron-doped micromechanical structures (Fig. 69(g)). The nickel mask is removed in the last process step.

The functionality of MOS transistors achieved via this process has been verified via numerous measurements on HP4145B Semiconductor Parameter Analyzers. The results were shown in a previous Semi-Annual Report for this grant, so will not be repeated here in the interest of brevity.

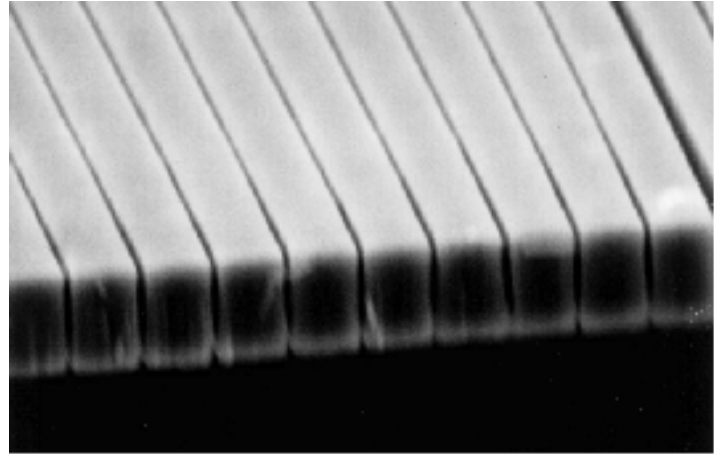


Fig. 70: SEM showing 0.1 μm -wide gaps between 2 μm -wide cantilever beams, etched in 3.1 μm -thick single-crystal silicon using a high-density ICP Cl_2 -etch.

4.5.2. *Nickel Micromechanical Resonators and Aging Studies*

Although modular to a degree, the above single-crystal MEMS/transistor merging technology was not completely modular, in that the MEMS process module had to be suspended and effectively interrupted by the transistor process module. In addition, as described above, the process did not provide adequate anchoring design flexibility for complex mechanical circuits, such as mechanical filters. Pursuant to attaining a more modular MEMS/transistor merging process similar to the MICS process [26], [42], [43], but without the high post-transistor temperatures that precluded the use of Al or Cu metallization in MICS, this grant turned next to nickel as a structural material for micromechanical resonators. In addition to being more amenable to low temperature integration directly above integrated circuit transistors, nickel also has the advantage of being more conductive, possibly making it more conducive to high power transmit filtering applications.

The work in this grant to explore nickel as a structural material has already been presented in Section 4.2.4 of this final report. Again, as explained in Section 4.2.4, the electroplated nickel

material used for this grant was found to have insufficient Q at VHF frequencies, and this was in large part the reason that nickel was discontinued as a structural material. Despite this, it is not the opinion of this PI that nickel can never be used as a high- Q resonator structural material. In fact, with appropriate alloying to slightly alter the electroplated nickel, there is probably still opportunity for nickel to yet play a role in vibrating resonator RF MEMS applications. However, the man power of this grant was better spent on more established materials, such as polysilicon and polydiamond.

4.5.3. Bonded-Microplatform MEMS/Transistor Merging Process

After demonstrating micromechanical resonators in polydiamond material, and given that a fully integrated transceiver using MEMS devices will most likely require a variety of structural materials (not just one), merging processes based on one structural material, such as MICS or any single-crystal silicon MEMS/transistor technology, clearly are not sufficient for a complete MEMS based transceiver. Thus, rather than continue to develop a fully planar merging process, this grant moved towards the ultimate in modularity: a bonding process that allows the modular combination of integrated circuit transistors and MEMS devices in a variety of technologies [48].

This bonded platform technology allows low-capacitance, “single-chip”, merging of MEMS and transistors with several key advantages: (1) It is truly modular, requiring no compromises in either the MEMS or transistor modules; (2) It attempts to minimize Q -degrading anchor losses experienced by previous bonding-based methods [47] by bonding *platforms* housing resonators, instead of directly bonding the anchors of resonators; and (3) It constitutes not only a wafer-scale batch approach, but also a repeatable approach, where a step-and-repeat procedure can be used to allow a single MEMS wafer to service several transistor wafers.

Figure 71 presents a scanning electron micrograph (SEM) of a completed μ platform housing a two-resonator, 40 MHz μ mechanical filter, just before bonding to a transistor wafer. In addition to the filter, the platform also includes several $30 \times 30 \mu\text{m}^2$ gold pads that serve as bonding sites to the transistor wafer. Some of these pads are strategically placed at corners of the platform to enhance stability during and after bonding, while others are located to serve as vertical interconnects between resonator electrodes and transistor electronics.

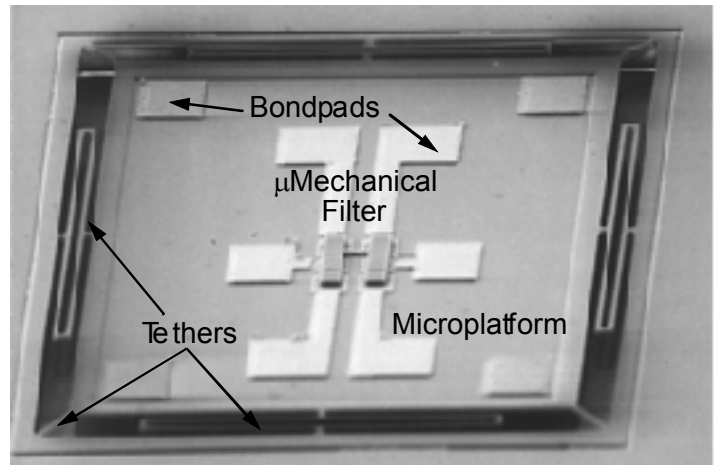


Fig. 71: SEM of a μ platform housing a 40 MHz, two-resonator CC-beam μ mechanical filter

As shown in Fig. 71, the μ platform is suspended by weak low stress nitride tethers to be broken after bonding to a transistor wafer by tearing away the MEMS wafer, leaving bonded μ platforms behind, in a procedure succinctly summarized in Fig. 72. This “tear away” approach borrows from the work of [47], and offers similar advantages in that a single MEMS wafer with platform/device repetitions can be used to service several transistor wafers—as many as there are repetitions. The economy of such an approach is obvious, especially for integrated MEMS/transistor systems where the transistor circuit dominates the die area.

The μ platform is realized using an SOI approach, where the silicon device layer of an SOI wafer defines the platform structure, and the buried oxide layer serves as a sacrificial layer, which is later removed to suspend the platform before bonding. The device layer in the SOI wafer is chosen to be 10-20 μ m-thick with the intent of maximizing the acoustic impedance of the eventual platform in order to minimize energy loss through the platform itself, and to minimize microphonic effects.

Figure 73 presents cross sections summarizing the μ platform process sequence. Here, a 5 μ m wide, 20 μ m deep trench is first etched around the platform area (defined by the isolation layer) using an STS deep RIE etcher (Fig. 73(a)). The trench is refilled with 2.5 μ m of low stress nitride to seal off the oxide in field areas from a future HF release step (Fig. 73(b)). The μ mechanical filter is then fabricated directly over the platform area using a conventional surface μ machining process [15] (Fig. 73(c)). Upon completion of μ mechanical filter processing, and before release, the nitride layer is patterned and dry-etched to delineate the platform and its supporting tethers. The μ platform structure and filters are then released using a combination of dry isotropic and wet etching techniques. The dry isotropic etch step removes the silicon under the nitride tethers, forming a trench opening that exposes the buried oxide. Figure 74 presents a cross-sectional SEM of the μ platform at this juncture. A surfactant-enriched HF solution (for better wetting along the sidewall of the opening) is then used to remove the sacrificial oxide under the platform, resulting in a suspended structure (Fig. 73(d)).

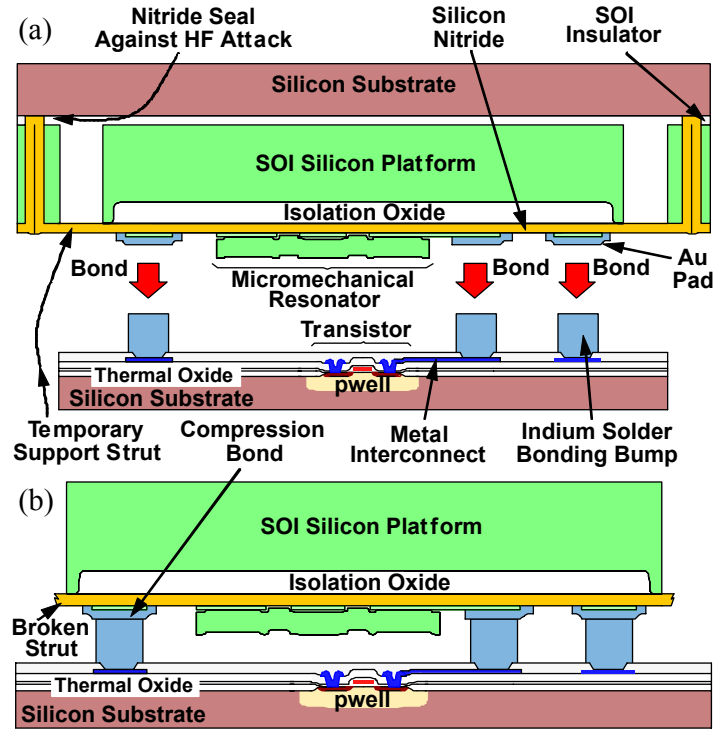


Fig. 72: Illustration of the procedure for achieving a combined MEMS/transistor chip via the described flip-bond-and-tear process. (a) Bonding. (b) Final cross-section.

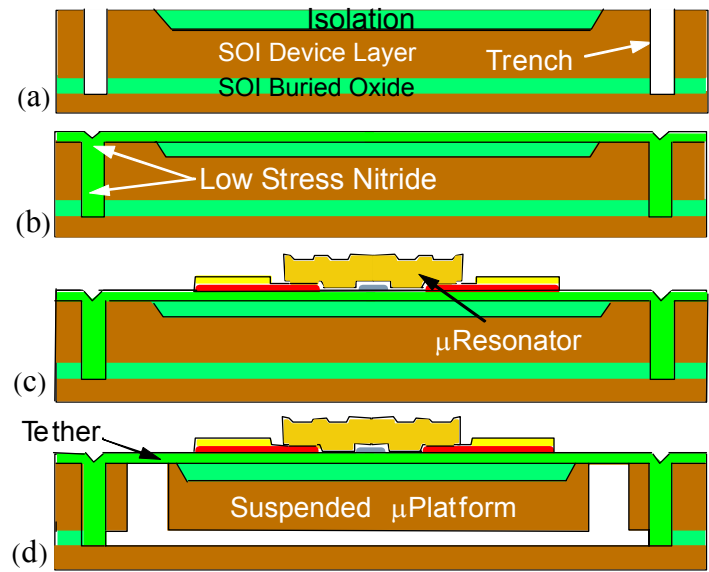


Fig. 73: Schematic showing cross-sections of the μ platform fabrication process flow.

Next, $7.5\mu\text{m}$ -thick, $30\times 30\mu\text{m}^2$ indium solder bumps are electroplated onto exposed bondpads on the BiCMOS wafer, which are located at sites corresponding to the gold electrode pads of the flipped $\mu\text{mechanical}$ filter. Figure 75 presents an SEM of the deposited solder bump posts, showing some deficiencies in their shapes, and indicating that additional work is needed to fully characterize this step. Bonding of $\mu\text{platforms}$ to the BiCMOS wafer is then done via an Electronic Visions aligner-bonder using a compressive force of 500N and a temperature of 175°C , which is needed to slightly reflow the solder bumps (Fig. 72(a)). The MEMS wafer is finally torn away from the BiCMOS wafer, breaking the tethers and leaving bonded $\mu\text{platforms}$ behind (Fig. 72(b)). Figure 76 presents top- and perspective-view SEMs of a $\mu\text{platform}$ bonded to BiCMOS circuits, with broken tethers clearly visible.

Of all the steps in the above process, the bonding of platforms to transistor circuit wafers proved to be the most difficult. This was due mainly to the poorly formed solder bumps (c.f., Fig. 75) mentioned above, but also due to cleanliness problems during bonding. In particular, before bonding, after flipping one wafer above the other, particulates were seen to drop onto the bottom wafer, seriously compromising the quality of the bonds. All tolled, the above problems led to less than 30% yield after bonding. Needless to say, further characterization of the bonding procedure is needed.

A custom-built vacuum chamber capable of achieving $50\mu\text{Torr}$ pressure was utilized to test $\mu\text{mechanical}$ resonators and filters housed by bonded platforms. The devices under test included a 40 MHz CC-beam $\mu\text{mechanical}$ resonator and a 38 MHz two-resonator filter, each with electrode-to-resonator gaps d_o of 350\AA ; and 6 MHz CC-beam resonator with a relatively large gap $d_o=1000\text{\AA}$. The 6 MHz device was included in testing, because it suffers less from anchor losses

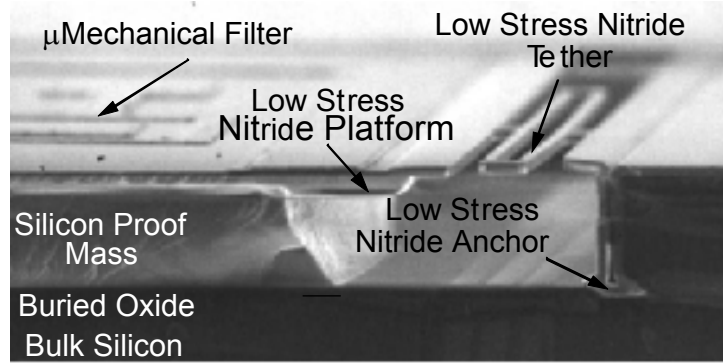


Fig. 74: SEM showing the cross-sectional view of the $\mu\text{platform}$.

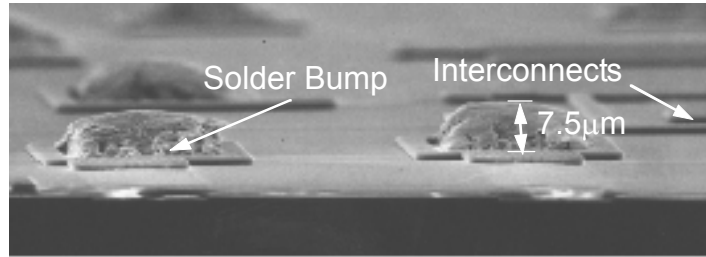


Fig. 75: SEM showing the solder bumps deposited on the BiCMOS wafer.

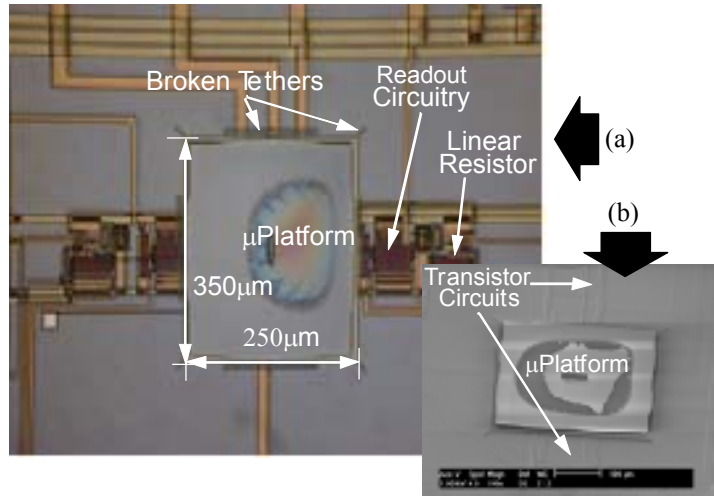


Fig. 76: A $\mu\text{mechanical}$ filter circuit showing both the transistor level electronics and the bonded platform: (a) Top view; (b) Perspective view.

than the others [18], and thus, could better serve as a vehicle for estimating the degree of Q degradation introduced by bonded-platform mounts.

Pursuant to exploring the effect of platform-mounting on device performance (especially, on Q), both bonded-platform-mounted devices and ones on unreleased platforms (still attached to the MEMS carrier wafer; i.e., substrate-mounted) were tested. Figures 76-80 present measured frequency spectra before and after platform-bonding for each of the aforementioned devices.

Before commenting on the observed “before and after” Q changes, some justification for the difference in Q between the various substrate-mounted test resonators is in order. Specifically, from the curves of Figs. 76 and 77, the Q of the substrate-mounted 6 MHz resonator is clearly much higher than that of its substrate-mounted 40 MHz counterpart. Although anchor losses, which are higher for the stiffer 40 MHz resonator, are partly responsible for this [18], it is actually Q -loading by parasitic interconnect series resistance R_s that dominates the difference in Q . In particular, although both devices “see” approximately the same load resistance $R_s \sim 150\Omega$, the 40 MHz device has a much smaller series motional resistance $R_x \sim 25\Omega$ than its 6 MHz counterpart ($R_x \sim 2.75k\Omega$), since its electrode-to-resonator gap spacing d_o is much smaller. (As detailed in [18], R_x goes as d_o^4 , so its value rolls off very quickly as d_o gets smaller.) Thus, the Q of the 40 MHz resonator is loaded more heavily by R_s , as predicted by expression for loaded Q

$$Q_L = Q \left[\frac{R_x}{R_x + R_s} \right] \quad (19)$$

where Q and Q_L are the intrinsic and loaded Q 's, respectively. As further testament to this loading-dominated Q -degradation mechanism, Fig. 78 presents measured spectra for two 9 MHz CC-beam resonators—one with $d_o=300\text{\AA}$, the other with $d_o=1000\text{\AA}$ —where the $Q=1,500$ for the larger-gapped device is clearly much higher than the $Q=150$ of its smaller-gapped counterpart.

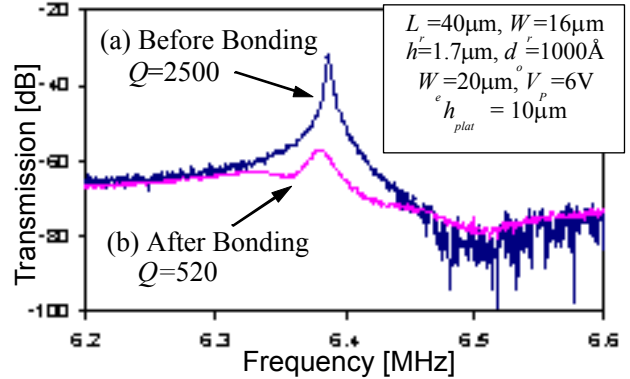


Fig. 76: Frequency response of a 6 MHz resonator (a) before bonding and (b) after bonding.

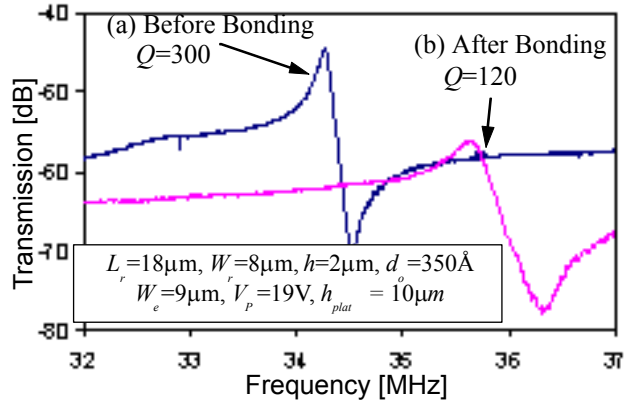


Fig. 77: Frequency response of a 40 MHz resonator (a) before bonding and (b) after bonding.

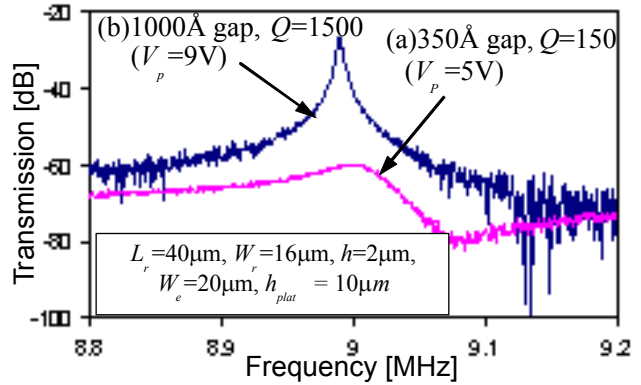


Fig. 78: Frequency response of a 9 MHz resonator with (a) 350Å gap (b) 1000Å gap.

Returning to our comparison of substrate- versus platform-mounted resonator performance, Fig. 76 reveals that the Q of the 6 MHz resonator drops from 2,500 for the substrate-mounted device, to only 520 after its platform is released and bonded to the transistor wafer. Figure 77 shows a similar effect for the 40 MHz resonator, where the Q drops from 300 to 120 after release and bonding of the platform mount. Needless to say, the observed Q loss is disappointing, and can tentatively be attributed to either or all of the following mechanisms:

- (1) Poor mechanical quality of the compression bonds. If these bonds are not perfectly rigid, they can be a source of losses in cases where energy is transferred from the resonator device, to the platform, to the substrate.
- (2) Insufficient platform rigidity. The 10 μm -thick platform may in fact not be thick enough to present an infinite acoustic impedance to a resonator. The farther from infinity the impedance, the greater the losses, and the lower the system Q .
- (3) Poor electrical quality of the compression bonds. In particular, bond deficiencies can raise the R_s by up to 5X, making Q -loading an issue for even medium-gapped resonators.
- (4) Insufficient cleanliness in the process. After bonding, the yield of working devices was substantially lower than before bonding. Given the well-known susceptibility of $\mu\text{mechanical}$ devices to contamination [49], this could easily be a source of Q degradation.

Design and fabrication adjustments are presently underway to remedy or investigate the above phenomena under the DARPA/MTO NMA SP Program, which will use this technology.

Figure 80 presents measured frequency characteristics for the 38 MHz two-resonator $\mu\text{mechanical}$ filter, before and after platform release and bonding. Again, significant performance degradation is observed after platform bonding, and not all of it can be attributed solely to Q -degradation. In particular, if Q -reduction were the only deficiency, then the same frequency characteristics would be expected in (a) and (b), with only an insertion loss difference between the two. Instead, distortion is seen in (b), possibly caused by a variety of phenomena, including platform-based capacitive/charging effects, or even contamination.

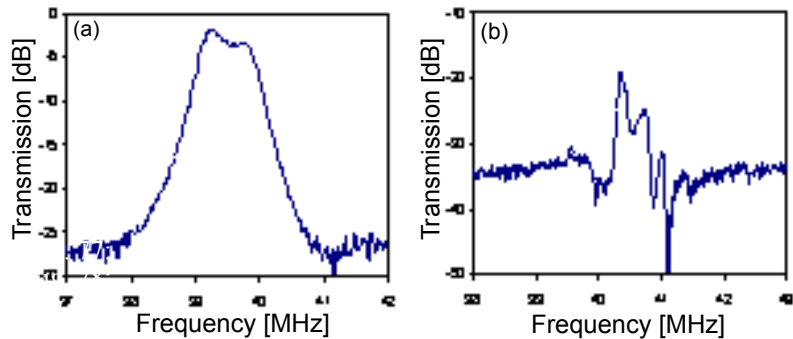


Fig. 80: Frequency response of a 40MHz filter (a) before bonding and (b) after bonding.

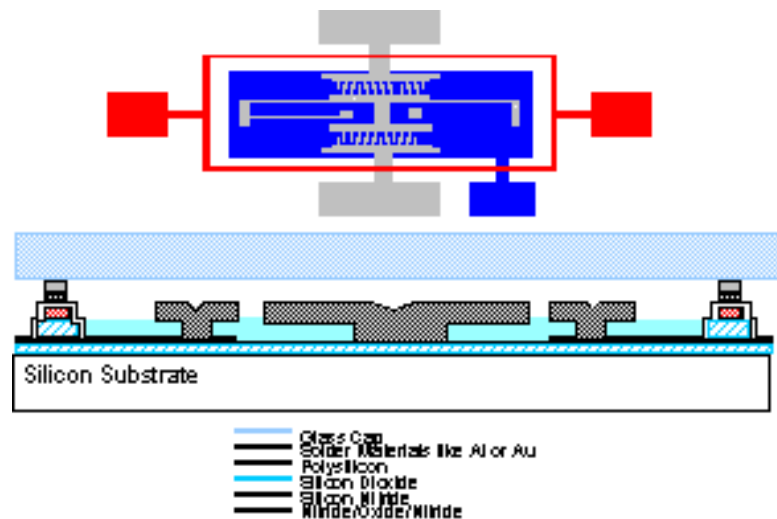


Fig. 81: Layout and cross-section for a $\mu\text{mechanical}$ resonator with overhead for encapsulation via solder-based localized heating.

4.5.4. Localized Heated Bonded Vacuum Encapsulation

Given that vacuum is required to attain high Q 's in VHF micromechanical resonators, and for protection against the environment, this grant also investigated vacuum-packaging methods. To be consistent with the bonding approach used for MEMS/transistor merging, and to take advantage of the localized annealing technique previously developed for trimming and Q -enhancement purposes (see Sections 4.2.3 and 4.2.4), a localized heating method for bonding vacuum encapsulating caps over micromechanical resonators—possibly resonators integrated with transistor electronics—was pursued, in which temperatures required to achieve hermetically sealed cap-to-substrate bonds are attained by locally heating at the bond areas, with minimal effect on surrounding devices, both electrical and micromechanical [50]. Over the course of this work, additional diagnostic runs have shown that locally melted solder or eutectic bonds can achieve seals as good or better than those achieved using locally heated silicon-glass(oxide) fusion bonding, with better reflow and coverage over interconnect lines running under the contact points of sealing caps.

At about midway through the grant, the efforts of this task were directed towards the implementation of a fully vacuum-encapsulated folded-beam micromechanical resonator using a solder-bonded cap as described above. Figure 81 presents the layout for the intended device and its cross-section immediately before localized heated bonding. As shown, the bonding structure consists of a doped polysilicon resistor encased under films of oxide and nitride dielectrics that electrically isolate it from a thick block of indium solder patterned directly above it. A (glass) sealing cap is placed on top of this structure immediately before bonding. To activate the bonding process, currents are sent through the polysilicon resistor, heating it and the indium solder to temperatures exceeding the melting point of indium. The indium then melts and wets the surfaces of both the silicon wafer and the glass sealing cap, reflowing to cover any topographies, such as those presented by interconnect to and from the device to be encapsulated.

Figure 82 presents the detailed process flow used to achieve both the resonator and bonding layers. The process begins with the deposition of oxide and nitride isolation layers normally used in conventional polysilicon surface micro-machining technologies. Next, interconnect polysilicon is deposited, patterned, and doped, again, as in conventional surface-

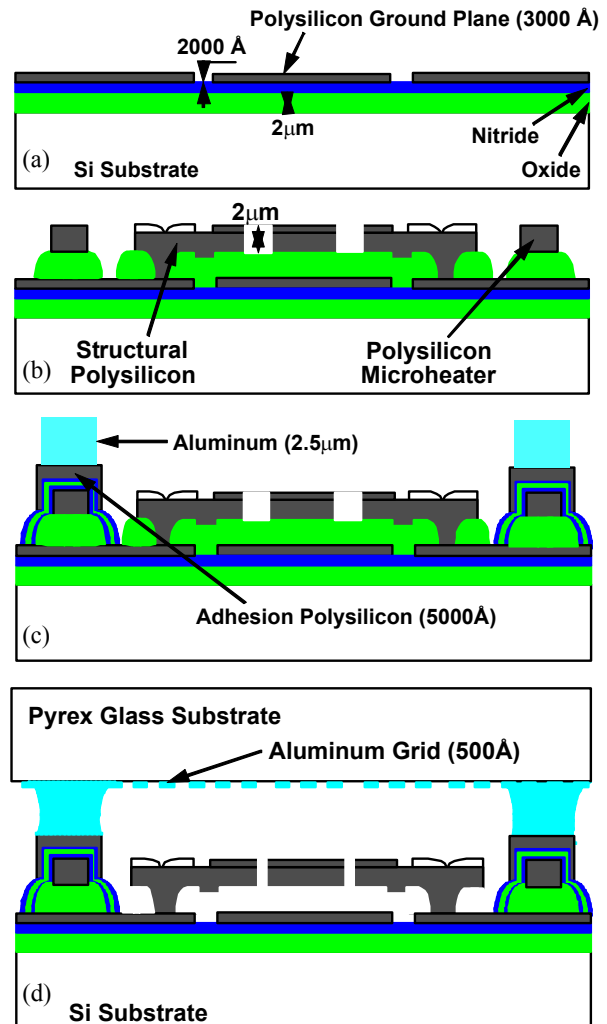


Fig. 82: Process flow for wafer-level vacuum encapsulation of micromechanical resonators via localized heated bonding.

micromachining, leaving the cross-section of Fig. 82(a). A 2 μm -thick layer of sacrificial oxide is then deposited and patterned to form anchor openings for the eventual resonators. Next, a 2 μm -thick film of structural polysilicon is deposited, patterned, and implant-doped to form both resonator geometries and localized heater runners to be used later for localized solder bonding. Once the polysilicon has been removed over field areas, the sacrificial oxide is patterned a second time to form mesas underneath the heater runners that now define the eventual vacuum cap sealing boundary. At this point, the cross-section is as shown in Fig. 82(b). Nitride/oxide/nitride isolation are then deposited and patterned over the boundary mesas. Next, a film of polysilicon is deposited, doped, and patterned over the boundary mesas to serve as an adhesion layer for the aluminum solder, which is deposited and patterned over the boundary mesas, yielding the cross-section of Fig. 82(c). Bonding then proceeds as already described above to yield the final cross-section shown in Fig. 82(d).

Over the past half-year, this process was run, and after solving a minor problem with the conductivity of the heater polysilicon layer, encapsulated resonators were achieved. Figure 82 presents a micromechanical resonator with glass sealing cap forcefully removed. The fact that the cap itself broke before the bond did indicates that the bond is indeed very strong. At present, however, the encapsulated resonators are not testable, since they are in fact stuck down under the shells, as can be seen in Fig. 82, where the folding truss on the right-hand side is visibly stuck to the substrate. This problem has now been solved using a supercritical CO_2 release technique, and testable vacuum-encapsulated resonators have finally been achieved.

Figure 83 presents the measured frequency characteristic for a folded-beam polysilicon $\mu\text{mechanical}$ resonator encapsulated via the above process. Although the Q of 2,500 is lower than that seen in previous such resonators, it is still a Q indicative of a vacuum environment under the glass cap. In addition, further measurements for resonators in this process under a controlled vacuum environment indicate that the low Q is

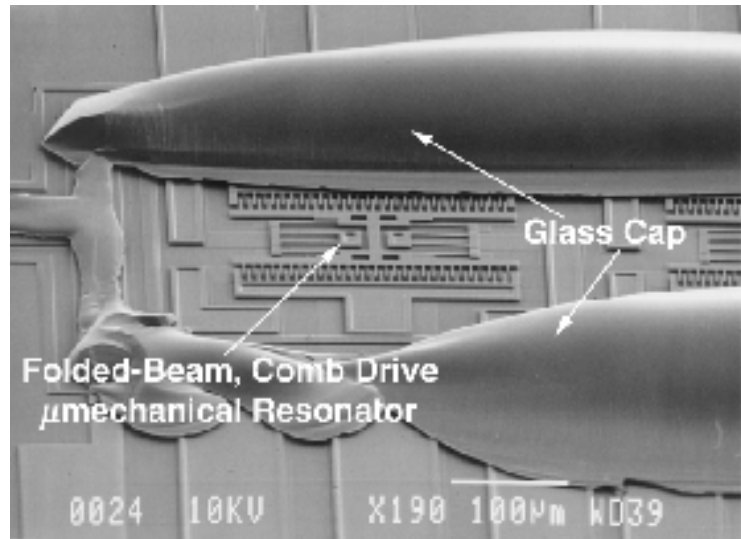


Fig. 82: SEM of a previously encapsulated micromechanical resonator with glass cap forcibly removed (i.e., broken).

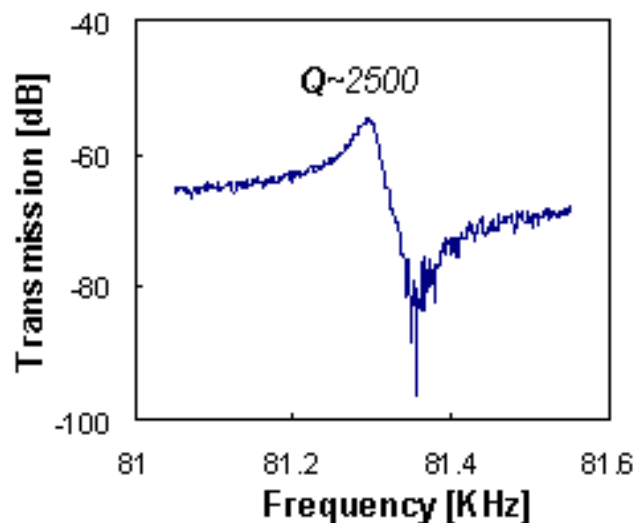


Fig. 83: Measured frequency characteristic for a polysilicon folded-beam $\mu\text{mechanical}$ resonator vacuum encapsulated using the localized heated bonding technique of Fig. 81.

actually caused by material deficiencies, rather than by insufficient pressure. In particular, due to an oversight, the micromechanical resonators in this process were not properly annealed. Thus, the polysilicon material did not benefit from the structural reorganization afforded by the standard annealing process, and these resonators show about an order of magnitude lower Q than annealed counterparts at the same pressure. Measurements of Q versus pressure for these resonators show that the observed $Q=2,500$ corresponds to a vacuum under the glass cap of about 25 mTorr.

Figure 84 presents a plot of pressure versus time, showing that this localized heated encapsulation process is capable of holding a vacuum of ~ 25 mTorr for more than 10 weeks. (Actually, Fig. 84 is a very old plot. At the time of this writing, this vacuum level has actually held for more than 1.5 years now.) Successful demonstration of vacuum encapsulation now makes possible controlled experiments to evaluate the stability and reliability of μ mechanical resonator devices. Such experiments are planned in future research.

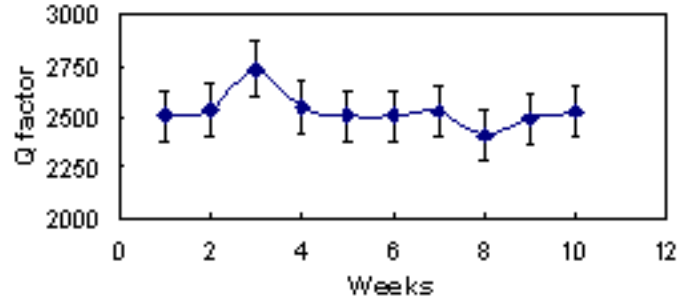


Fig. 84: Plot of pressure versus time for a vacuum encapsulated resonator such as shown in Fig. 83.

[For completeness, it should be noted that this localized-heated vacuum encapsulation work was started and finished under funding supplied by this grant (and only this grant), and the student doing this work graduated with a Ph.D. from the University of Michigan as a student of Prof. Khalil Najafi. The reason for stating this is that this work was later transitioned to another grant (PI'ed by Prof. Ken Wise, but actually lead by Prof. Liwei Lin), and it is my understanding that Lin had also been using this vacuum encapsulation work to push his grant, which is fine, but which is technically not true, since this work was actually supported entirely by this grant.]

5.0 SUMMARY

The efforts over the four years of this grant have pioneered the field of vibrating RF MEMS and have yielded potentially revolutionary advancements towards wireless transceivers with substantially smaller size and greatly enhanced performance. Among the successfully demonstrated research prototype vibrating RF MEMS devices that fill requirements specified by the MEMS-based transceiver of Fig. 1 are:

- (1) Micromechanical IF and RF filters constructed of micro-scale resonators with higher Q than any other room temperature on-chip (or even off-chip) resonator in their frequency range, and thus, capable of insertion loss performance many times better than presently available and in sizes orders of magnitude smaller. These devices are also on/off switchable via their dc-bias voltages, and thus, do not require diode or micromechanical switches in the signal path for switching—a major advantage that eliminates the insertion loss of other tunable filter approaches that use switches in their signal paths.
- (2) Micromechanical resonator oscillators with thermal stability on par with quartz crystal oscillators and using resonators with Q 's capable of achieving extremely low phase noise performance.

- (3) Micromechanical mixer-filter (dubbed “mixler”) devices capable of mixing, bandpass filtering, and parametric amplification in a single, passive, micromechanical device. This single device replaces three different components in a super-heterodyne or wideband IF communications receiver architecture. In recognition of the novelty and potentially far-reaching impact of micromechanical mixer-filters, the 1998 IEEE Int. Electron Devices Meeting (IEDM’98) awarded the paper describing mixer-filters the Roger A. Haken Best Student Paper Award that year.

Provided they can operate at the desired frequencies and within the desired linearity and power handling specifications, the above devices together can satisfy virtually all off-chip, high- Q functions needed in super-heterodyne or zero-IF receivers. In particular, all shaded components in Fig. 1 can be replaced via the above set of vibrating RF MEMS devices, and with substantially better insertion loss performance than achievable via other on-chip technologies, including RF MEMS technologies, such as switches, tunable capacitors, or MEMS-based inductors. To put it bluntly, provided the right frequencies and power handling performances can be achieved, the results of this grant serve to further bolster the opinion that “the only MEMS technology that need be added to IC transistor technology to achieve multi-band, robust, ultra-low-power, miniaturized wireless receivers is vibrating RF MEMS technology.”

Still, although its findings and demonstrations do provide some testament for the above statement, this grant alone has not proven the statement true. Nor could it possibly do this within the time allotted. Rather, as indicated in the body of this report, there is much work left to do even at the component level, before vibrating RF MEMS technology can achieve its true potential. Among unfinished items are:

- (1) Demonstration of micromechanical resonators operating beyond UHF.
- (2) Demonstration of micromechanical filters with sufficient linearity and power handling ability to process high power transmit signals. In particular, the majority of the devices demonstrated via this grant are appropriate for receive path applications, but not for transmit path applications (near the antenna), where high power handling is generally needed for military (and even commercial) applications. In this regard, larger devices, or arrays of many vibrating micromechanical devices will likely be required to process high power signals.
- (3) Demonstration of micromechanical filters with sufficiently low impedances so as to allow proper impedance matching to antennas without the need for sizable matching networks. Again, larger devices or arrays of devices are likely needed for this.
- (4) Demonstration of micromechanical resonator oscillators with adequate power output (the reader should be noticing a theme developing here), and without the $1/f^3$ phase noise component observed in the oscillators demonstrated via this grant. Again, as detailed in the report body, a model has been defined for the mechanism behind the extra noise, so solutions to this problem exist, but work is needed to implement them. In addition, much higher frequency oscillators and micromechanical resonator VCO’s should be pursued in future work to enhance transceiver functionality in both military and commercial applications.
- (5) Demonstration of an automatic frequency trimming technique to allow the use of mechanical circuits containing hundreds of micromechanical resonators, such as the arrays described above.
- (6) Demonstration of technologies that not only merge micromechanical resonators and integrated circuit transistors together, but also vacuum-encapsulate the micromechanical devices to allow high- Q operation, and to protect them from environmental contaminants.

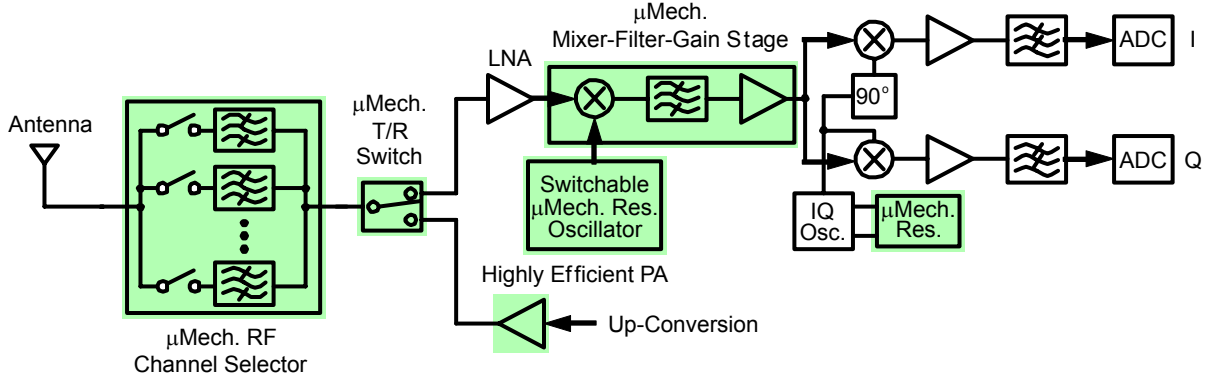


Fig. 85: System block diagram for an RF channel-select receiver architecture utilizing large numbers of micromechanical resonators in banks to trade Q for power consumption. (On-chip μ mechanics are shaded.)

Again, the above is merely a subset of numerous remaining issues, some of which can only be revealed or appreciated when considering the future of vibrating RF MEMS technology—a future that should go well beyond anything yet mentioned in the reports associated with this grant and that may well make possible paradigm-shifts in transceiver architectures with equally revolutionary impact on transceiver performance.

In particular, the MEMS-usage strategy depicted in Fig. 1 amounts to direct replacement of off-chip components in an existing transceiver architecture. While beneficial, and actually capable of attaining (through sheer better insertion loss performance) receiver noise figure reductions from 9 dB to 3 dB, the performance gains afforded by mere direct replacement by MEMS are quite limited when compared to more aggressive uses of MEMS technology. To fully harness the advantages of μ mechanical circuits, one must first recognize that due to their micro-scale size and zero dc power consumption, μ mechanical circuits offer the same system complexity advantages over off-chip discrete components that planar IC circuits offer over discrete transistor circuits, except in the mechanical signal processor domain. Thus, as with transistor circuits, μ mechanical circuits should be utilized in large numbers to maximize performance gains.

Figure 85 presents the system-level block diagram for a possible transceiver front-end architecture that takes full advantage of the complexity achievable via μ mechanical circuits [51], [52], [53]. The main driving force behind this architecture is power reduction, attained in several of the blocks by replacing active components by low-loss passive μ mechanical ones, and by trading power for high selectivity (i.e., high- Q). Among the key performance enhancing features are: (1) an RF channel selector comprised of a bank of switchable μ mechanical filters, offering multi-band reconfigurability, receive power savings via relaxed dynamic range requirements [13], and transmit power savings by allowing the use of a more efficient power amplifier; (2) use of a passive μ mechanical mixer-filter to replace the active mixer normally used, with obvious power savings; (3) a VCO referenced to a switchable bank of μ mechanical resonators, capable of operating without the need for locking to a lower frequency reference, hence, with orders of magnitude lower power consumption than present-day synthesizers; (4) use of a μ mechanical T/R switch, with already described power savings in transmit-mode; and (5) use of μ mechanical resonator and switch components around the power amplifier to enhance its efficiency.

Although already quite aggressive, the architecture of Fig. 85 may still not represent the best power savings afforded by MEMS. In fact, even more power savings than in Fig. 85 are possible if the high- Q μ mechanical circuits in the signal path can post such low losses that the RF LNA (normally required to boost the received signal against losses and noise from subsequent stages) may in fact no longer be needed. Rather, the RF LNA can be removed, and the needed gain to baseband provided instead by an IF LNA that consumes much less power since it operates at the much lower IF frequency. Without the RF LNA or transistor mixer, the receiver front-end architecture reduces to an all-MEMS topology, such as shown in Fig. 86. Here, since the absence of RF transistor circuits removes dynamic range concerns, the channel-selecting filter bank of Fig. 85 has been converted to a mixer-filter bank and moved down to the IF frequency, where it might be easier to implement, and where it allows the use of a single-frequency RF local oscillator (LO) to down-convert from RF to IF. Since the RF LO is now a single frequency oscillator, power hungry phase-locking and pre-scaling electronics are not needed, allowing similar power advantages as for the VCO in the architecture of Fig. 85. In fact, the architecture of Fig. 86 attains all the power advantages of that of Fig. 85, plus additional power savings due to the lack of an LNA. It, however, does so at the cost of a slightly higher overall noise figure and decreased robustness against hostile (i.e., jamming) interferers.

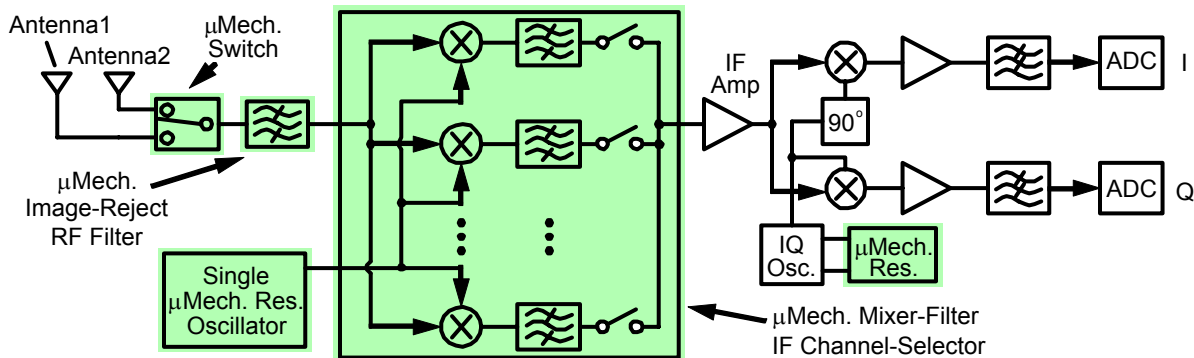


Fig. 86: System block diagram for an all-MEMS receiver front-end, employing an RF image-reject filter, a fixed μ mechanical resonator local oscillator, and a switchable array of IF μ mechanical mixer-filters.

If the above architectures seem unbelievable, requiring too many far-reaching advancements in the state of the art, then consider that this is exactly the state of affairs that existed four years ago when this very grant was started. In particular, as mentioned in the first paragraph of this report, four years ago the wireless integrated circuits community was focused on methods for attaining alternative communication architectures that eliminate off-chip high- Q passive filters and resonators, and in the process had embraced direct-conversion architectural techniques as the only sensible way to achieve anything close to single-chip transceivers. As such, vibrating RF MEMS technology was not considered a plausible direction, and it was even scoffed at by the field as “never being able to reach 20 MHz” and as “too expensive to implement versus an all-transistor solution.”

Needless to say, at the present time, vibrating RF MEMS has reached well beyond 20 MHz, with the 200 MHz demonstration of this work representing a three order of magnitude increase in frequency from the start of this grant. In addition, at least to date, it seems that all-transistor solutions to wireless transceivers will not be able to implement single-chip transceivers, having only eliminated one IF filter of all the passives needed in a super-heterodyne transceiver in all this time. As a result, in a reversal of opinion from four years ago, the wireless community now

seems to be embracing MEMS technology as the most promising method for achieving smaller, better performing transceivers, and all this in no small way due to the results, numerous papers, and invited presentations supported by this grant.

In the wake of this grant, the premise that high- Q components could not be miniaturized that existed before the start of this grant no longer governs wireless thinking. In fact, at the recent 2002 Int. Solid-State Circuits Conference (ISSCC'02), it seems that MEMS has now been accepted by those who originally doubted the technology as a solution for both miniaturization and performance enhancement of wireless transceivers. Even more concrete examples of the influence and impact of this grant include:

- (1) The new DARPA/MTO NMAPS Program, which further develops the technologies pioneered by this grant, specifically investigating arrays of micromechanical resonator devices for communication transceivers.
- (2) Numerous industrial companies are now pursuing vibrating RF MEMS, including Motorola, Intel, IBM, and Agere. In addition, a start-up company called Discera has been formed by the PI of this grant, bent on developing products based upon the vibrating RF MEMS technology researched under this grant. RF MEMS is now considered one of the most lucrative areas for business development by venture capitalists across the U.S.
- (3) Vibrating RF MEMS are now being researched and developed worldwide, in Europe and in Asia, by companies such as Nokia, ST Microelectronics, Sony, and Samsung.

It should be mentioned that none of the above successes were possible if it not for open-minded thinking by DARPA, and in particular by the DARPA/ETO MEMS Program Manager at the beginning of this grant, Ken Gabriel, and those who followed, Al Pisano and Bill Tang, who despite the prevailing, opposing opinions at the time by the majority of the wireless community, had the vision and insight to support and continue to support the vibrating RF MEMS ideas in the original proposal, and now beyond via the NMAPS Program.

And finally, in closing, the work made possible by this grant has greatly extended the state of the art in micromechanical resonator technology, and has elevated this technology to a position where it stands to revolutionize not only the size, but also the architectures and outright performances (e.g., battery lifetime, robustness) of wireless communication devices. It is gratifying to know that although this particular grant is ending, this type of work will not end. In fact, work on vibrating RF MEMS should actually expand, especially given subsequent programs like NMAPS, which should be instrumental in bringing about the revolution expected of micromechanical resonator technology.

References:

- [1] H. Khorramabadi and P. R. Gray, "High-frequency CMOS continuous-time filters," *IEEE J. Solid-State Circuits*, vol. SC-19, No. 6, pp. 939-948, Dec. 1984.
- [2] B.-S. Song and P. R. Gray, "Switched-capacitor high- Q bandpass filters for IF applications," *IEEE J. Solid-State Circuits*, vol. SC-21, No. 6, pp. 924-933, Dec. 1986.
- [3] A. A. Abidi, "Direct-conversion radio transceivers for digital communications," *IEEE J. Solid-State Circuits*, vol. 30, No. 12, pp. 1399-1410, Dec. 1995.
- [4] W. C. Tang, T.-C. H. Nguyen, and R. T. Howe, "Laterally driven polysilicon resonant microstructures," *Sensors and Actuators*, **20**, 25-32, 1989.

- [5] C. T.-C. Nguyen and R. T. Howe, "Quality factor control for micromechanical resonators," *Technical Digest*, IEEE International Electron Devices Meeting, San Francisco, California, December 14-16, 1992, pp. 505-508.
- [6] C. T.-C. Nguyen and R. T. Howe, "Microresonator frequency control and stabilization using an integrated micro oven," *Digest of Technical Papers*, the 7th International Conference on Solid-State Sensors and Actuators (Transducers'93), Yokohama, Japan, pp. 1040-1043, June 7-10, 1993.
- [7] J. D. Cressler, *et al.*, "Silicon-germanium heterojunction bipolar technology: the next leap for silicon?" *Digest of Technical Papers*, 1994 ISSCC, San Francisco, CA, February, 1994.
- [8] J. C. Rudell, J. A. Weldon, J. J. Ou, L. Lin, P. Gray, "An Integrated GSM/DECT Receiver: Design Specifications", *UCB Electronics Research Laboratory Memorandum*, Berkeley.
- [9] N. Slawsby, "Frequency control requirements of radar," *Proceedings of the 1994 IEEE International Frequency Control Symposium*, June 1-3, 1994, pp. 633-640.
- [10] W. P. Robins, *Phase Noise in Signal Sources*. London: Peter Peregrinus, Ltd., 1982.
- [11] D. B. Leeson, "A simple model of feedback oscillator noise spectrum," *Proc. IEEE*, vol. 54, pp. 329-330, Feb. 1966.
- [12] C. T.-C. Nguyen, "Micromechanical resonators for oscillators and filters (invited)," *Proceedings*, 1995 IEEE International Ultrasonics Symposium, Seattle, WA, Nov. 7-10, 1995, pp. 489-499.
- [13] C. T.-C. Nguyen, "Frequency-selective MEMS for miniaturized low-power communication devices (invited)," *IEEE Trans. Microwave Theory Tech.*, vol. 47, no. 8, pp. 1486-1503, Aug. 1999.
- [14] K. Wang and C. T.-C. Nguyen, "High-order medium frequency micromechanical electronic filters," *IEEE/ASME J. Microelectromech. Syst.*, vol. 8, no. 4, pp. 534-557, Dec. 1999.
- [15] F. D. Bannon III, J. R. Clark, and C. T.-C. Nguyen, "High frequency micromechanical filters," *IEEE J. Solid-State Circuits*, vol. 35, no. 4, pp. 512-526, April 2000.
- [16] A. I. Zverev, *Handbook of Filter Synthesis*. New York: John Wiley & Sons, 1967.
- [17] R. Navid, J. R. Clark, M. Demirci, and C. T.-C. Nguyen, "Third-order intermodulation distortion in capacitively-driven CC-beam micromechanical resonators," *Technical Digest*, 14th Int. IEEE Micro Electro Mechanical Systems Conference, Interlaken, Switzerland, Jan. 21-25, 2001, pp. 228-231.
- [18] K. Wang, A.-C. Wong, and C. T.-C. Nguyen, "VHF free-free beam high- Q micromechanical resonators," *IEEE/ASME J. Microelectromech. Syst.*, vol. 9, no. 3, pp. 347-360, Sept. 2000.
- [19] J. R. Vig and Y. Kim, "Noise in microelectromechanical system resonators," *IEEE Trans. Ultrason. Ferroelec. Freq. Contr.*, vol. 46, no. 6, pp. 1558-1565, Nov. 1999.
- [20] J. R. Clark, W.-T. Hsu, and C. T.-C. Nguyen, "High- Q VHF micromechanical contour-mode disk resonators," *Technical Digest*, IEEE Int. Electron Devices Meeting, San Francisco, California, Dec. 11-13, 2000, pp. 399-402.

- [21] J. Wang, J. E. Butler, D. S. Y. Hsu, and C. T.-C. Nguyen, "CVD polycrystalline diamond high- Q micromechanical resonators" *Tech. Digest*, 2002 IEEE Int. Micro Electro Mechanical Systems Conf., Las Vegas, Jan. 20-24, 2002, pp. 657-650.
- [22] *Diamond and Related Materials*, 3, pp. 160-162 (1993).
- [23] W.-T. Hsu, J. R. Clark, and C. T.-C. Nguyen, "A sub-micron capacitive gap process for multiple-metal-electrode lateral micromechanical resonators," *Technical Digest*, 14th Int. IEEE Micro Electro Mechanical Systems Conference, Interlaken, Switzerland, Jan. 21-25, 2001, pp. 349-352.
- [24] W. -T. Hsu, J. R. Clark, and C. T. -C. Nguyen, " Q -optimized lateral free-free beam micro-mechanical resonators," *Digest of Technical Papers*, the 11th Int. Conf. on Solid-State Sensors & Actuators (Transducers'01), Munich, Germany, June 10-14, 2001, pp. 1110-1113.
- [25] D. M. Aslam and D. Schulz, "Technology of Diamond Microelectromechanical Systems," *Technical Digest*, 8th Int. Conf. on Solid-State Sensor & Actuators, Stockholm (Sweden), Vol. 2, 222-224 (1995).
- [26] C. T.-C. Nguyen and R. T. Howe, "An integrated CMOS micromechanical resonator high- Q oscillator," *IEEE J. Solid-State Circuits*, vol. 34, no. 4, pp. 440-455, April 1999.
- [27] W.-T. Hsu, S. Lee, and C. T.-C. Nguyen, "*In situ* localized annealing for contamination resistance and enhanced stability in nickel micromechanical resonators," *Digest of Technical Papers*, 10th International Conference on Solid-State Sensors and Actuators, Sendai, Japan, June 7-10, 1999, pp. 932-935.
- [28] S. Lee, M. U. Demirci, and Clark T.-C. Nguyen, "A 10-MHz micromechanical resonator Pierce reference oscillator for communications," *Digest of Technical Papers*, the 11th Int. Conf. on Solid-State Sensors & Actuators (Transducers'01), Munich, Germany, June 10-14, 2001, pp. 1094-1097.
- [29] J. Cao and C. T.-C. Nguyen, "Drive amplitude dependence of micromechanical resonator series motional resistance," *Digest of Technical Papers*, 10th Int. Conf. on Solid-State Sensors and Actuators, Sendai, Japan, June 7-10, 1999, pp. 1826-1829.
- [30] W.-T. Hsu, J. R. Clark, and C. T.-C. Nguyen, "Mechanically temperature compensated flexural-mode micromechanical resonators," *Technical Digest*, IEEE Int. Electron Devices Meeting, San Francisco, California, Dec. 11-13, 2000, pp. 493-496.
- [31] W. -T. Hsu and C. T. -C. Nguyen, "Stiffness-compensated temperature-insensitive micro-mechanical resonators," *Tech. Digest*, 2002 IEEE Int. Micro Electro Mechanical Systems Conf., Las Vegas, Nevada, Jan. 20-24, 2002, pp. 731-734.
- [32] K. Wang, A.-C. Wong, W.-T. Hsu, and C. T.-C. Nguyen, "Frequency-trimming and Q -factor enhancement of micromechanical resonators via localized filament annealing," *Digest of Technical Papers*, 1997 International Conference on Solid-State Sensors and Actuators, Chicago, Illinois, June 16-19, 1997, pp. 109-112.
- [33] R. A. Johnson, *Mechanical Filters in Electronics*, New York: John Wiley & Sons, 1983.
- [34] A.-C. Wong, H. Ding, and C. T.-C. Nguyen, "Micromechanical mixer+filters," *Technical Digest*, IEEE Int. Electron Devices Meeting, San Francisco, California, Dec. 6-9, 1998, pp. 471-474.

- [35] J.-B. Yoon and C. T.-C. Nguyen, "A high- Q tunable micromechanical capacitor with movable dielectric for RF applications," *Technical Digest*, IEEE Int. Electron Devices Meeting, San Francisco, California, Dec. 11-13, 2000, pp. 489-492.
- [36] J. R. Clark, A.-C. Wong, and C. T.-C. Nguyen, "Parallel-resonator HF Micromechanical Bandpass Filters," *Digest of Technical Papers*, 1997 International Conference on Solid-State Sensors and Actuators, Chicago, Illinois, June 16-19, 1997, pp. 1161-1164.
- [37] D. J. Young and B. E. Boser, "A micromachined variable capacitor for monolithic low-noise VCO's," *Tech. Digest*, 1996 Solid-State Sensor and Actuator Workshop, pp. 86-89, June 1996.
- [38] A. Dec and K. Suyama, "Micromachined electro-mechanically tunable capacitors and their applications to RF IC's," *IEEE Trans. Microwave Theory Tech.*, vol. 46, pp. 2587-2596, Dec. 1998.
- [39] G. T. Mulhern, *et al.*, "Supercritical carbon dioxide drying of microstructures," *Proceedings*, Transducers'93, pp. 296-299, June 1993.
- [40] T. A. Core, W. K. Tsang, S. J. Sherman, "Fabrication technology for an integrated surface-micromachined sensor," *Solid State Technology*, pp. 39-47, Oct. 1993.
- [41] J. H. Smith, S. Montague, J. J. Sniegowski, J. R. Murray, *et al.*, "Embedded micromechanical devices for the monolithic integration of MEMS with CMOS," *Tech. Digest*, IEEE Int. Electron Devices Meeting (IEDM), Washington, D.C., Dec. 10-13, 1995, pp. 609-612.
- [42] J. M. Bustillo, G. K. Fedder, C. T.-C. Nguyen, and R. T. Howe, "Process technology for the modular integration of CMOS and polysilicon microstructures," *Microsystem Technologies*, 1 (1994), pp. 30-41.
- [43] A. E. Franke, D. Bilic, D. T. Chang, P. T. Jones, T.-J. King, R. T. Howe, and G. C. Johnson, "Post-CMOS integration of germanium microstructures," *Technical Digest*, 12th Int. IEEE MEMS Conf., Orlando, FA, Jan. 17-21, 1999, pp. 630-637.
- [44] H. Baltes, O. Paul, and O. Brand, "Micromachined thermally based CMOS microsensors," *Proc. IEEE*, vol. 86, no. 8, pp. 1660-1678, Aug. 1998.
- [45] G. K. Fedder, S. Santhanam, M. L. Reed, S. C. Eagle, D. F. Guillou, M. S.-C. Lu, and L. R. Carley, "Laminated high-aspect-ratio microstructures in a conventional CMOS process," *Sensors and Actuators*, vol. A57, no. 2, pp. 103-110, March 1997.
- [46] J. W. Weigold, A.-C. Wong, C. T.-C. Nguyen, and S. W. Pang, "A merged process for thick single crystal Si resonators and conventional BiCMOS Circuitry," *IEEE/ASME J. Microelectromech. Syst.*, vol. 8, no. 3, pp. 221-228, Sept. 1999.
- [47] A. Singh, D. Bilic and R. T. Howe, "Performance evaluation of batch-transferred surface micromachined resonators," *Digest of Technical Papers*, 10th Int. Conf. on Solid-State Sensors and Actuators, Sendai, Japan, June 7-10, 1999, pp. 1158-1161.
- [48] A.-C. Wong, Y. Xie, and C. T.-C. Nguyen, "A bonded-micro-platform technology for modular merging of RF MEMS and transistor circuits," *Digest of Technical Papers*, the 11th Int. Conf. on Solid-State Sensors & Actuators (Transducers'01), Munich, Germany, June 10-14, 2001, pp. 992-995.

- [49] A.-C. Wong, J. R. Clark, and C. T.-C. Nguyen, "Anneal-activated, tunable, 68MHz micro-mechanical filters" *Digest of Technical Papers*, 10th International Conference on Solid-State Sensors and Actuators, Sendai, Japan, June 7-10, 1999, pp. 1390-1393.
- [50] Y.-T. Cheng, W.-T. Hsu, L. Lin, C. T.-C. Nguyen, and K. Najafi, "Vacuum packaging using localized aluminum/silicon-to-glass bonding," *Technical Digest*, 14th Int. IEEE Micro Electro Mechanical Systems Conference, Interlaken, Switzerland, Jan. 21-25, 2001, pp. 18-21.
- [51] C. T.-C. Nguyen, "Transceiver front-end architectures using vibrating micromechanical signal processors (invited)," *Dig. of Papers*, Topical Meeting on Silicon Monolithic Integrated Circuits in RF Systems, Sept. 12-14, 2001, pp. 23-32.
- [52] C. T.-C. Nguyen, "Micromechanical circuits for communication transceivers (invited)," *Proceedings*, 2000 Bipolar/BiCMOS Circuits and Technology Meeting (BCTM), Minneapolis, Minnesota, September 25-26, 2000, pp. 142-149.
- [53] C. T.-C. Nguyen, "Transceiver front-end architectures using vibrating micromechanical signal processors," to be published in *Low Power Communications Electronics*, edited by G. I. Haddad, T. Itoh, and J. Harvey (35 pages).

6.0 LIST OF PUBLICATIONS (over the period of this grant)

- [1] †A.-C. Wong and C. T.-C. Nguyen, "Micromechanical mixer-filters ("mixlers")," submitted to *IEEE/ASME J. Microelectromech. Syst.* in Sept. 2001.
- [2] K. Wang, A.-C. Wong, and C. T.-C. Nguyen, "VHF free-free beam high- Q micromechanical resonators," *IEEE/ASME J. Microelectromech. Syst.*, vol. 9, no. 3, pp. 347-360, Sept. 2000.
- [3] F. D. Bannon III, J. R. Clark, and C. T.-C. Nguyen, "High frequency micromechanical filters," *IEEE J. Solid-State Circuits*, vol. 35, no. 4, pp. 512-526, April 2000.
- [4] K. Wang and C. T.-C. Nguyen, "High-order medium frequency micromechanical electronic filters," *IEEE/ASME J. Microelectromech. Syst.*, vol. 8, no. 4, pp. 534-557, Dec. 1999.
- [5] J. W. Weigold, A.-C. Wong, C. T.-C. Nguyen, and S. W. Pang, "A merged process for thick single crystal Si resonators and conventional BiCMOS Circuitry," *IEEE/ASME J. Microelectromech. Syst.*, vol. 8, no. 3, pp. 221-228, Sept. 1999.
- [6] C. T.-C. Nguyen, "Frequency-selective MEMS for miniaturized low-power communication devices (invited)," *IEEE Trans. Microwave Theory Tech.*, vol. 47, no. 8, pp. 1486-1503, Aug. 1999.
- [7] C. T.-C. Nguyen and R. T. Howe, "An integrated CMOS micromechanical resonator high- Q oscillator," *IEEE J. Solid-State Circuits*, vol. 34, no. 4, pp. 440-455, April 1999.
- [8] C. T.-C. Nguyen, L. P.B. Katehi, and G. M. Rebeiz, "Micromachined devices for wireless communications (invited)," *Proc. IEEE*, vol. 86, no. 8, pp. 1756-1768, Aug. 1998.
- [9] W. -T. Hsu and C. T. -C. Nguyen, "Stiffness-compensated temperature-insensitive micro-mechanical resonators," *Tech. Digest*, 2002 IEEE Int. Micro Electro Mechanical Systems Conf., Las Vegas, Nevada, Jan. 20-24, 2002, pp. 731-734.

- [10] J. Wang, J. E. Butler, D. S. Y. Hsu, and C. T.-C. Nguyen, "CVD polycrystalline diamond high- Q micromechanical resonators" *Tech. Digest*, 2002 IEEE Int. Micro Electro Mechanical Systems Conf., Las Vegas, Jan. 20-24, 2002, pp. 657-660.
- [11] C. T.-C. Nguyen, "RF MEMS for Low-Power Communications," *Extended Abstracts*, 2001 Int. Conf. on Solid-State Devices and Materials (SSDM'01), Tokyo, Japan, Sept. 26-28, 2001, pp. 462-463.
- [12] C. T.-C. Nguyen, "Transceiver front-end architectures using vibrating micromechanical signal processors (invited)," *Dig. of Papers*, Topical Meeting on Silicon Monolithic Integrated Circuits in RF Systems, Sept. 12-14, 2001, pp. 23-32.
- [13] C. T.-C. Nguyen, "Vibrating RF MEMS for low power wireless communications (invited keynote)," *Proceedings*, 2000 Int. MEMS Workshop (iMEMS'01), Singapore, July 4-6, 2001, pp. 21-34.
- [14] S. Lee, M. U. Demirci, and Clark T.-C. Nguyen, "A 10-MHz micromechanical resonator Pierce reference oscillator for communications," *Digest of Technical Papers*, the 11th Int. Conf. on Solid-State Sensors & Actuators (Transducers'01), Munich, Germany, June 10-14, 2001, pp. 1094-1097.
- [15] W. -T. Hsu, J. R. Clark, and C. T. -C. Nguyen, " Q -optimized lateral free-free beam micro-mechanical resonators," *Digest of Technical Papers*, the 11th Int. Conf. on Solid-State Sensors & Actuators (Transducers'01), Munich, Germany, June 10-14, 2001, pp. 1110-1113.
- [16] W. -T. Hsu, J. R. Clark, and C. T. -C. Nguyen, "A resonant temperature sensor based on electrical spring softening," *Digest of Technical Papers*, the 11th Int. Conf. on Solid-State Sensors & Actuators (Transducers'01), Munich, Germany, June 10-14, 2001, pp. 1484-1487.
- [17] A.-C. Wong, Y. Xie, and C. T.-C. Nguyen, "A bonded-micro-platform technology for modular merging of RF MEMS and transistor circuits," *Digest of Technical Papers*, the 11th Int. Conf. on Solid-State Sensors & Actuators (Transducers'01), Munich, Germany, June 10-14, 2001, pp. 992-995.
- [18] J. R. Clark, W.-T. Hsu, and C. T.-C. Nguyen, "Measurement techniques for capacitively-transduced VHF-to-UHF micromechanical resonators," *Digest of Technical Papers*, the 11th Int. Conf. on Solid-State Sensors & Actuators (Transducers'01), Munich, Germany, June 10-14, 2001, pp. 1118-1121.
- [19] R. Navid, J. R. Clark, M. Demirci, and C. T.-C. Nguyen, "Third-order intermodulation distortion in capacitively-driven CC-beam micromechanical resonators," *Technical Digest*, 14th Int. IEEE Micro Electro Mechanical Systems Conference, Interlaken, Switzerland, Jan. 21-25, 2001, pp. 228-231.
- [20] W.-T. Hsu, J. R. Clark, and C. T.-C. Nguyen, "A sub-micron capacitive gap process for multiple-metal-electrode lateral micromechanical resonators," *Technical Digest*, 14th Int. IEEE Micro Electro Mechanical Systems Conference, Interlaken, Switzerland, Jan. 21-25, 2001, pp. 349-352.
- [21] Y.-T. Cheng, W.-T. Hsu, L. Lin, C. T.-C. Nguyen, and K. Najafi, "Vacuum packaging using localized aluminum/silicon-to-glass bonding," *Technical Digest*, 14th Int. IEEE Micro

Electro Mechanical Systems Conference, Interlaken, Switzerland, Jan. 21-25, 2001, pp. 18-21.

- [22] J. R. Clark, W.-T. Hsu, and C. T.-C. Nguyen, "High- Q VHF micromechanical contour-mode disk resonators," *Technical Digest*, IEEE Int. Electron Devices Meeting, San Francisco, California, Dec. 11-13, 2000, pp. 399-402.
- [23] W.-T. Hsu, J. R. Clark, and C. T.-C. Nguyen, "Mechanically temperature compensated flexural-mode micromechanical resonators," *Technical Digest*, IEEE Int. Electron Devices Meeting, San Francisco, California, Dec. 11-13, 2000, pp. 493-496.
- [24] J.-B. Yoon and C. T.-C. Nguyen, "A high- Q tunable micromechanical capacitor with movable dielectric for RF applications," *Technical Digest*, IEEE Int. Electron Devices Meeting, San Francisco, California, Dec. 11-13, 2000, pp. 489-492.
- [25] C. T.-C. Nguyen, "Micromechanical circuits for communication transceivers (invited)," *Proceedings*, 2000 Bipolar/BiCMOS Circuits and Technology Meeting (BCTM), Minneapolis, Minnesota, September 25-26, 2000, pp. 142-149.
- [26] C. T.-C. Nguyen, "Micromechanical circuits for wireless communications (invited plenary)," *Proceedings*, 2000 European Solid-State Device Research Conference, Cork, Ireland, September 11-13, 2000, pp. 2-12.
- [27] C. T.-C. Nguyen, "Transceiver front-end architectures using high- Q micromechanical resonators (invited)," *Proceedings*, IEEE European MIDAS Workshop, University of Surrey, United Kingdom, July 17-18, 2000.
- [28] C. T.-C. Nguyen, "Communication architectures based on high- Q MEMS devices (invited)," *Workshop Notes*, Workshop on Microwave and Photonic Applications of MEMS at the 2000 IEEE MTT-S International Microwave Symposium, Anaheim, California, June 16, 2000.
- [29] S. Pacheco, L. P. B. Katehi, and C. T.-C. Nguyen, "Design of low actuation voltage RF MEMS switches," *Proceedings*, IEEE MTT-S International Microwave Symposium, Boston, Massachusetts, June 11-16, 2000.
- [30] C. T.-C. Nguyen, "Micromechanical circuits for communications (invited)," *Proceedings*, 2000 Int. Conference on High Density Interconnect and Systems Packaging, Denver, Colorado, April 25-28, 2000, pp. 112-117.
- [31] C. T.-C. Nguyen, "Micromechanical components for miniaturized low-power communications (invited)," *Proceedings*, 1999 IEEE MTT-S International Microwave Symposium RF MEMS Workshop (on Microelectromechanical Devices for RF Systems: Their Construction, Reliability, and Application), Anaheim, California, June 18, 1999, pp. 48-77.
- [32] A.-C. Wong, J. R. Clark, and C. T.-C. Nguyen, "Anneal-activated, tunable, 68MHz micromechanical filters" *Digest of Technical Papers*, 10th International Conference on Solid-State Sensors and Actuators, Sendai, Japan, June 7-10, 1999, pp. 1390-1393.
- [33] W.-T. Hsu, S. Lee, and C. T.-C. Nguyen, "*In situ* localized annealing for contamination resistance and enhanced stability in nickel micromechanical resonators," *Digest of Technical Papers*, 10th International Conference on Solid-State Sensors and Actuators, Sendai, Japan, June 7-10, 1999, pp. 932-935.

- [34] J. Cao and C. T.-C. Nguyen, "Drive Amplitude Dependence of Micromechanical Resonator Series Motional Resistance," *Digest of Technical Papers*, 10th International Conference on Solid-State Sensors and Actuators, Sendai, Japan, June 7-10, 1999, pp. 1826-1829.
- [35] V. L. Rabinovich, M. Deshpande, J. R. Gilbert, M.-A. Getillat, N. de Rooij, J. R. Clark, and C. T.-C. Nguyen, "Prediction of mode frequency shifts due to electrostatic bias," *Digest of Technical Papers*, 10th International Conference on Solid-State Sensors and Actuators, Sendai, Japan, June 7-10, 1999, pp. 442-445.
- [36] T. C. Nolan, W. E. Stark, and C. T.-C. Nguyen, "Direct down conversion of passband signals using MEMS filters and sub-sampling," *Proceedings*, the Spring 1999 IEEE Vehicular Technology Conference, Houston, TX, May 16-19, 1999. (paper copy of *Proceedings* has an error; CD ROM copy is correct)
- [37] C. T.-C. Nguyen, "Micromechanical filters for miniaturized low-power communications," *Proceedings of SPIE: Smart Structures and Materials (Smart Electronics and MEMS)*, Newport Beach, California, March 1-5, 1999, pp. 55-66.
- [38] C. T.-C. Nguyen, A.-C. Wong, and H. Ding, "Tunable, switchable, high- Q VHF microelectromechanical bandpass filters," *Digest of Technical Papers*, 1999 IEEE International Solid-State Circuits Conference, San Francisco, California, Feb. 15-17, 1999, pp. 78-79, 448.
- [39] K. Wang, Y. Yu, A.-C. Wong, and C. T.-C. Nguyen, "VHF free-free beam high- Q micro-mechanical resonators," *Technical Digest*, 12th International IEEE Micro Electro Mechanical Systems Conference, Orlando, Florida, Jan. 17-21, 1999, pp. 453-458.
- [40] A.-C. Wong, H. Ding, and C. T.-C. Nguyen, "Micromechanical mixer+filters," *Technical Digest*, IEEE International Electron Devices Meeting, San Francisco, California, Dec. 6-9, 1998, pp. 471-474. (**best paper award winner**)
- [41] W.-T. Hsu and C. T.-C. Nguyen, "Geometric stress compensation for enhanced thermal stability in micromechanical resonators," *Proceedings*, 1998 IEEE International Ultrasonics Symposium, Sendai, Japan, Oct. 5-8, 1998, pp. 945-948.
- [42] C. T.-C. Nguyen, "Micromachining technologies for miniaturized communication devices (invited plenary)," *Proceedings of SPIE: Micromachining and Microfabrication*, Santa Clara, California, Sept. 20-22, 1998, pp. 24-38.
- [43] C. T.-C. Nguyen, "Communications applications of microelectromechanical systems (invited)," *Proceedings*, Sensors Expo, San Jose, California, May 20, 1998, pp. 447-455.
- [44] L. P.B. Katehi, G. M. Rebeiz, and C. T.-C. Nguyen, "MEMS and Si-micromachined components for low-power, high-frequency communications systems (invited)," *Proceedings*, IEEE MTT-S International Microwave Symposium, Baltimore, Maryland, June 7-12, 1998, pp. 331-333.
- [45] S. Pacheco, C. T.-C. Nguyen, and L. P. B. Katehi, "Micromechanical electrostatic K-band switches," *Proceedings*, IEEE MTT-S International Microwave Symposium, Baltimore, Maryland, June 7-12, 1998, pp. 1569-1572. (**Judges award winner**)
- [46] C. T.-C. Nguyen, "Frequency-selective MEMS for miniaturized communication devices (invited)," *Proceedings*, 1998 IEEE Aerospace Conference, Snowmass, Colorado, March 21-28, 1998, pp. 445-460.

- [47] C. T.-C. Nguyen, "Micromechanical devices for wireless communications (invited plenary)," *Proceedings*, 1998 IEEE International Workshop on Micro Electro Mechanical Systems, Heidelberg, Germany, Jan. 25-29, 1998, pp. 1-7.
- [48] K. Wang, F. D. Bannon III, J. R. Clark, and C. T.-C. Nguyen, " Q -enhancement of micro-mechanical filters via low-velocity spring coupling," *Proceedings*, 1997 IEEE International Ultrasonics Symposium, Toronto, Ontario, Canada, Oct. 5-8, 1997, pp. 323-327.
- [49] K. Wang, A.-C. Wong, W.-T. Hsu, and C. T.-C. Nguyen, "Frequency-trimming and Q -factor enhancement of micromechanical resonators via localized filament annealing," *Digest of Technical Papers*, 1997 International Conference on Solid-State Sensors and Actuators, Chicago, Illinois, June 16-19, 1997, pp. 109-112.
- [50] J. R. Clark, A.-C. Wong, and C. T.-C. Nguyen, "Parallel-resonator HF Micromechanical Bandpass Filters," *Digest of Technical Papers*, 1997 International Conference on Solid-State Sensors and Actuators, Chicago, Illinois, June 16-19, 1997, pp. 1161-1164.
- [51] C. T.-C. Nguyen, "High- Q micromechanical oscillators and filters for communications (invited)," *Proceedings*, 1997 IEEE Int. Symposium on Circuits and Systems, Hong Kong, June 9-12, 1997, pp. 2825-2828.

7.0 LIST OF INVITED PRESENTATIONS (over the period of this grant)

To better convey the degree to which the work of this grant has been disseminated at various conferences, the following comprises a list of invited presentations given by the PI over the course of this grant:

Invited Papers/Presentations: (does not include industry visits)

Total Number of Accepted Invites: 48

Plenary or Keynote Presentations: 5

- | | |
|-------------------|--|
| 7/4/01 - 7/6/01 | • <u>Invited Paper/Presentation (Keynote)</u> , "Vibrating RF MEMS for Low Power Wireless Communications," 2001 International MEMS Workshop, Singapore. |
| 9/11/00 - 9/13/00 | • <u>Invited Paper/Presentation (Plenary)</u> , "Micromechanical circuits for wireless communications," 2000 European Solid-State Device Research Conference, Cork, Ireland. |
| 7/12/99 - 7/14/99 | • <u>Invited Presentation (Keynote)</u> , "Vibrating micromechanical resonators for miniaturized low-power communications," 11 th International Conference on Wireless Communications (Wireless'99), Calgary, Canada. |
| 9/20/98 - 9/22/98 | • <u>Invited Paper/Presentation (Plenary)</u> , "Micromachining technologies for miniaturized communication devices," 1998 SPIE MEMS Conference, Santa Clara, California. |
| 1/25/98 - 1/29/98 | • <u>Invited Paper/Presentation (Plenary)</u> , "Micromechanical devices for wireless communications," 1998 IEEE International Workshop on Micro Electro Mechanical Systems, Heidelberg, Germany. |

Invited Short Courses at Conferences/Workshops: 2

- | | |
|--------|---|
| 7/3/01 | • <u>Invited Short Course</u> , "RF MEMS for Wireless Communications," given at the 2001 Int. MEMS Workshop, Singapore. |
|--------|---|

- 6/10/01 • Invited Short Course, “Micromechanical RF Devices for Communication Transceivers,” given at the 11th Int. Conference on Solid-State Sensors and Actuators (Transducers’01), 9 a.m.-12:30 p.m., Munich, Germany.

Other Invited Presentations at Conferences/Workshops: 41

(Key: P/P = paper and presentation, PA = journal paper, PR = presentation only, PN = panel member)

- | | |
|-------------------|---|
| 9/26/01 - 9/28/01 | • <u>P/P</u> : 2001 Int. Conf. on Solid-State Devices and Materials (SSDM’01) |
| 9/18/01 - 9/21/01 | • <u>PN</u> : Small Tech 2001 Conference |
| 9/12/01 - 9/14/01 | • <u>P/P</u> : 2001 Topical Mtg. on Silicon Monolithic IC’s in RF Systems |
| 8/29/01 - 8/31/01 | • <u>PR</u> : Summer 2001 DARPA/MEMS PI Meeting |
| 5/3/01 - 5/4/01 | • <u>PR</u> : 2001 Advisory Group on Electron Devices Meeting (AGED’01) |
| 3/22/01 - 3/23/01 | • <u>PR</u> : DARPA/MTO Workshop on Chip-Scale Atomic Clocks |
| 2/16/01 | • <u>PN</u> : 2001 Microsystems Symposium |
| 9/25/00 - 9/26/00 | • <u>P/P</u> : 2000 Bipolar/BiCMOS Circuits and Technology Meeting (BCTM) |
| 8/23/00 - 8/25/00 | • <u>PR</u> : Summer 2000 DARPA MEMS PI Meeting |
| 7/17/00 - 7/18/00 | • <u>P/P</u> : 2000 IEEE European MIDAS Workshop |
| 6/16/00 | • <u>P/P</u> : Workshop on Microwave and Photonic Applications of MEMS at the 2000 IEEE MTT-S International Microwave Symposium |
| 6/5/00 | • <u>PN</u> : 2000 37 th Design Automation Conference (DAC) |
| 4/25/00 - 4/28/00 | • <u>P/P</u> : 2000 Int. Conference on High Density Interconnect and Systems Packaging |
| 3/14/00 | • <u>PR</u> : Solid-State Sciences Seminar Series, California Inst. of Technology |
| 3/13/00 | • <u>PR</u> : BSAC Seminar, University of California, Berkeley |
| 12/1/99 - 12/2/99 | • <u>PR</u> : NSF/ARO/DARPA/NRL Workshop on RF Micromachining and MEMS Technology for Wireless Communications Systems |
| 8/99 | • <u>PA</u> : <i>IEEE Trans. on Microwave Theory Tech.</i> (invited journal paper) |
| 6/18/99 | • <u>P/P</u> : Workshop on Microelectromechanical Devices for RF Systems at the 1999 IEEE MTT-S International Microwave Symposium |
| 3/1/99 - 3/5/99 | • <u>P/P</u> : 1999 SPIE Symposium on Smart Structures and Materials |
| 2/22/99 - 2/23/99 | • <u>PR</u> : DARPA Workshop on MEMS for Mechanical Computation and Information Processing |
| 2/16/99 | • <u>PN</u> : 1999 International Solid-State Circuits Conference (ISSCC) |
| 2/14/99 | • <u>P/P</u> : 1999 IEEE Solid-State Circuits Technology Workshop on RF Passive Components |
| 1/13/99 | • <u>PR</u> : DoD-Wide MEMS Meeting |
| 1/12/99 | • <u>PR</u> : Baltimore IEEE MTT Local Chapter Meeting |
| 11/3/98 | • <u>PR</u> : Air Force Research Laboratory (AFRL) |
| 9/29/98 | • <u>PR</u> : Southeast Michigan SPIE Local Chapter Meeting |
| 8/98 | • <u>PA</u> : <i>Proc. IEEE</i> (invited journal paper) |
| 5/19/98 - 5/21/98 | • <u>P/P</u> : 1998 Sensors Expo |

- | | |
|-------------------|--|
| 6/7/98 - 6/12/98 | • <u>PN</u> : 1998 IEEE MTT-S International Microwave Symposium (IMS) |
| 4/21/98 - 4/22/98 | • <u>PR</u> : Micro-Nanotechnology for Micro-Nanosatellites Workshop |
| 3/21/98 - 3/28/98 | • <u>P/P</u> : 1998 IEEE Aerospace Conference |
| 2/24/98 - 2/25/98 | • <u>PR</u> : MCC Heterogeneous Component Integration Executive Workshop |
| 1/15/98 - 1/16/98 | • <u>PR</u> : DARPA/MEMS PI Meeting |
| 1/14/98 | • <u>PR</u> : DoD-Wide MEMS Meeting |
| 10/28/97 | • <u>PR</u> : Cornell University |
| 5/27/97 - 5/29/97 | • <u>PR</u> : DARPA Composite CAD Semi-Annual PI Meeting |
| 6/9/97 - 6/12/97 | • <u>P/P</u> : 1997 IEEE International Symposium on Circuits and Systems |